



University of Zagreb  
Faculty of Science  
Department of Physics

Blaž Ivšić

**Coupling of Rac1 protein dynamics and cell  
shape in *Dictyostelium discoideum***

DOCTORAL THESIS

Zagreb, 2026



University of Zagreb  
Faculty of Science  
Department of Physics

Blaž Ivšić

**Coupling of Rac1 protein dynamics and cell  
shape in *Dictyostelium discoideum***

DOCTORAL THESIS

Supervisors:

Sr. Res. Assoc. Tomislav Vuletić, PhD

Prof. Matko Glunčić, PhD

Zagreb, 2026



Sveučilište u Zagrebu  
Prirodoslovno-matematički fakultet  
Fizički odsjek

Blaž Ivšić

**Sprega dinamike proteina Rac1 i oblika  
stanica *Dictyostelium discoideum***

DOKTORSKI RAD

Mentori:

dr. sc. Tomislav Vuletić  
prof. dr. sc. Matko Glunčić

Zagreb, 2026

# Acknowledgements

This thesis was prepared during my five-year appointment at the Institute of Physics, Zagreb, and a subsequent six-month appointment at the Ruđer Bošković Institute, Zagreb. I thank my formal mentors, Tomislav Vuletić, PhD (Institute of Physics), and Prof. Matko Glunčić, PhD (Faculty of Science, Department of Physics), for the opportunity and guidance provided during the preparation of this dissertation.

I am especially grateful to Prof. Ana Sunčana Smith, PhD and Prof. Igor Weber, PhD for their substantive help throughout this work. I thank the assistants and scientists in the Laboratory for Cell Dynamics at the Ruđer Bošković Institute (supervised by Prof. Weber) for preparing the cell cultures used in my microscopy experiments and for providing access to the laboratory microscope. I owe particular thanks to Piotr Nowakowski of the Computational Life Sciences group, led by Prof. Smith within the Division for Physical Chemistry at the Ruđer Bošković Institute. His generous help in shaping the model for simulating live cells and in its implementation was invaluable. I also thank Marko Šoštar (Laboratory for Cell Dynamics) for providing microscopy images, contributing to the imaging effort alongside me, and analysing part of the dataset used here. Some of these data previously appeared in a publication by Marko Šoštar, which I acknowledge here Šoštar et al., 2024.

I acknowledge the computational resources provided by SRCE (University Computing Centre), which enabled the large-scale simulations reported in this thesis. This work was supported by the Croatian Science Foundation (IP-2024-05: Dissecting the redundancy of Rac1 isoforms in *Dictyostelium discoideum*) and by the Croatian Science Foundation & Swiss National Science Foundation, Croatian-Swiss Research Program (CSRP 2017–2023), Phagocytosis and Macropinocytosis: a mechanistic view (with Pierre Cosson, University of Geneva).

Finally, I thank my parents and my brother for their unconditional support during the writing of this thesis. I also thank all my friends, especially David and Filip, who selflessly put up with me and motivated me to complete this doctoral dissertation.

# Abstract

Eukaryotic cells crawl by coupling intracellular signalling to membrane mechanics and cytoplasmic flow. This thesis examines how that coupling organises motility patterns using a minimal mechanochemical model. The key ingredient is a spatially variable surface tension along the cortex, linked to activator concentration and acting alongside a normal protrusive stress. In a diffuse-interface level-set framework coupled to Stokes flow and a reaction–diffusion–advection (RDA) system, these couplings generate Marangoni surface flows and cytosolic advection that reshape canonical reaction–diffusion patterns.

To validate the model, we imaged *in vitro Dictyostelium discoideum* expressing a Rac1-GTP probe and defined a motility-centric taxonomy: stationary, alternating runners, circular runners, run-and-stop, and run-and-turn. By tuning protrusive and surface-tension couplings, the model reproduces all motile classes and maps how coupling ratios or protein number variability select characteristic shapes (fan, stadium, egg, flat-front, dumbbell) and trajectories. The results reveal regimes in which behaviour is dominated, respectively, by reaction–diffusion (stationary), by flow-modified patterns (persistent runs), or by geometry-mediated feedback (turning).

This work provides a transparent baseline for future extensions, including spatially varying rheology, alternative surface tension laws, and additional signalling species, and is readily adaptable to other eukaryotic cell types.

Keywords: cell motility, reaction—diffusion—advection systems, cytosolic and cortical flows, variable surface tension.

# Prošireni sažetak

Stanično kretanje, specifično puzanje po površini, je proces o kojem ovise mnogi eukariotski organizmi. Ugrubo ovaj se proces može rastaviti u četiri koraka (Lauffenburger & Horwitz, 1996): polariziranje stanice, istežanje lamelipodija ili filopodija, formacija i raspad adhezivnih mjesta te kontrakcija stražnjeg dijela. Prolazeći kroz cikluse ovih koraka eukariotske stanice mogu efikasno puzati po većini podloga. Cijeli proces staničnog kretanja omogućuje struktura koju nazivamo citoskelet

Općenito, citoskelet eukariotskih stanica sastoji se od tri različita bio-filamenta: aktinska vlakna, mikrotubuli i intermedijarna vlakna. Svako od navedenih vlakana posjeduje specifična svojstva koja mu omogućavaju da obavlja određene funkcije tijekom procesa kretanja (Merino-Casallo et al., 2022). U usporedbi sa sintetskim ili drugim biopolimerima, navedeni filamenti posjeduju mnogo veću čvrstoću smicanja u usporedbi s njihovim poprečnim presjekom.

Ukratko, sva tri filamenta sastoje se od manjih podjedinica koje polimeriziraju u dugačka vlakna. Aktinska vlakna čine većinu citoskeleta te omogućavaju protruziju prednjeg dijela stanice tijekom kretanja. Također, neka od aktinskih vlakana povezana su molekularnim motorima tipa miozin, te formiraju tzv. stresna vlakna koja omogućuju kontrakciju i povlačenje stražnjeg dijela stanice. Mikrotubuli su najčvršći od spomenutih vlakana te služe kao glavni potporanj membrani stanice. Po mikrotubulima se mogu usmjereno kretati molekularni motori tipa dinein koji dopremaju vezikule s unutarstaničnim molekulama iz središta prema membrani stanice. Treća, intermedijarna vlakna, povezuju različite stanične strukture te djeluju kao opruge koje moderiraju naprezanje svojom elastičnošću.

Kako bi se stanica mogla kontrolirano kretati potrebno je regulirati citoskeletnu strukturu sačinjenu od ova tri filamenta. Tu ulogu obavljaju male GTPaze obitelji Rho (Heasman & Ridley, 2008). Ovi proteini djeluju kao sklopke budući da razlikujemo dvije konformacije. U aktivnoj formi za GTPazu je vezan GTP (Guanosine triphosphate) te ona može interagirati s proteinima nizvodno u signalnom putu kojeg je dio. U neaktivnom stanju, dok je za GTPazu vezan GDP (Guanosine diphosphate), ova molekula ne može provoditi signal.

Tri druga proteina reguliraju izmjenu GDP-a za GTP te samim time i dinamiku GTPaza (Jaffe

& Hall, 2005). GEF (GTPase exchange factor) jest protein koji potiče izmjenu GDP-a za GTP što dovodi GTPazu u aktivno stanje. Zatim, GAP (GTPase activating protein), katalizira hidrolizu GTP-a u GDP, dok RhoGDI obuhvaća GTPazu te blokira njezino djelovanje i osigurava bazen ovih proteina dostupnih za provođenje unutarstaničnih signala. Dinamika GTPaza i njihovih regulatornih molekula određuje kako i kamo će se stanica kretati.

Kako bismo modelirali ovaj proces, moramo spregnuti mehaniku citoskeleta i signalnu dinamiku GTPaza. Postoji više pristupa rješavanju ovog problema koji se razlikuju u kompleksnosti implementacije kao i u preciznosti modela (Buttenschön & Edelstein-Keshet, 2020). Za potrebe ove teze, odlučili smo koristiti metodu skupa razina (Level-set method) spregnutu s reakcijsko-difuzijskim sustavom koji modelira signalnu dinamiku GTPaza. Ova metoda omogućava praćenje kompleksnih oblika stanice te odjeljivanje unutar i izvanstanične tekućine. Kako bi se stanica mogla kretati rješavamo Navier-Stokes jednadžbu fluida koja uključuje membranske sile koje stvaraju tok na cijeloj računalnoj domeni. Taj tok tekućine posljedično pomiče funkciju skupa razina koja određuje položaj stanice.

Sile na membrani koje djeluju na tekućinu, uključuju površinsku napetost, faktor koji drži površinu stanice konstantnom, viskozno trenje koje sprječava divergirajuće ubrzanje stanice te sile koje ovise o koncentraciji određenog proteina. U naš model uključili smo dvije takve sile: protruzivnu silu koja ovisi linearno o koncentraciji tzv. aktivatora (proteina za koji pretpostavljamo da određuje prednji kraj stanice) i djeluje okomito na membranu prema van, te Marangonijeva sliku koja nastaje zbog promjenjive površinske napetosti koja također ovisi o koncentraciji aktivatora.

Protruzivna sila spregnuta je s aktivatorom što modelira aktinski dio citoskeleta koji pomiče prednji kraj stanice prema naprijed polimeriziranje vlakana. Ujedno prilikom kretanja stanice, stražnji dio se povlači prema naprijed dok se na prednjem dijelu globalna napetost smanjuje membrane smajuje kako bi se prednji kraj mogao gurnuti prema naprijed. Kako bismo objedinili kontrakciju i smanjenu frontalnu napetost, odlučili smo u naš model dodati linearnu ovisnost napetosti površine o koncentraciji aktivatora (Whitfield & Hawkins, 2016).

Sprega koncentracije aktivatora s protruzivnom silom i promjenjivom napetošću površine generira tok tekućine koja prenosi funkciju razina. Karakteristični tokovi javljaju se na membrani stanice te u unutrašnjosti stanice. Protruzivna sila stvara tok u citosolu koji formira dva vrtloga koja kruže od prednjeg prema stražnjem dijelu stanice uz membranu te se vraćaju sa stražnjeg prema prednjem dijelu kroz sredinu (slika 2.10). Promjenjiva površinska napetost, stvara Marangonijev tok koji tjera tekućinu od područja niže prema području više površinske napetosti. Ovisno o predznaku parametra sprege razlikujemo dva slučaja. U prvom se maksimalna koncentracija aktivatora poklapa s nižom površinskom napetošću što dovodi do toka

na membrani koji teče od prednjeg prema stražnjem dijelu stanice. Taj tok uzrokuje tok u citosolu sličan onom kojeg stvara protruzivna sila (slika 2.11 C i D). S druge strane, ako je sprega pozitivna, maksimalna koncentracija aktivatora poklapa se s većom površinskom napetošću te je tok preokrenut u odnosu na prvi slučaj (slika 2.11 A i B). Spomenuti tokovi znatno utječu na dinamiku reakcijsko–difuzijskog sustava te mijenjaju njegova karakteristična rješenja.

Kako bismo provjerili valjanost našeg pristupa odlučili smo primijeniti naš model na kretanje amebe *Dictyostelium discoideum*. Ove amebe, koje žive na šumskom tlu, poznate su po svojoj pokretljivosti. Njihov je citoskelet i regulatorni putevi koji ga kontroliraju, pojednostavljen u odnosu na više eukariote. To čini ove amebe idealnim organizmom za proučavanje staničnog kretanja kao i za validaciju našeg minimalnog modela takvog kretanja.

Stanice organizma *Dictyostelium* baziraju svoje brzo kretanje na tzv aktinsko-miosinskom korteksu koji ježi s unutarnje strane stanične membrane. Ove stanice ne posjeduju klasična intermedijarna vlakna, dok mikrotubuli igraju ulogu potpornja i ne sudjeluju znatno u samom procesu kretanja. Nadalje, ove stanice posjeduju samo jednu GTPazu, Rac1, koja kontrolira kretanje, za razliku od kompleksnijih organizama koji ih posjeduju nekoliko.

Snimanjem *in vitro* ameba, klasificirana su četiri karakteristična načina kretanja prema dinamici same stanice kao i dinamici aktivne forme proteina Rac1 koja je praćena fluorescentnom sondom. Najprije u eksperimentalnim podacima razlikujemo stanice koje miruju te one koje se kreću. Stanice koje se kreću možemo dalje podijeliti na: alternirajuće trkače, kružeće trkače, kreni-stani stanice te kreni-skreni stanice. Pojedine klase krećućih stanica možemo razlikovati usporedbom statističkih mjera prikazanih na slici 3.12.

Kako bismo usporedili rezultate modela s eksperimentalnim rezultatima odlučili smo prilagoditi reakcijsko-difuzijski sustav jednadžbi prema postojećem radu (Šoštar et al., 2024). Predloženi model prati dva proteina Rac1 te njegov GAP. Neaktivna forma Rac1 nalazi se u citosolu stanice, dok je aktivna forma vezana specifično za membranu. Slično GAP protein nalazi se također u citosolu no može interagirati s membranskim Rac1 te formirati kompleks Rac1-GTP-GAP koji je također lokaliziran na membrani. Kao što smo već spomenuli protruzivna sila i varijabilna površinska napetost spregnute su s koncentracijom aktivatora koji je u ovom slučaju membranski Rac1-GTP.

Naš primijenjeni model može simulirati sve četiri klase krećućih stanica koje smo primijetili u eksperimentu. Dodatno smo u simulacijama uočili i uporne trkače koji više liče na amebe u stanju kemotaksije, dok ih u vegetativnom stanju nismo primijetili. Klasu kretanja stanice u simulacijama određuje omjer parametara sprege (slika 2.18). Za malu protruzivnu spregu te pozitivnu spregu s površinskom napetošću stanice u simulacijama miruju, budući da je dinamika proteina brža od promijene oblika, dok inducirani Marangonijev tok dodatno ubrzava tu dinamiku.

Povećavanjem protruzivne sprege i/ili nametanjem negativne sprege s površinskom napetošću, stanice se počinju perzistentno kretati bez zaustavljanja te ih nazivamo uporni trkači. Taj je način kretanja uzrokovan tokom unutar citosola koji dovodi nove molekule na prednji dio stanice gdje je koncentracija aktivatora već visoka.

Dodatnim smanjenjem sprege s površinskom napetošću dolazimo do kreni-skreni stanica. Za ovu je klasu karakteristično što počinju svoje kretanje kao i uporni trkači no unutarstanični tokovi te promjena oblika dovodi do širenja prednjeg dijela stanice a time i smanjenje koncentracije aktivatora. Kada se stanica raširi okomit na smjer gibanja, koncentracija aktivatora pada te stanica usporava. U trenutku kad tok unutar stanice dovoljno opadne, reakcijsko-difuzijska dinamika preuzima glavnu ulogu te dovodi do poravnanja maksimuma koncentracije aktivatora na membrani ponovno s dužom osi oblika stanice što dovodi do skretanja.

Na prijelazu tri spomenute klase u faznom dijagramu razapetom parametrima sprege pojavljuju se preostale dvije klase uočene u eksperimentu: alternirajući trkači i kružeći trkači. Obje klase nastaju kao produženje rotacijskog i oscilacijskog obrasca u dinamici proteina stacionarnih stanica, slika 2.7 (Šoštar et al., 2024). Karakteristike simuliranih stanica dobro odgovaraju onima koje smo primijetili u eksperimentu.

Naš model uspješno je opisao većinu eksperimentalno opaženih načina kretanja. Nadalje, nedavno objavljeni rad (Chen et al., 2024) predlaže da dinamika aktivatora u stanicama ovisi o podjeli energije između pojedinih dijelova stanice uključenih u kretanje. Sličan zaključak mogli bi donijeti i na temelju naših rezultata. Ovisno o tome koji dio model dominira, stanica eksplicira određeni način kretanja. Ako reakcije između proteina dominiraju stanice su većinom statične budući da ih mehanika promijene oblika ne može sustići. Perzistentne trkače karakterizira usmjereno kretanje bez usporavanja. U tom režimu tokovi unutar citosola dominiraju nad dinamikom proteina. Slično kod trči-skreni stanica, oblik moderira tokove koji nameću perzistentno kretanje. Kada se oblik dovoljno raširi u smjeru okomitom na kretanje tokovi unutar citosola opadaju i dinamika proteina ponovno sustiže mehaniku i nameće promjenu smjera.

Osim omjera parametara sprege, različite klase moguće je simulirati i promijenom broja molekula u sustavu. Moguća rješenja dostupna reakcijsko-difuzijskom sustavu s očuvanom masom ovise o broju molekula koje se nalaze u sustavu. Varijacijom broja Rac1 i GAP molekula uspjeli smo simulirati većinu klasa stanica te time predložili biološki način na koji stanice mogu mijenjati svoj način kretanja ekspresijom različitih proteina.

U ovoj tezi predstavljen je minimalni model staničnog kretanja. Novost u odnosu na postojeće modele, leži u uključivanju promjenjive površinske napetosti duž membrane stanice. Nejednolika napetost i protruzija sila dovode do stvaranja tokova na membrani te u citosolu stanice koji znatno mijenjaju reakcijsko difuzijska rješenja sustava. Uključivanjem promjene oblika koji je

rezultat spomenutih sila dovodi do spregnutog sustava koji uspješno simulira stanice organizma *Dictyostelium* te karakteristike njegovog kretanja.

Ključne riječi: kretanje stanica, reakcijsko-difuzijsko-advekcijski sustavi, tok citosola, membranski tok, promijenjiva površinska napetost...

# Contents

<b>1</b>	<b>Introduction</b>	<b>1</b>
1.1	Crawling migration . . . . .	1
1.2	Cytoskeleton . . . . .	3
1.2.1	Actin filaments . . . . .	3
1.2.2	Microtubules . . . . .	5
1.2.3	Intermediate filaments . . . . .	5
1.2.4	Emergent mechanics of the cytoskeletal network . . . . .	6
1.3	Cytoskeleton organisation by small GTPases . . . . .	8
1.3.1	Rho-family GTPases as molecular switches and their regulators . . . . .	8
1.3.2	Effector pathways downstream of Rho-family GTPases . . . . .	10
1.3.3	Emergent oscillatory dynamics of Rho GTPases . . . . .	12
1.4	<i>Dictyostelium discoideum</i> : a model organism . . . . .	13
1.4.1	Genomic and experimental advantages . . . . .	14
1.4.2	Cytoskeleton of <i>Dictyostelium discoideum</i> . . . . .	15
1.4.3	Rho GTPase signalling in <i>Dictyostelium discoideum</i> . . . . .	16
1.5	Existing models of cell migration and polarization . . . . .	17
1.5.1	Polarization models . . . . .	18
1.5.2	Motility models . . . . .	19
1.6	Aim of the thesis . . . . .	23
<b>2</b>	<b>Model of cell locomotion</b>	<b>24</b>
2.1	Formulation of the model . . . . .	24
2.1.1	Level-set Formalism . . . . .	24
2.1.2	Fluid dynamics . . . . .	28
2.1.3	Reaction–diffusion–advection system . . . . .	29
2.2	Numerical Methods . . . . .	33
2.2.1	Implementation of the model equations . . . . .	33
2.2.2	Software implementation . . . . .	46
2.2.3	Supplementary routines for analysis of simulation results . . . . .	49
2.3	Behaviour of reaction–diffusion system . . . . .	49
2.3.1	Reaction–diffusion dynamics on circular geometry . . . . .	49
2.3.2	Shape effects on reaction–diffusion dynamics . . . . .	51
2.4	Behaviour of fully coupled model . . . . .	56

2.4.1	Flows induced by coupling . . . . .	56
2.4.2	Classification of solution phenotypes . . . . .	62
2.4.3	Phase diagrams as a function of coupling strengths . . . . .	72
<b>3</b>	<b>Motility and signalling dynamics in <i>Dictyostelium Discoideum</i></b>	<b>77</b>
3.1	Experimental methods . . . . .	77
3.1.1	Cell culture . . . . .	78
3.1.2	Cell Imaging . . . . .	78
3.1.3	Quantitative image analysis . . . . .	79
3.1.4	Qualitative Image Analysis . . . . .	83
3.2	Experimentally observed phenotypes . . . . .	88
3.2.1	Phenotype classes . . . . .	90
3.2.2	Comparison of motile classes . . . . .	96
<b>4</b>	<b>Adaptation of the model to <i>Dictyostelium Discoideum</i></b>	<b>101</b>
4.1	Adaptation of reaction–diffusion system . . . . .	101
4.2	Comparison of live and simulated cells . . . . .	104
4.3	How cells shift between behavioural phenotypes . . . . .	106
4.3.1	Protein variation on stationary cell . . . . .	106
4.3.2	Protein variation with coupling forces . . . . .	109
<b>5</b>	<b>Conclusion and outlook</b>	<b>111</b>
5.1	Conclusion . . . . .	111
5.2	Summary . . . . .	111
5.3	Outlook . . . . .	113
	<b>Appendix</b>	<b>115</b>
	<b>References</b>	<b>126</b>
	<b>Curriculum vitae</b>	<b>137</b>

# List of Figures

1.1	Cell crawling . . . . .	2
1.2	Cytoskeletal components . . . . .	6
1.3	Rho GTPase regulation . . . . .	9
1.4	Basic reaction–diffusion models . . . . .	12
1.5	<i>Dictyostelium discoideum</i> life cycle . . . . .	14
2.1	Profile of the level-set function . . . . .	26
2.2	Profiles of bulk and surface localizing potentials. . . . .	32
2.3	Schematic of the simulation grid . . . . .	34
2.4	Schematic of the simulation work flow . . . . .	40
2.5	Error metrics for assessing stability; batch 1 . . . . .	44
2.6	Error metrics for assessing stability; batch 2 . . . . .	45
2.7	Canonical reaction–diffusion solution types . . . . .	50
2.8	Effect of geometry on reaction–diffusion dynamics . . . . .	53
2.9	Diffusion variation phase diagram . . . . .	55
2.10	Representation of protrusive coupling induced flow . . . . .	58
2.11	Representation of surface tension coupling induced flow . . . . .	60
2.12	Examples of <i>in silico</i> stationary cells . . . . .	63
2.13	Examples of <i>in silico</i> run-and-stop cell . . . . .	64
2.14	Examples of <i>in silico</i> persistent runner cells . . . . .	66
2.15	Example of <i>in silico</i> alternating runner cell . . . . .	68
2.16	Examples of <i>in silico</i> circular runner cells . . . . .	69
2.17	Example of <i>in silico</i> run-and-turn cell . . . . .	71
2.18	Phase diagrams as a function of coupling strengths . . . . .	73
3.1	Example of raw Rac1-GTP probe DYFP channel . . . . .	80
3.2	Example of intensity data after filtering . . . . .	80
3.3	Example of preprocessed segmented cell . . . . .	81
3.4	Example of ECMM mapping . . . . .	82
3.5	Example of intensity sampling band . . . . .	82
3.6	Contour transformations during invariant moments calculation . . . . .	85
3.7	Examples of <i>in vitro</i> stationary cells . . . . .	91
3.8	Example of <i>in vitro</i> alternating runner cell . . . . .	92
3.9	Example of <i>in vitro</i> run-and-stop cell . . . . .	94

3.10	Example of <i>in vitro</i> circular runner cell . . . . .	95
3.11	Example of <i>in vitro</i> run-and-turn cell . . . . .	97
3.12	Statistics of <i>in vitro</i> observed motility phenotypes . . . . .	98
4.1	Schematic representation protein interactions in adapted version of the model .	103
4.2	Phase diagram as a function of protein number 1 . . . . .	107
4.3	Phase diagram as a function of protein number 2 . . . . .	108

# List of Tables

2.1	Parameters used in the simulations . . . . .	42
2.2	Code performance metrics . . . . .	48
5.1	Fixed parameters used in all of the simulations . . . . .	115
5.2	Parameters used in the simulations presented in figure 2.7 . . . . .	116
5.3	Parameters used in the simulations presented in figure 2.8 . . . . .	117
5.4	Parameters used in the simulations presented in figure 2.9 . . . . .	118
5.5	Parameters used in the simulations presented in figure 2.10 . . . . .	118
5.6	Parameters used in the simulations presented in figure 2.11 . . . . .	119
5.7	Parameters used in the simulations presented in figure 2.12 . . . . .	120
5.8	Parameters used in the simulations presented in figure 2.13 . . . . .	121
5.9	Parameters used in the simulations presented in figure 2.14 . . . . .	122
5.10	Parameters used in the simulations presented in figure 2.15 . . . . .	123
5.11	Parameters used in the simulations presented in figure 2.16 . . . . .	123
5.12	Parameters used in the simulations presented in figure 2.17 . . . . .	124
5.13	Parameters used in the simulations presented in figure 2.18 . . . . .	124
5.14	Parameters used in the simulations presented in figure 4.2 . . . . .	125
5.15	Parameters used in the simulations presented in figure 4.3 . . . . .	125

# Chapter 1

## Introduction

Cell migration has fascinated scientist from the discovery of unicellular organisms. However it remains evasive how exactly these small biochemical robots perform such wide range of random as well as persistent motility patterns. This thesis aims to demystify exactly that. We propose a minimal model of interactions including reaction, diffusion, flow, and shape mechanics that can simulate main characteristics of motile cells. To support our models results, we accompany them with experimental observations and analysis. This way we unite the knowledge from both sides and present our findings that elucidate this biophysical problem. We begin our quest begins by presenting biological background of cell motility in general. After broad decomposition of underlying cell machinery needed for motility we focus specifically on motile amoeba *Dictyostelium discoideum*. This amoeba possesses minimal cytoskeletal components which allows for rapid reorganization of its cytoskeleton. We conclude the introduction with the overview of current state-of-the-art numerical models of cell locomotion which sets the stage for the presentation of our approach to modelling cell motility.

### 1.1 Crawling migration

Many organisms can actively relocate within their environment, from flagellated bacteria that swim through liquids to motile fibroblasts that close wounds in animals. Such locomotion is vital for, but not limited to, nutrient acquisition, hazard avoidance, morphogenesis, and immune surveillance. At a coarse level, cell migration can be divided into *swimming* in the medium and *crawling* on the substrate. Swimming, driven by rotating flagella or beating cilia, predominates among bacteria and spermatozoa, whereas crawling, powered by actin polymerisation and actomyosin contractility against a substrate, is characteristic of most eukaryotic cells. As this thesis is focused on the mechanics of actin-driven motility, we will henceforth focus on crawling.

Crawling migration can be parsed into a recurrent four-step cycle (Lauffenburger & Horwitz,

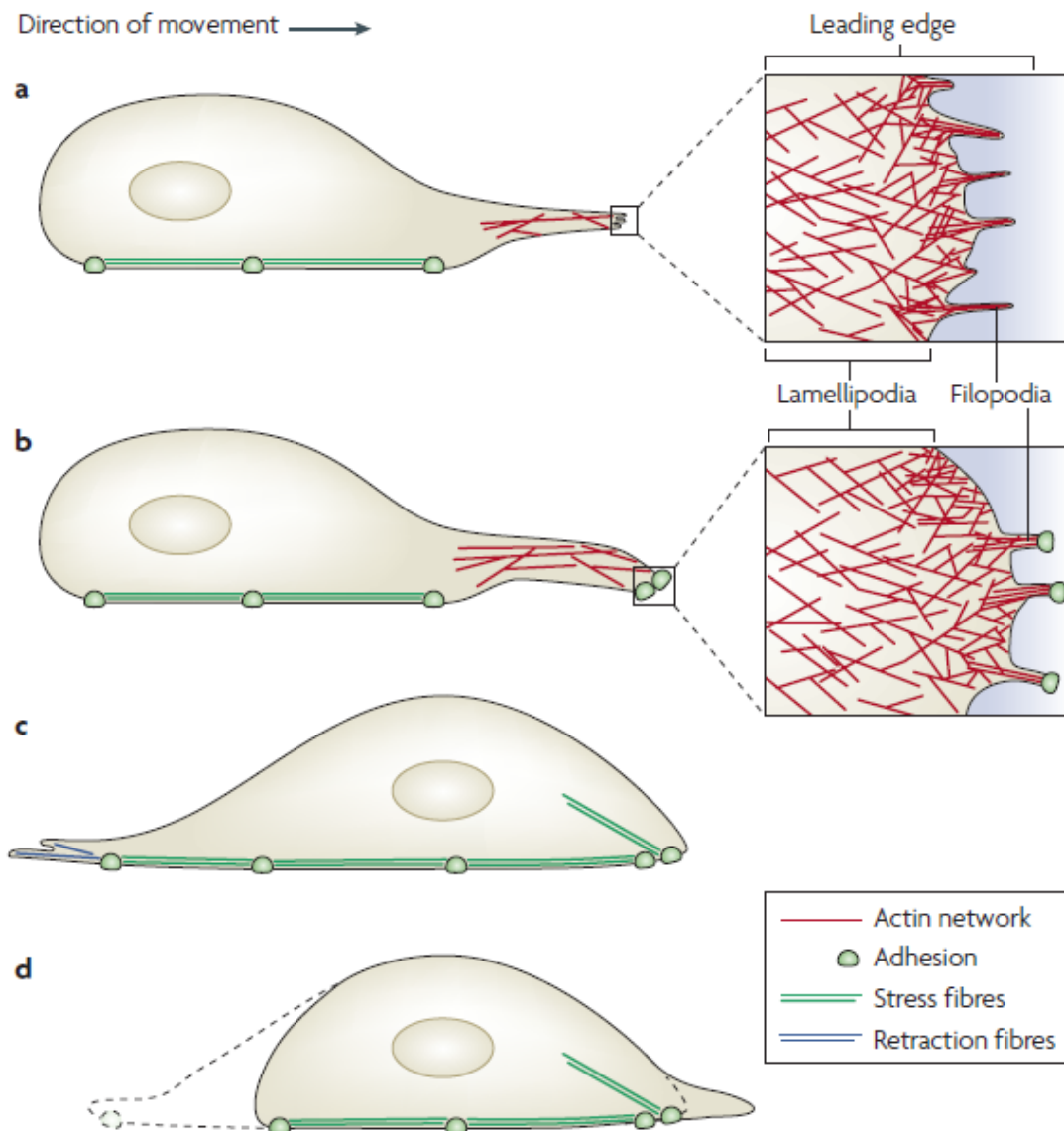


Figure 1.1: Schematic representation of steps during one cycle of crawling motility. Adapted from Mattila & Lappalainen (Mattila & Lappalainen, 2008).

1996):

- 1. Symmetry breaking and front-rear polarisation:** This first step is a prerequisite for persistent motion, without a front–rear axis, intracellular forces cancel out globally.
- 2. Protrusion of lamellipodium (or filopodium):** During protrusion (figure 1.1 a), rapid polymerisation of actin filaments pushes the plasma membrane forward, at the leading edge.
- 3. Formation of new adhesions:** The newly extended membrane establishes novel adhesion complexes (figure 1.1 b), providing a mechanical foothold. Concurrently, adhesions at the

trailing edge disassemble (figure 1.1 c).

**4. Actomyosin-driven contraction:** Myosin-II mini-filaments assemble on the rearward actin arrays and contract the cortex, pulling the cell body toward the anchored front (figure 1.1 d). Repetition of this cycle propels the cell across flat as well as corrugated surfaces.

## 1.2 Cytoskeleton

In this section we lay out the general structural components that allow motility in eukaryotic cells. We start by presenting general cytoskeletal components and their interactions which are not necessarily present in all motile cells. After general motility foundations have been laid out we shift our focus to the model organism *Dictyostelium discoideum*.

To generate net forces during the cycles of protrusion and retraction, a cell must coordinate mechanical properties and output of its distinct body segments. The scaffold that mediates this coordination is the *cytoskeleton*. In higher eukaryotes, the cytoskeleton comprises three filament systems: actin filaments (F-actin), microtubules (MTs), and intermediate filaments (IFs), which differ markedly in their mechanical properties (Merino-Casallo et al., 2022). Compared with synthetic polymers and even many other biopolymers, these filaments exhibit exceptionally high bending stiffness relative to their cross-section (Wen & Janmey, 2011). Before discussing how the cytoskeletal network orchestrates cell migration, we briefly introduce the individual filament systems and highlight their mechanical features.

### 1.2.1 Actin filaments

Actin is among the most abundant and evolutionarily conserved proteins in eukaryotic cells, present from simple organisms such as budding yeast and amoebae to the most complex like humans (Lee & Dominguez, 2010; Fritz-Laylin & Titus, 2023). Filamentous actin (F-actin) assembles from ATP-bound globular actin (G-actin) into a right-handed, double-helical polymer with a diameter of approximately 7 nm (Wen & Janmey, 2011). Each filament is polar, with a fast-growing barbed end (+ end) and a slower-growing pointed end (– end) (Pollard, 2019). After incorporation into the filament, actin subunits hydrolyse bound ATP, and subsequent phosphate release promotes filament ageing and favours disassembly. This nucleotide-dependent turnover underlies treadmilling, in which subunit addition at the barbed end is balanced by subunit loss from the pointed end. In cells, actin-binding proteins further regulate, cross-link, and organize these dynamic filaments into viscoelastic networks, such as those driving rapid lamellipodial protrusion (Mogilner & Oster, 1996).

Polymerising actin networks generate protrusive force through a *Brownian-ratchet* mechanism (Peskin et al., 1993). The actin cortex lies just behind the plasma membrane of the cell. Thermal fluctuations transiently separate the plasma membrane from the barbed ends of actin filaments, and provided a sufficient pool of G-actin, new monomers can insert into the gap. The added subunit prevents the membrane from returning to its previous position, thereby rectifying random dynamics into directed motion. A dense, treadmilling and cross-linked filament array can collectively exert forces on the order of 200 pN against the membrane, as established by theoretical estimates and *in vitro* measurements (Mogilner & Oster, 1996).

This remodelling is orchestrated principally by the Rho family of proteins (see Section 1.3), while a diverse suite of actin-binding proteins then regulates the processes such as filaments nucleation, elongation, cross-linking, or disassembly and contraction of the actin-myosin network (figure 1.2a) (Merino-Casallo et al., 2022):

- **Formins** attached to barbed ends *promote* the addition of G-actin subunits, favouring formation of long, unbranched filaments.
- **Fascin** bundles parallel filaments, stiffening protrusive structures such as filopodia.
- **Cofilin** binds older, ADP-rich segments near pointed ends, accelerating disassembly and liberating G-actin.
- The **Arp2/3 complex** nucleates daughter filaments at an angle of  $\sim 70^\circ$  to existing ones, creating densely branched networks that push the membrane forward.
- **Capping proteins** (e.g. CapZ, gelsolin) bind barbed ends and *terminate* elongation, thereby controlling filament length and turnover.
- **Myosin-II** minifilaments “walk” toward barbed ends on antiparallel filaments, generating contractile tension within the network.
- **Integrin** clusters at the plasma membrane couple the actin cytoskeleton to the extracellular matrix via adaptors including **talin** and **vinculin** (Hynes, 2002), providing traction and enabling forces to translate into cell-scale movement.

Single actin filaments exhibit a persistence length of 10–17  $\mu\text{m}$ , comparable to the diameter of many mammalian cells such as neutrophils or lymphocytes. Their bending rigidity is roughly  $\kappa \simeq 2\text{--}7 \times 10^{-26} \text{ Nm}^2$  (Gittes et al., 1993). Owing to their high length-to-diameter ratio, actin polymers form percolating, gel-like networks at concentrations as low as  $\sim 0.05\%$  (w/v) (Wen & Janmey, 2011). In most motile cells this network condenses into a cortical layer 50–100 nm thick beneath the plasma membrane, thereby sustaining cortical tension (Dai et al., 1999).

### 1.2.2 Microtubules

Microtubules (MTs) are cytoskeletal polymers assembled from heterodimers of  $\alpha$ - and  $\beta$ -tubulin. Linear stacks of these dimers form protofilaments, which associate laterally (typically 13 dimers *in vivo*) to create hollow cylinders of 25 nm outer diameter (Cooper & Hausman, 2000). Polymerisation occurs predominantly at the plus end, with growth rates of several  $\mu\text{m min}^{-1}$ , while the minus end is usually anchored at a microtubule-organising centre. Shortly after a dimer incorporates into the lattice, GTP bound to the  $\beta$ -tubulin subunit is hydrolysed to GDP, weakening longitudinal contacts. Stochastic loss of the stabilising “GTP cap” triggers so called *catastrophe*: a rapid transition from growth to shrinkage. Contrary, so called *rescue* events allow shrinkage to revert to growth. This behaviour, termed *dynamic instability*, drives continual cycling between elongation and shortening (Mitchison & Kirschner, 1984).

Compared with F-actin, MTs exhibit a flexural rigidity of  $\approx 2.2 \times 10^{-23} \text{ Nm}^2$ , corresponding to a persistence length greater than 1 mm (Gittes et al., 1993). Treating an MT as a hollow cylinder of constant cross-section yields an effective Young modulus of  $\sim 1 \text{ GPa}$  (comparable to Plexiglas) which renders microtubules effectively rigid on the length scale of most eukaryotic cells.

Rather than forming dense meshes, microtubules radiate from a centrosome toward the cortex. Centrosome is microtubule-organising centre, usually located near the nucleus (figure 1.2b). By spanning over the cell body and peripheral protrusions, MT high stiffness stabilises lamellipodia and filopodia (Merino-Casallo et al., 2022), this however does not apply to *Dictyostelium* cells, which will be discussed later (see section 1.4.2). In addition, the MT lattice can serve as a highway for kinesin- and dynein-driven vesicle transport, delivering signalling complexes and other necessary factors to the leading edge and thereby reinforcing polarization (Wittmann et al., 2003).

### 1.2.3 Intermediate filaments

Intermediate filaments (IFs) assemble from staggered, antiparallel tetramers that pack laterally into eight-protofilament ropes, producing filaments of roughly 10 nm diameter (figure 1.2c) (Coelho-Rato et al., 2024). Unlike F-actin and microtubules, IFs possess a short persistence length (0.3–1  $\mu\text{m}$ , depending on isoform) and yet can withstand large axial strains, extending elastically to more than twice their resting length (Wen & Janmey, 2011). These mechanical traits make them well suited to accommodate the rapid shape changes that accompany continuous protrusion–retraction cycles while bearing substantial tensile loads.

Via cross-linking proteins such as plectin, IFs interconnect with F-actin and microtubules,

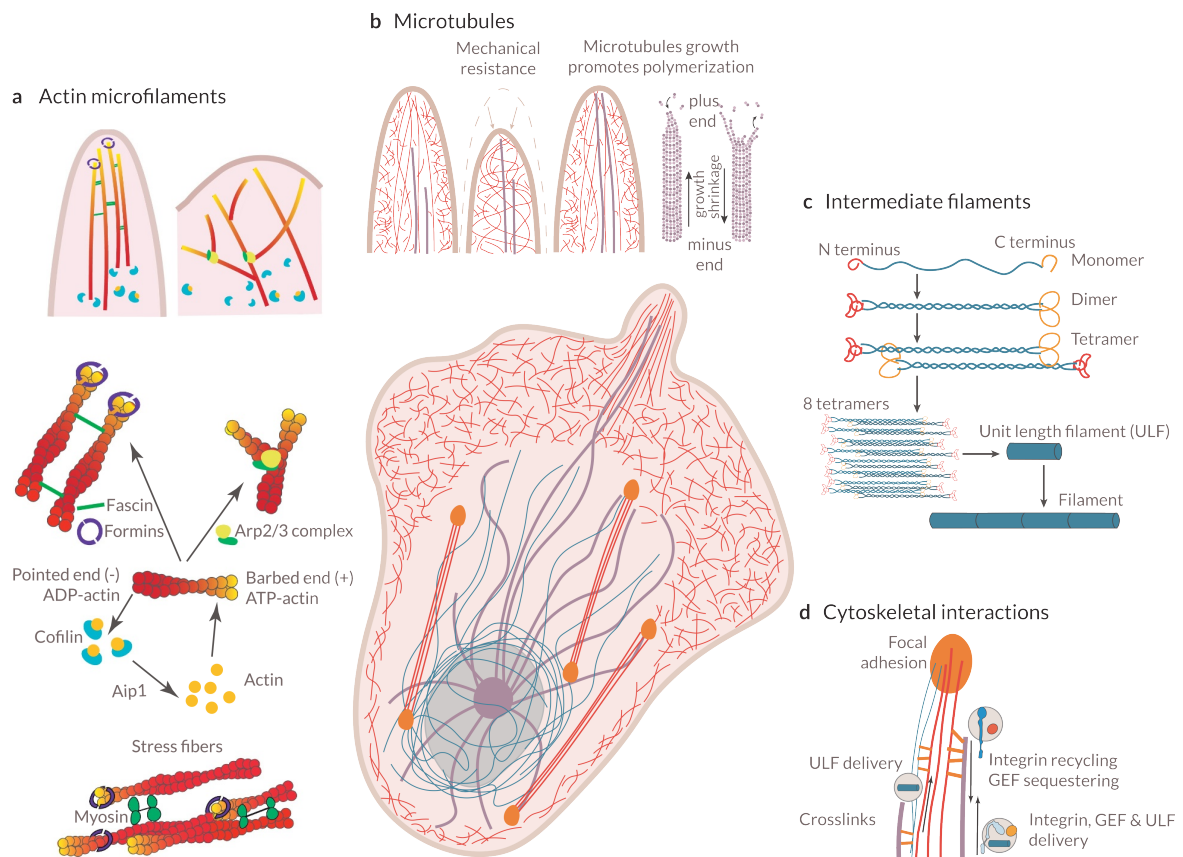


Figure 1.2: Schematic representation of the cytoskeleton and its principal components. Actin filaments and actin-binding proteins (a), microtubules (b), and intermediate filaments (c). Adapted from Merino-Casallo *et al.* (Merino-Casallo *et al.*, 2022).

reinforcing the composite cytoskeleton (Infante & Etienne-Manneville, 2022). IF networks are especially dense in the perinuclear region, where they buffer nuclear deformations during protrusion–retraction cycles (Coelho-Rato *et al.*, 2024). They also contribute to focal-adhesion stability: vimentin engages the Rac1 guanine-nucleotide-exchange factor Trio, promoting robust adhesions under load (Havel *et al.*, 2015). It should be noted that some cells (like *Dictyostelium discoideum*) lack intermediate filaments completely and some other structures take over the needed functions. This will be further explained in section 1.4.2.

### 1.2.4 Emergent mechanics of the cytoskeletal network

Having introduced the three filament systems, we now examine how their concerted interactions drive cell motility. As outlined in Section 1.1, a migrating cell first establishes front–rear polarity, creating distinct cytoskeletal structures at the leading and trailing edges. The polarised cell

then extends a lamellipodium at the front, assembles new focal adhesions (FAs) beneath it, and concurrently disassembles adhesions at the rear. The cycle concludes with actomyosin-driven contraction of the trailing cortex. Each step requires the coordinated integration of the intrinsic mechanics of actin, microtubules, and intermediate filaments, with the emergent properties of their composite network (Sackmann et al., 2010).

At the leading edge, polymerising F-actin generates the protrusive force that extends the lamellipodium, whereas microtubules (MTs) serve chiefly as stiff guidance scaffolds. So called “Pioneer” MTs grow more persistently in the front than in the rear (Wittmann et al., 2003; Jimenez et al., 2021). Reciprocal coupling between the two systems is mediated by the Rho-effector formin mDia1 and the spectraplakins ACF7, which steer MT plus-ends along actin bundles toward the cortex (Ishizaki et al., 2001; Palazzo et al., 2001; Wu et al., 2008; Ning et al., 2016). Conversely, the plus-end-tracking protein EB1 recruits a CLIP-170-mDia1 complex that nucleates new actin filaments directly at the edge (Henty-Ridilla et al., 2016; Seetharaman & Etienne-Manneville, 2020). Dense branched actin can slow MT polymerisation or trigger catastrophes (Colin et al., 2018), establishing a negative feedback that constrains protrusion width.

Recent experiments reveal that IFs interlock with the actin meshwork in the lamellipodium, and position key regulators such as Arp2/3, capping protein, and CARMIL2 (Terriac et al., 2017; De Pascalis et al., 2018; Lanier et al., 2015). Vimentin depletion leads to excessive stress-fibre formation and loss of lamellipodial actin (Jiu et al., 2017), while vimentin filaments laterally stabilise neighbouring MTs against depolymerisation (Schaedel et al., 2021). Dynein- and kinesin-driven transport of IF precursors along MTs continually replenishes the vimentin pool at the front (Helfand et al., 2002; Hookway et al., 2015; Leduc & Etienne-Manneville, 2017), providing positive feedback. Newly recruited IFs tether to FAs and cortical actin near the membrane (Infante & Etienne-Manneville, 2022).

Nascent FAs assemble beneath the lamellipodium, whereas those at the rear disassemble. Vimentin filaments inserted into FAs, tune both their size and mechanical strength (Terriac et al., 2017; Maniotis et al., 1997). MTs repeatedly target large, rear-flank adhesions; such MT “hits”, together with vimentin strands that bridge the actomyosin network to integrins (Seetharaman & Etienne-Manneville, 2019; Infante & Etienne-Manneville, 2022), provide routes for force redistribution and signalling cues that determine whether an FA matures or disassembles. Histone deacetylase 6-mediated de-acetylation of tubulin has been proposed to reorganise vimentin and remodel the IF network at these sites (Rathje et al., 2014).

Finally, at the trailing edge, non-muscle myosin-II contracts actin stress fibres to retract the rear (Weißenbruch & Mayor, 2024), while IF mechanics modulate this contractility: on soft

extracellular matrix (ECM) vimentin damps global tension, whereas on stiff ECM it amplifies stress by stabilising compressed MTs (Alisafaei et al., 2024). Single-filament studies show that IF–MT crosslinkers stabilise NM-II-bearing stress fibres, ensuring that contractile work is channelled into substrate traction rather than dissipated internally (Katsuta et al., 2023).

Throughout the motility cycle, actin, MTs, and IFs form a distributed, load-bearing lattice: F-actin and MTs generate rapid, reversible forces, whereas IFs act as an elastic safety net that prevents ruptures during large deformations (Infante & Etienne-Manneville, 2022). Although embedding stiff MTs in an actomyosin gel can transform a fast, chaotic network into a slower, self-synchronised “muscle-like” actuator (Lee et al., 2021), these filaments alone cannot coordinate movement. Instead, global front–rear asymmetry, established and maintained by the Rho-family GTPases, organises the three filament systems into functional sub-networks with the required mechanical properties (Houk et al., 2012). In the next section we quantify how GTPase gradients modulate cortical tension and protrusive pressure, linking biochemical polarity to the physical behaviour of the cortex.

## 1.3 Cytoskeleton organisation by small GTPases

To distinguish front from rear, a migrating cell must relay spatially resolved signals to each region of the cortex. This polarity is mediated by the Rho family of small GTPases (Nobes & Hall, 1995) together with their dedicated regulators and downstream effectors (Heasman & Ridley, 2008). Members of this family are conserved throughout eukaryotes, from budding yeast and amoebae to animals (Jaffe & Hall, 2005). Acting as molecular switches, they cycle between an **inactive** GDP-bound state in the cytosol and an **active** GTP-bound state at membranes, where they recruit effectors that remodel the actin, microtubule, and intermediate-filament networks. The influence of small GTPases on cytoskeletal organisation is relayed through a well-defined signal-transduction pathway (Jaffe & Hall, 2005). Beyond motility, they coordinate a broad spectrum of processes across the cell cycle, including cytokinesis, vesicle trafficking, and morphogenesis (Heasman & Ridley, 2008).

### 1.3.1 Rho-family GTPases as molecular switches and their regulators

The Rho family comprises small (20–25 kDa) guanine-nucleotide-binding proteins such as Cdc42, Rac1, and RhoA. They operate as conformational **switches**: binding of guanosine triphosphate (GTP) places the GTPase in an **active** state, whereas hydrolysis of the nucleotide to guanosine diphosphate (GDP) returns it to an **inactive** conformation (Mosaddeghzadeh &

Ahmadian, 2021; Jaffe & Hall, 2005). Although the free energy released by GTP hydrolysis is lower than that of ATP, it is sufficient to drive the protein structure rearrangements required for binding with downstream effectors. These downstream proteins contain one of several Rho-GTPase-binding domains (GBDs), and regulate one or more processes related to actin organisation, cell-matrix adhesion, microtubule dynamics, gene expression, and cell-cycle progression (Jaffe & Hall, 2005).

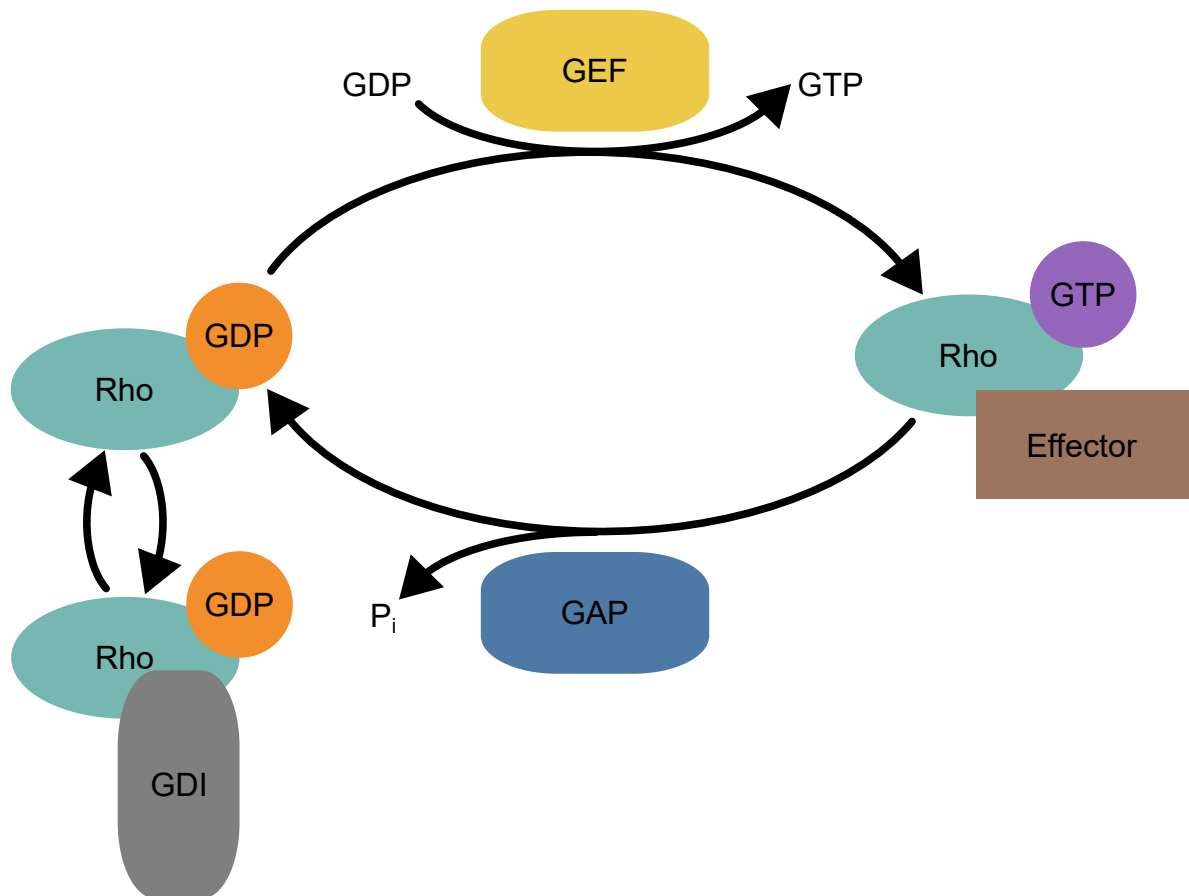


Figure 1.3: Schematic representation of canonical regulation of Rho-family GTPases by GEFs, GAPs, and GDIs. Adapted from Jaffe & Hall (Jaffe & Hall, 2005).

Three main classes of regulatory proteins control the GDP ↔ GTP exchange (figure 1.3):

- 1. Guanine-nucleotide-exchange factors (GEFs)** catalyse the exchange of GDP for GTP (Hart et al., 1991; Cook et al., 2014), thereby switching the GTPase into its active state. Most RhoGEFs contain a conserved Dbl-homology (DH) domain (Cook et al., 2014). Roughly 70 RhoGEFs, belonging to Dbl family are encoded in the human genome (Mosaddeghzadeh & Ahmadian, 2021). Additional lipid-binding motifs, PH or BAR domains, and scaffolding modules facilitate GEF signalling to specific complexes or areas of the

membranes (Mosaddeghzadeh & Ahmadian, 2021; Ohashi et al., 2024). This diversity permits distinct upstream cues to activate the same Rho GTPase in different contexts. For example, mechanical stress at cell-cell or cell-matrix junctions can recruit select GEFs that activate RhoA (Ohashi et al., 2024).

2. **GTPase-activating proteins (GAPs)** accelerate the intrinsic rate of GTP hydrolysis (Rittinger et al., 1997; Amin et al., 2016). About 70 RhoGAPs are present in humans. A conserved  $\sim 190$ -residue GAP domain provides an “arginine finger” that stabilizes the transition state of hydrolysis (Mosaddeghzadeh & Ahmadian, 2021). The nearly one-to-one ratio of GTPases to GAPs implies tight regulation to prevent inadvertent switch-off events. Similar to GEFs, lipid-binding motifs, BAR domains, and other interaction zones tune localization and responsiveness of GAPs (Amin et al., 2016). Their function encompasses mediation of actin disassembly, endocytic trafficking, and morphogenesis, while some (e.g. DLC1/2/3) behave as mechanosensitive dampers at focal adhesions (Amin et al., 2016; Frey et al., 2025).
3. **Guanine-nucleotide-dissociation inhibitors (GDIs)** isolate prenylated Rho GTPases in the cytosol by binding their hydrophobic C-termini with the targeted protein (Keep et al., 1997; Garcia-Mata et al., 2011). Only three RhoGDI isoforms exist in humans (Mosaddeghzadeh & Ahmadian, 2021). GDIs can extract both GDP- and GTP-loaded GTPases from membranes-though they preferentially bind the GDP form, and thus maintain the cytosolic pool largely inactive (Garcia-Mata et al., 2011; Golding et al., 2019). Single-molecule imaging shows that active Rho GTPases occupy tiny membrane patches, while GDIs continually cycle them between membrane and cytosol, forming inhibitory GDI-GTPase complexes in various cell compartments (Mosaddeghzadeh & Ahmadian, 2021). Besides trafficking and protection from degradation, GDIs can as well modulate crosstalk among different Rho GTPases (Boulter et al., 2010).

### 1.3.2 Effector pathways downstream of Rho-family GTPases

Once bound to GTP, the canonical switches RhoA, Rac1, and Cdc42 recruit more than 70 known **effectors**. This subsequent interactions allow active GTPases to facilitate directed motility as well as other intracellular processes (Mosaddeghzadeh & Ahmadian, 2021). Bellow are condensed signalling pathways that matter most for cell motility.

- **Cdc42**→**N-WASP**→**Arp2/3**. Active Cdc42 binds N-WASP, relieving its autoinhibition. The exposed VCA motif docks both Arp2/3 and G-actin, accelerating Arp2/3-mediated branching and polymerization  $\sim 30$ -fold thus driving filopodia and lamellipodial actin

networks (Rohatgi et al., 1999).

- **Rac1→WAVE complex→Arp2/3.** Rac1 allosterically activates WAVE1/2 complexes (via Nck/Sra1/Nap1 subunits), producing broad lamellipodia (Eden et al., 2002; Innocenti et al., 2004). Together, Rac1 and Cdc42 converge on Arp2/3 to seed dense, rapidly treadmilling actin.
- **Rac1→Capping proteins.** Rac1 additionally promotes barbed-end elongation by uncapping filaments and boosting the local G-actin pool through cofilin-gelsolin regulation (Heasman & Ridley, 2008).
- **RhoA→mDia1.** Binding of RhoA–GTP unlocks the formin mDia1, which processively adds actin subunits to create long, unbranched filaments—the backbone of stress fibres (Watanabe et al., 1999; Narumiya et al., 2009).
- **RhoA→ROCK→MLC & LIMK.** Rho-associated kinase (ROCK) phosphorylates (i) myosin-II light chain, activating contractility and thereby regulating the cortical tension, and (ii) LIM kinase, which inactivates cofilin and thereby stabilises newly formed filaments (Maekawa et al., 1999). This dual pathway turns the mDia1 scaffold into a tension-bearing stress fibre while simultaneously maturing focal adhesions (Watanabe et al., 1999; Ning et al., 2024).
- **IQGAP1.** This large scaffold binds F-actin, captures growing MT plus-ends via CLIP-170, and associates with E-cadherin/ $\beta$ -catenin at adherens junctions (Fukata et al., 2002; Noritake et al., 2004). IQGAP1 can both harbour (and locally stabilise) active Rac1/Cdc42 and recruit Arp2/3 or Dia1, making it a hub where branched and linear nucleation intersect (Brandt & Grosse, 2007).
- **PAKs (p21-activated kinases).** Rac1/Cdc42 binding releases PAK autoinhibition, enabling phosphorylation of (i) MLC and MLCK (modulating tension), (ii) LIMK (stabilising leading-edge actin), and (iii) vimentin (promoting IF disassembly and protrusion) (Bokoch, 2003; Helfand et al., 2011). PAKs therefore tune both protrusive actin dynamics and rear-edge contractility. Loss of PAK1 produces erratic, low-persistence migration (Sells et al., 1999).

To summarize, Rho GTPases act as spatial “selectors” that:

1. trigger rapid, branched actin growth at the front (Rac1/Cdc42→Arp2/3);
2. assemble and contract actomyosin network at the rear (RhoA→mDia1/ROCK);
3. coordinate crosstalk between actin, microtubules, and intermediate filaments via scaffolds such as IQGAP1 and PAKs.

This biochemical polarization drives mechanical processes described in section 1.2.4: protrusive forces and cortical tension are simply two sides of one regulatory group. Many additional Rho-effectors (Citron kinase, Rhotekin, DOCKs, etc.) participate in cytokinesis, vesicle traffic,

and morphogenesis, but are omitted here for brevity.

### 1.3.3 Emergent oscillatory dynamics of Rho GTPases

Spatially patterned dynamics of Rho-family GTPases can arise without an external cue given two prerequisites are satisfied: local positive feedback, typically a GEF that is itself recruited by active GTPase and delayed negative feedback provided by GAPs or substrate protein depletion. In terms of reaction–diffusion dynamics two minimal schemes relate the underlying process (figure 1.4) (Halatek et al., 2018; Bement et al., 2024):

- 1. Activator–inhibitor:** the activator (GTPase-GEF complex) autocatalytically amplifies itself, while a faster-diffusing inhibitor (GAP) quenches activity at longer spatial range.
- 2. Activator–depletion:** the activator consumes a common substrate (GDP-loaded GTPase). Rapid diffusion of the substrate refuels active sites and sustains local peaks.

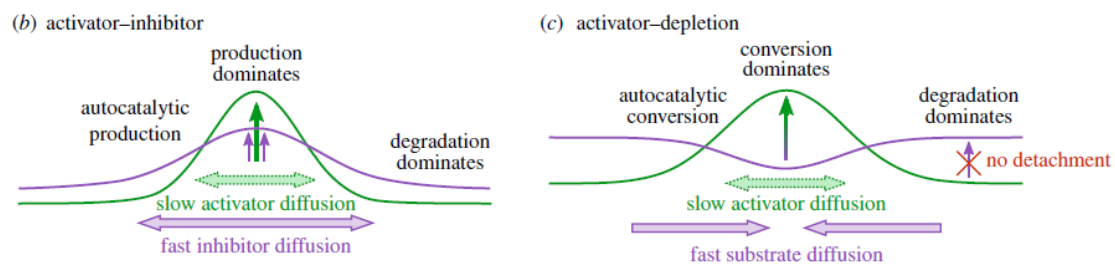


Figure 1.4: Schematic representation of activator-inhibitor and activator-depletion dynamics. Adapted from Halatek & Frey (Halatek et al., 2018).

There exists a growing number of experimental evidence supporting this reaction–diffusion activity of GTPases. We briefly present few of them:

- **Pole-to-pole Cdc42 oscillations** in budding yeast cycle every  $\sim 2$  min as GEF-mediated activation outruns GAP-driven inhibition (Das et al., 2012).
- **Pulsed RhoA contractility** with a period of  $\sim 30$  s drives cortical contractions in *C. elegans*. Positive feedback comes from the RhoGEF ECT-2, while negative feedback is provided by actin-recruited RGA-3/4 (Michaux et al., 2018).
- **Traveling RhoA waves** and spirals in mammalian cells require GEF-H1-dependent activation opposed by multiple GAPs (Graessl et al., 2017).

Furthermore active RhoA was observed in triggering actomyosin contractility, with the resulting cortical flows, in turn, advecting and stretching the chemical patterns. Chen *et al.* (Chen et al., 2024) demonstrated that increasing RGA-3/4 (GAP) switches the system from pulsatile to wave-like regimes. Beyond a threshold, chemical oscillations outpace mechanical relaxation

and the two become uncoupled. Elevated cofilin, which accelerates F-actin turnover, can restore coupling by lowering the mechanical time-scale, illustrating how cytoskeletal rheology tunes pattern dynamics.

Rho GTPases constitute an excitable medium whose intrinsic reaction–diffusion kinetics produce pulses, waves, and spirals. Because the same molecules also modulate cytoskeletal organization, these chemical patterns directly map onto mechanical ones: zones of high RhoA correspond to actomyosin contractions, whereas Rac1/Cdc42 peaks specify protrusive growth. Maintaining coherent cell migration therefore requires a tight balance between chemical feedback loops and the viscoelastic response of the cortex.

## 1.4 *Dictyostelium discoideum*: a model organism

In this section, we present a model organism used extensively to study cellular processes (Annesley & Fisher, 2009). These amoebas are known for their exceptional motility. Furthermore, their cytoskeletal arsenal is simplified in relation to the full cytoskeletal network introduced in previous sections. These features of *Dictyostelium discoideum* make it an excellent case study for testing numerical models of cell locomotion. Below we introduce characteristics of this organism and present specificities of its life-cycle, genetics, cytoskeleton and regulatory proteins extracting from the general picture presented before.

*Dictyostelium discoideum* is a social, soil-dwelling amoeba that preys on bacteria. In the vegetative (nutrient-replete) state, single cells grow to 10–20  $\mu\text{m}$  in diameter (Annesley & Fisher, 2009). Starvation triggers the secretion and relay of cyclic adenosine monophosphate (cAMP), prompting chemotactic migration toward aggregation centres. The resulting aggregate, or *mound*, matures by forming a tip while the cells differentiate into two major lineages: prestalk and prespore. Through secretion of an extracellular matrix, the cells adhere to one another and form a migratory multicellular *slug* that typically measures  $\sim 1$  mm in length (Bozzaro, 2019). Slugs exhibit photo- and thermotaxis, locomoting toward illuminated, drier regions that favour efficient spore dispersal (Fisher & Williams, 1982). When conditions permit, the slug undergoes culmination, first adopting a “Mexican-hat” shape and then erecting a fruiting body in which prestalk cells form the stalk while prespore cells mature into spores (Bozzaro, 2019; Schaap, 2011). A single migrating slug can comprise up to  $\sim 10^5$  cells, of which roughly 80% become spores (Annesley & Fisher, 2009). A schematic of this life cycle is shown in figure 1.5.

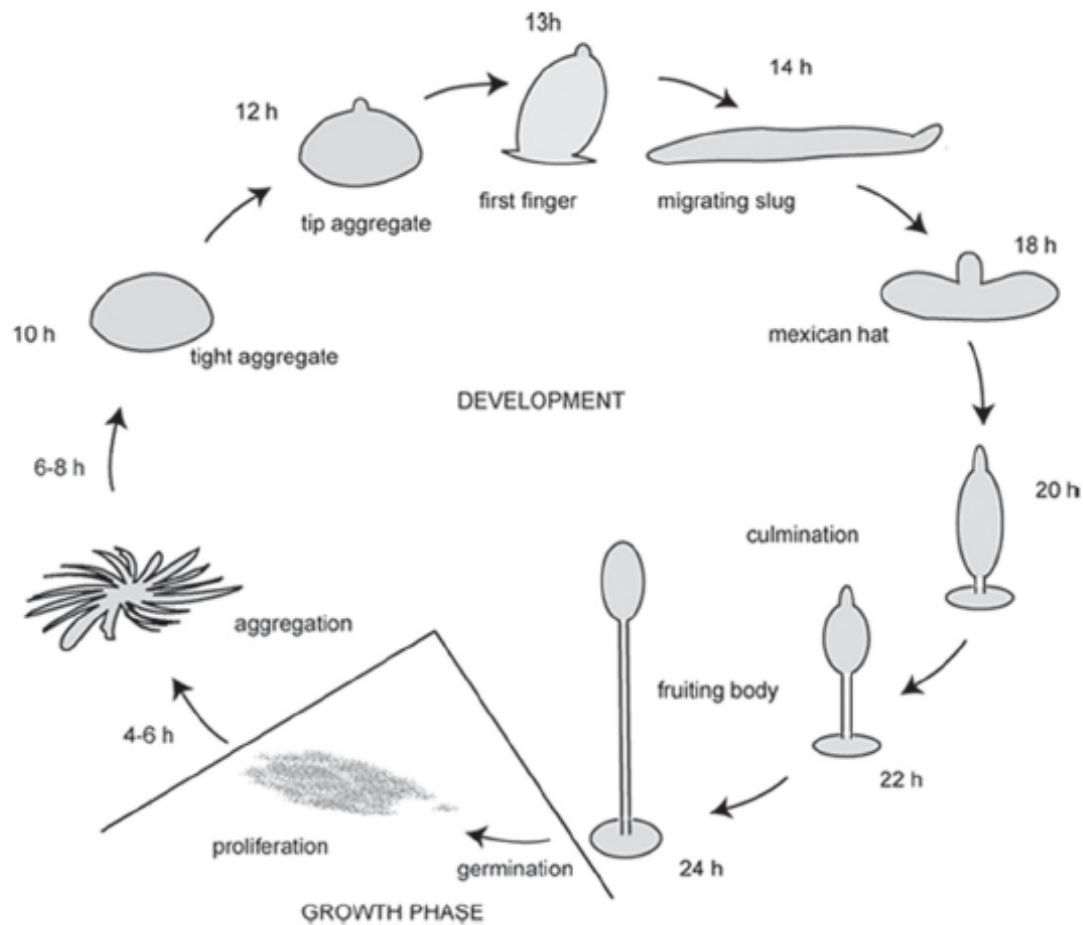


Figure 1.5: Schematic representation of the *Dictyostelium discoideum* life cycle. Adapted from Bozzaro (Bozzaro, 2019).

### 1.4.1 Genomic and experimental advantages

The life cycle of *D. discoideum* reflects its haploid genetics: every developmental transition is executed by haploid cells that directly express existing mutations. It was also the first free-living protozoan to have its genome completely sequenced, the nuclear genome spans 34 Mbp across six chromosomes (Eichinger et al., 2005). This compact genome, combined with efficient homologous recombination and, more recently, CRISPR/Cas9 editing-enables rapid generation of strains with over-expressed proteins or knockout strains. Although *Dictyostelium* diverged from the metazoan lineage more than one billion years ago, roughly two-thirds of its proteome has clear human orthologues, including most cytoskeletal and signalling components, making it a powerful surrogate for exploring mechanisms relevant to human disease.

All stages of the *Dictyostelium* cycle, from bacterial foraging to chemotactic aggregation,

slug migration, and culmination, depend on finely tuned cell motility. The organism is therefore ideally suited for studying actin-myosin dynamics and their upstream regulators. Cells are relatively large and optically transparent, facilitating high-resolution live imaging. Behavioral contrasts between nutrient-replete and starved cells are especially revealing: vegetative cells execute frequent turns and thus show low net displacement, whereas starved cells suppress turning and increase their mean run length roughly 30-fold even in the absence of an external cAMP gradient (Van Haastert & Bosgraaf, 2009). These shifts in migration program highlight the coupling between intracellular signalling and cytoskeletal mechanics.

### 1.4.2 Cytoskeleton of *Dictyostelium discoideum*

Compared with mammalian cells, *Dictyostelium discoideum* possesses a streamlined cytoskeletal toolkit that is optimised for rapid amoeboid locomotion (Pears & Gross, 2021). Below we revisit the three filament systems introduced in section 1.2, emphasising both the simplifications unique to *Dictyostelium* and the emergent mechanical behaviour that follows.

*Dictyostelium* completely lacks canonical IF proteins (Annesley & Fisher, 2009). Nuclear rigidity is instead provided by the lamin-like protein NE81, whereas cytoplasmic load bearing comes from a dense actomyosin cortex cross-linked by talin and cortexillin (Gräf et al., 2025). Talin links F-actin to the membrane, talin-null mutants show a 5-fold drop in envelope bending stiffness and lose the normal front-rear tension asymmetry (Merkel et al., 2000). In essence, a rapidly turning-over actomyosin gel substitutes for the elastic safety net that IFs supply in higher eukaryotes.

A single centrosome containing  $\gamma$ -tubulin nucleates a modest radial array of MTs (Gräf et al., 2021). This sparse network can be reorganised within seconds, supporting swift shape changes. MTs help position the nucleus and sustain polarity; nocodazole-treated cells remain motile but exhibit erratic trajectories and poor persistence (Yoshioka et al., 2011; Ishikawa-Ankerhold et al., 2022). Thus, while dispensable for force production, MTs are key organisers of the polarity circuitry that sustains directed crawling.

*Dictyostelium* forms tiny, short-lived SibA-family adhesions ( $\sim 15 - 20$  s lifetime) and entirely lacks integrins (Mijanović & Weber, 2022). Without integrins, IFs, or stable adhesions, classic acto-myosin stress fibres do not form (Sackmann et al., 2010). Traction instead derives from an isotropic actomyosin cortex that can redirect force within a fraction of a second.

The genome encodes a single myosin-II heavy chain that assembles into short cortical filaments, in addition to  $\gtrsim 12$  class-I myosins (Bozzaro, 2019). Myosin-II filaments are transient, and motility persists in myosin-II knock-outs. Class-I motors can compensate the lack of

myosin-II, albeit with reduced efficiency of rear retraction (Lee & Dominguez, 2010).

Individual, F-actin, cortical filaments are short ( $\sim 0.2 \mu\text{m}$ ) and randomly oriented. Depolymerising F-actin with latrunculin A raises whole-cell deformability 10-fold (Girard et al., 2006). Wild-type cortical tension is  $0.1 - 0.4 \text{ nN}\mu\text{m}^{-1}$  (Dai et al., 1999), among the highest measured for motile cells. Myosin-II-null mutants display a three-fold drop in peak traction stress and a nearly uniform, low-tension cortex (Lombardi et al., 2007). Overexpressing class-I myosins or filamin stiffens the cortex, while loss of filamin yields a compliant shell and unstable pseudopods (Merkel et al., 2000).

Traction-force microscopy reveals a stereotyped mechanical polarity: high contractile stress under the rear and low stress at the front (Lombardi et al., 2007). When the pattern becomes symmetric the cell stalls, with rapid rear detachment letting stored tension snap the cell body forward. Micropipette aspiration confirms this polarity, frontal cortex is softer than at the rear, a difference abolished in talin-null cells (Merkel et al., 2000). Together, polymerisation-driven pushing at the front and myosin-II contractility at the back form a self-organised “push-pull” mechanism analogous to the composite mechanics described in Section 1.2.4, but executed with a radically simplified protein repertoire.

By stripping away IFs, integrins, and extensive MT scaffolds, *Dictyostelium* trades structural redundancy for speed and plasticity. A thin, contractile actomyosin shell, cross-linked by talin and dynamically tuned by class-I and class-II myosins, assumes the dual role of propulsion and structural integrity. Given together these amoebae can outrun and out-manoeuvre far more complex cells.

### 1.4.3 Rho GTPase signalling in *Dictyostelium discoideum*

Similar to its streamlined cytoskeletal components, the regulators of cytoskeleton are also simplified in these amoebae. Unlike mammalian cells, *Dictyostelium discoideum* lacks a canonical Cdc42 homologue. Rho GTPase regulation tasks, normally split between Cdc42 and Rac1, are reassigned to an expanded Rac sub-family (Filić et al., 2021). The genome encodes  $\sim 20$  Rho-family members, all annotated as “Rac”, implying sub-functionalisation to cover the full spectrum of signalling demands (Rivero & Xiong, 2016). Of particular interest are the three paralogues Rac1A, Rac1B, and Rac1C, which share  $>90\%$  amino-acid identity (Filić et al., 2021). Overexpression of wild-type Rac1 drives exuberant actin-rich protrusions (filopodia, lamellipodia, membrane ruffles) and boosts both motility and endocytosis (Dumontier et al., 2000).

Bellow we list the main differences between isoforms. First, Rac1A is abundant throughout

the life cycle, whereas Rac1B/C peak only during aggregation and sexual maturation (Filić et al., 2021). Furthermore, single knock-out of Rac1A slows, but does not abolish, motility, while Rac1B nulls show mild developmental defects. All three isoforms partition between cytosol and plasma membrane; membrane-bound Rac shows enrichment, which is strongest at emerging protrusions and ruffles (Filić et al., 2012; Rivero & Xiong, 2016). In motile cells Rac1A localises to nascent pseudopods and endocytic cups, the functional analogue of lamellipodia in fibroblasts (Faix & Weber, 2013; Rivero & Xiong, 2016).

Chemoattractant cAMP induces rapid, F-actin-dependent Rac1A activation at the leading edge (Filić et al., 2014). However, external cues are not essential: vegetative cells exhibit spontaneous Rac1A bursts at random pseudopods (Filić et al., 2014; Marinović et al., 2016; Šoštar et al., 2024). Live-cell microscopy with fluorescent probes reveals active Rac1A domains that periodically relocate, either rotating around the cortex or flipping to the opposite side, every 2–5 min in freely crawling vegetative cells (Šoštar et al., 2024). Rear-localised Rac1A forms a complex with DGAP1 and cortexillin to stiffen the tail, whereas front-localised Rac1A engages the Scar/WAVE complex to drive protrusion (Filić et al., 2012; Faix & Weber, 2013). Thus identical switches elicit opposite mechanical outcomes depending on cortical context.

The Rac1A oscillations described here, together with the broader oscillatory motifs discussed in Section 1.3.3 and the mechanical asymmetries presented in Section 1.2.4, provide quantitative benchmarks for the mechanochemical model developed in Chapter 2. Before constructing that reaction–diffusion framework coupled with mechanical deformations, the next section surveys existing models of cellular motility and signalling dynamics.

## 1.5 Existing models of cell migration and polarization

Modelling cell motility is a complex problem that requires addressing multiple coupled processes, including the reorganization of the actin cytoskeleton, forces generated by polymerizing actin filaments, contractile forces produced by myosin type-II molecular motors, cortical tension, and the signalling pathways regulating cytoskeletal dynamics, as introduced in the previous section. Our main goal is to create a minimal model of cell locomotion which encompasses all of the aforementioned processes. Before presenting the model used for simulating locomotion, we first review the current state-of-the-art computational models and different approaches available. A variety of approximations and computational techniques can be employed to model each of these processes with varying levels of complexity and precision.

### 1.5.1 Polarization models

Since Turing's pioneering work (Turing, 1952), which demonstrated that two interacting and diffusing substances can form stable spatial patterns in their concentration distribution, reaction–diffusion (RD) systems have become an indispensable approach for modelling numerous biological processes. Moreover, RD systems extend Turing's original idea by revealing not only stationary but also time-dependent dynamics, which can explain some cyclic biological processes (Beta & Kruse, 2017). It has been shown that RD systems based on known interactions of the Rho family of GTPases and related proteins can explain stable polarization (Jilkin et al., 2007; Otsuji et al., 2007) as well as oscillatory dynamics (Bement et al., 2015; Chiou et al., 2018; Šoštar et al., 2024) in live cells.

Given that RD systems inherently produce ordered, time-dependent protein dynamics resembling those observed experimentally (Šoštar et al., 2024), it is often sufficient to construct a reaction network heuristically, even if it is not directly linked to known protein interactions. One such example is the Excitable Signal Transduction Network model developed by Devreotes *et al.* (Devreotes et al., 2017), a condensed version of which was employed in work by Shi *et al.* (Shi et al., 2013). Their model successfully replicates many experimentally observed cell shapes and motility dynamics, despite being constructed heuristically from the general behaviour of RD systems rather than by explicitly modelling known Rho family protein interactions. However, it should be noted that the authors do propose plausible protein interactions that could correspond to their modelled network (Devreotes et al., 2017).

A limitation of the model used by Shi *et al.* (Shi et al., 2013), as well as early RD models such as Turing's original formulation, is that they do not conserve the total number of molecules (or mass) over time. More recent models employ mass-conserved reaction–diffusion (MCRD) systems, which ensure that the total number of molecules remains constant. This approach is supported by the observation that protein synthesis and degradation occur on a much longer time-scale than the oscillatory dynamics exhibited by these systems (Halatek et al., 2018). Additionally, it has been shown that enforcing mass conservation enhances the robustness of RD systems (Moreno & Alonso, 2022). In MCRD systems with well-defined geometry and a constant total protein concentration, all possible steady-state and dynamic solutions can be determined based on the ratio of diffusion coefficients of specific protein species. Furthermore, increasing the number of chemical species or introducing a more complex reaction network does not necessarily result in new emergent system behaviours (Šoštar, 2022). Given these insights, it can be argued that the most effective approach is to use the minimal model capable of reproducing the desired behaviour while ensuring that the necessary reactions align with the available knowledge of the protein interactions governing cell motility.

All of the RD-based approaches mentioned above consistently exhibit three main spatio-temporal patterns relevant to cell locomotion: rotation, oscillation, and polarization (Šoštar et al., 2024; Moreno & Alonso, 2022; Otsuji et al., 2007; Jilkine et al., 2007). In rotation, a travelling concentration wave propagates along the cell cortex; oscillation is characterized by a stationary (standing) wave; and polarization displays a long-lasting, time-invariant profile. These patterns have been widely documented in diverse RD systems, and similar dynamics are observed in the morphological changes of locomoting cells (Maeda et al., 2008; Šoštar et al., 2024). This correspondence between biochemical and mechanical aspects highlights the need to couple RD systems with additional modules that account for mechanical forces, cortical tension, and other key determinants of cell shape. Such integrated approaches provide a more comprehensive framework for understanding how spatio-temporal protein distributions drive the range of locomotion behaviours seen in living cells.

### 1.5.2 Motility models

A variety of models capturing the main components of cell motility have been proposed, ranging from 1D to 3D representations (Holmes & Edelstein-Keshet, 2012; Ziebert & Aranson, 2016; Buttenschön & Edelstein-Keshet, 2020). Main difference of these approaches lies in a way aforementioned forces are incorporated with the RD system and how interface and the position of the cell is tracked. As we will see, different models capture and describe cell's position, shape and forces acting on it with a different computational efficiency and accuracy.

One of the conceptually simplest models was proposed by Kabaso *et al.* (Kabaso et al., 2011). In their approach cells membrane is modelled as a periodic 1D line whose height  $h(x)$  from reference line is tracked. This height depends on the Helfrich free energy as well as the membrane coverage by specific protein species. Despite being 1D model, it is obvious that the height  $h(x)$  can be transformed to a 2D contour of a cell by displacing it from some fixed point which acts as a centroid of a cell. This simple model can account for changes in perimeter of the cell as well as the membrane buckling due to surface tension changes, while its main drawback is that it could incorporate only RD systems on the surface of the cell ignoring the bulk dynamics.

Similarly, another effectively 1D approach was proposed by Neilson *et al.* (Neilson et al., 2010). Again, instead of tracking the whole cell the authors opted to evolve only the interface using Parametrized Finite Element Method (PFEM). This choice effectively reduces the problem to a 1D arclength-based finite element mesh. This approach is similar to the Moving Mesh Finite Element Method (MMFEM), which is commonly used to redistribute nodes when solving partial differential equations (PDEs) based on the gradient of the solution. The authors employ this

technique to evolve the nodes defining the contour of the cell's cortex. The evolution of the contour in the normal direction is governed by a velocity profile dependent on local curvature and signalling molecule concentrations. Meanwhile, the tangential evolution of nodes is controlled by Moving Mesh Partial Differential Equations (MMPDEs), which aim to equidistribute the nodes along the contour.

This presents a challenge itself, because one needs to carefully choose the MMPDE such that the physical properties are captured accurately. A variety of monitor functions can be used to control MMPDE behaviour (Huang & Russell, 2011), and Neilson *et al.* opted for an equidistribution principle to evolve the nodes. This choice has a disadvantage compared to the aforementioned model by Kabaso because it does not capture the surface tension as well as the buckling of the membrane. Like the previous one, this model, also lacks the cytoplasm dynamics and is only tracking the cell's interface.

To address the lack of cytoplasm dynamics of RD systems coupled with cell shape changes, two upgraded models similar to PFEM were proposed (MacDonald *et al.*, 2016; Mackenzie *et al.*, 2019). Both approaches employ explicit bulk and surface tracking by evolving the positions of nodes that define the cell's interior, exterior, and cortex. The main advantage of these so-called Arbitrary Lagrangian-Eulerian (ALE) approaches is their reduced computational cost compared to other high-resolution models, although this comes at the expense of a mathematically complex formulation of the MMPDEs governing node translation. Furthermore, these approaches naturally incorporate the simulation of bulk and surface protein dynamics alongside the model of cell motility. However, similar to the PFEM approach used by Neilson *et al.*, ALE-based models struggle to fully capture membrane tension forces and intracellular forces that influence the bulk nodes. Instead, these models resemble mechanical spring-force approximations. A related approach, which discretizes the contour into a series of material points, appears to be used by Hecht *et al.* (Hecht *et al.*, 2011), though an in-depth analysis of the evolution problem is lacking.

Another type of models that usually incorporate the RD dynamics with the changes in cell shape better than the previously mentioned ones are Cellular Potts Models (CPM). In these models Monte Carlo algorithm is used to evolve the cell's interface and the procedure can be broken down in three main steps (Ziebert & Aranson, 2016): (1) selecting a lattice point to update, (2) accepting or rejecting the update based on the energy change associated with the new state, and (3) applying additional rules to model specific cellular processes. Maree *et al.* (Marée *et al.*, 2012) implemented CPM with a highly complex signalling network, incorporating multiple protein species and their interactions. This highlights the primary strength of the CPM approach-it can be easily coupled with intricate biochemical networks to model a wide range of biophysical processes involved in cell motility, while maintaining a relatively low computational

cost. However, a key limitation of CPM is that its shape evolution dynamics are inherently stochastic, and does not accurately reflect the physical nature of the forces driving cell motility. Additionally, advective fluxes along the cortex and in the cell's bulk are not explicitly modelled. Instead, RD coupled systems behave as though the cell is stationary. Nonetheless, CPM can be easily extended for simulating large populations of cells, making it particularly useful when cell–cell interactions play a significant role.

To address the stochastic nature of shape changes in CPM models, one can employ a Phase field (PF) model. This class of models naturally integrate free energy formulations into their evolution equations, improving the physical description of the system and have been widely used for simulating cell motility (Aranson, 2016; Shao et al., 2012; Alonso et al., 2018; Moreno et al., 2020, 2022). PF models fall into the category of diffuse interface models, meaning that the cell is represented by a smooth phase-field function that transitions gradually across the simulation domain. As a result, the interface has a finite thickness, rather than being a sharp boundary. On the downside, the diffuse interface imposes a lower limit on grid spacing and resolution to ensure accurate representation of the phase-field transition from the cell interior to its exterior.

The drawback of all of aforementioned models lies in the fact that they do not account for the flow inside the cytoplasm which can affect the RD system in moving cells. This can be mitigated by the use of approach similar to PF called the Level-Set (LS) method. Originally developed for simulating phase flow problems (Osher & Sethian, 1988), this approach has been effectively applied to cell migration modelling. The defining characteristic of the LS method is the use of a level-set function (LSF),  $\phi$ , which evolves over time according to the continuity equation:

$$\frac{\partial \phi}{\partial t} + \vec{v} \cdot \vec{\nabla} \phi = 0.$$

The LSF is typically defined as a signed distance function or a linear function, where the cell cortex is represented by the zero-level contour of  $\phi$ . Thus, the cell boundary is naturally embedded within a continuous field. Notably, this formulation assumes that the cortex is a 1D curve with zero thickness. Several studies have successfully employed LS methods for cell motility simulations (Kuusela & Alt, 2009; Shi et al., 2013; Schindler et al., 2024), each incorporating different techniques to model signalling dynamics. The main advantage of the LS approach, particularly compared to previously mentioned methods, is its ability to simulate highly irregular cell shapes and their dynamic deformations. However, a key drawback is the gradual degradation of the LS function over time, leading to errors in the evolution of the cell cortex. This issue necessitates periodic reinitialization of the LSF, which increases computational

costs.

The explicit interface tracking of the LS method can impose challenges by itself especially when trying to incorporate RD systems that have defined surface protein concentration and their diffusion. An alternative approach which combines elements of both LS and PF methods can be used to somewhat address this. As stated by Moure *et al.* (Moure & Gomez, 2016) instead of defining the LSF as a step or linear function, one can use a smooth saturating function, such as a hyperbolic tangent. Although the interface position is still determined by a predefined contour level, it is now diffuse rather than sharp. Additional enhancement to the problem introduced by LS method, is the use of stabilizing LS evolution equation, which effectively corrects and reinitializes the function at every step. This improvement mitigates the inherent degradation problem of LS methods while providing greater control over velocity equations governing cell shape and position.

Most of the aforementioned models can be raised from 1D or 2D to 3D naturally. For FEM approach the major change is the addition of extra dimensions to the matrix equations which does not change the implementation drastically. Similarly CPM, PF, LS models can be generalized to three dimensions by defining the higher dimensional mesh. As modelling cell's in three spatial dimensions seem quite straightforward one could wonder why more models do not use this approach? The answer lies in the fact that inclusion of extra dimension increases computational complexity of the model while not necessarily giving any new insights into the locomotion of live cells. As we are here interested in crawling on the surfaces, cell's are mostly flat in this regime. It can also be shown that the dynamics of the proteins inside the cell can effectively be projected on the plain without the loss of generality.

To summarize, a wide range of modelling approaches exist for simulating both single-cell and multicellular motility. These models vary in both computational and biological complexity, and careful consideration must be given when selecting a specific approach to ensure that it accurately represents the forces and biophysical processes of interest. When modelling signalling pathways, there is somewhat more flexibility, as reaction–diffusion systems inherently exhibit characteristic dynamics that closely resemble experimentally observed behaviours. However, employing a mass-conserved reaction–diffusion system is particularly advantageous due to its increased robustness and ability to capture diverse dynamic behaviours with a limited number of protein species and interactions. While it is possible to construct theoretical models of such systems without direct validation from known protein interactions, the current level of understanding of molecular dynamics within the cell is generally sufficient to justify most reaction expressions used in these models.

## 1.6 Aim of the thesis

With the biological context and modelling approaches introduced, we can now lay out the aim of this thesis. The previous sections outline the complex interactions that drive cell motility. Our goal is to encapsulate the essential principles presented above within a single, self-contained model. To this end, the next chapter presents the model we have developed for this purpose. We chose to adopt diffuse-interface level-set method as it combines the ability of tracking complex shape changes with the inclusion of the flow inside and outside of the cell. Furthermore, diffuse-interface variant allows for convenient localization of the protein species, encapsulated in the reaction–diffusion system, to be incorporated within the model. All the aforementioned features are delineated in the next section. After the definition of the model we proceed by characterising the solution behaviours admitted by the model and highlight emergent features arising from our implementation.

With the model introduced, we shift to analysis of *in vitro* behaviour of the motile amoeba *Dictyostelium discoideum*. By characterising its locomotion, we propose a taxonomy that distinguishes behavioural classes. Using fluorescence readouts from a Rac1-GTP-bound probe, we relate these motility classes to the underlying protein dynamics that orchestrate movement. Our experimental findings frame the central question addressed by this thesis: How does the coupling of signalling dynamics to the shape and structure of the cell cortex generate the observed diversity of behaviours?

To answer this question, we adapt the general model to *Dictyostelium* cells and demonstrate that a wide range of experimentally observed classes can be reproduced within our framework. We show how reaction–diffusion dynamics are modulated by cytoplasmic and membrane-associated flows, and how cell shape influences and mediates intracellular processes. Our results suggest that all components introduced in the model are necessary to efficiently simulate cellular motility.

# Chapter 2

## Model of cell locomotion

In this chapter we present the mathematical framework used to simulate cell motility, describing each constituent module. As introduced in Section 1.5, a complete model of cellular locomotion can be constructed in many different ways, with several alternative formalisms and techniques available for every individual component. Here, we adopt a deliberately minimal approach: we couple a reaction–diffusion–advection (RDA) system for intracellular signalling to an explicit description of cell-body deformation and translation, while keeping the formulation sufficiently simple to facilitate straightforward implementation.

### 2.1 Formulation of the model

In this section we lay out the three main components of the model which allows for simulation of motile cells based on the protein dynamics inside the cell. To track the cell boundary and its evolving shape we employ a diffuse-interface level-set (LS) method. This LS component is coupled to a second module that supplies the velocity field by solving the Navier-Stokes equation; the computed flow advects the LS function. The third module integrates a RDA system on the domain delineated by the LS function, using the Stokes velocity field to prescribe advection of the chemical species. Below, we present the governing equations and numerical schemes for each module.

#### 2.1.1 Level-set Formalism

We first introduce the interface-tracking strategy. Motivated by two-phase-flow applications, we adopt a LS approach, specifically a diffuse-interface variant (Osher & Fedkiw, 2003). This method allows for separation of different regions with a scalar field  $\phi$ , referred to as LS function.

The evolution of this function is governed by the conservative continuity equation popularised by Osher and Sethian (Osher & Sethian, 1988):

$$\frac{\partial \phi}{\partial t} + \vec{\nabla} \cdot (\vec{v}\phi) = 0, \quad (2.1)$$

which transports  $\phi$  under the prescribed velocity field  $\vec{v}$ . Equation (2.1) does not impose any particular shape (e.g. signed-distance property) on  $\phi$ , it solely advances the field in time according to  $\vec{v}$ .

In the classical LS formulation the scalar field  $\phi$  is usually taken to be a signed-distance function (Osher & Fedkiw, 2003): its value is negative in one part of the computational domain and positive in the other, with a prescribed threshold (conventionally 0) separating the two regions. Thus the interface  $\Gamma$  is defined by the zero-level contour

$$\Gamma = \{(x, y) \in \Omega | \phi(x, y) = 0\}. \quad (2.2)$$

where  $\Omega$  denotes the entire computational domain. Representing the interface as an isocontour of a smooth, continuous function rather than as an explicit set of time-dependent boundary points permits the simulation of complex, possibly topology-changing shapes while evolving the system with the single advection equation (2.1) (Osher & Fedkiw, 2003).

Given the freedom to specify the shape of the LS function, we adopt a diffuse-interface variant rather than the classical signed-distance form. This choice, common in phase-field (PF) models, permits the interface to be spread over a finite width instead of being an infinitely sharp contour (Anderson et al., 1998). On a two-dimensional domain the standard LS formulation represents the interface as a one-dimensional zero-level curve, whereas in our diffuse formulation this curve is broadened into a smooth transition zone. For simplicity consider a circular geometry centred at the origin. We model that shape by demanding a value of the field equalling 1 inside and 0 outside, with a continuous smooth function connecting the two. In polar coordinates this can be represented as hyperbolic-tangent profile (Anderson et al., 1998):

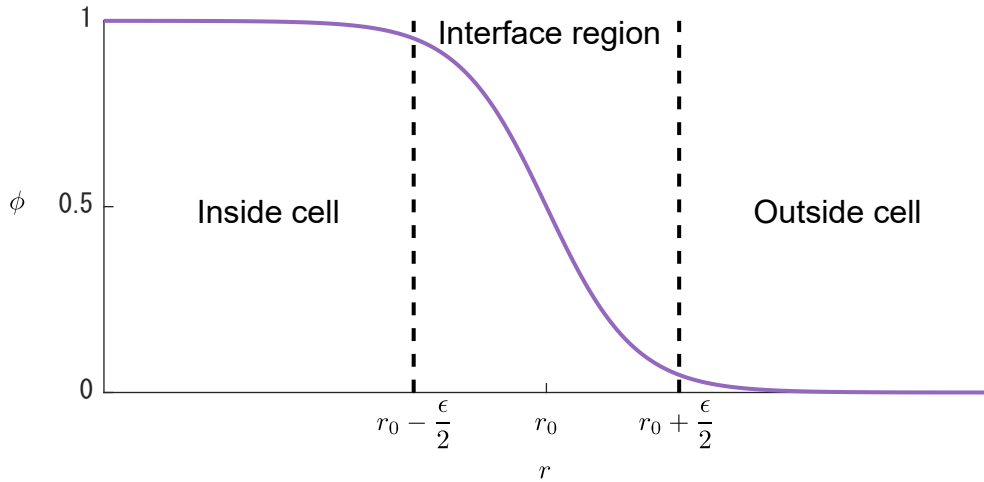
$$\phi(r, \theta) = \frac{1}{2} \left( 1 - \tanh \left( \frac{r - r_0(\theta)}{\varepsilon/3} \right) \right). \quad (2.3)$$

where  $r_0(\theta)$  determines the radial position of the interface and  $\varepsilon$  controls its thickness. The radial profile of  $\phi$  and its gradient are shown in Figure 2.1. In this diffuse setting the interface  $\Gamma$  is identified with the mid-value contour  $\phi = 1/2$ , which coincides with the locus where the

magnitude of the gradient,  $|\nabla\phi|$ , attains its maximum:

$$\Gamma = \{(x, y) \in \Omega | \phi(x, y) = 1/2\}. \quad (2.4)$$

**A**



**B**

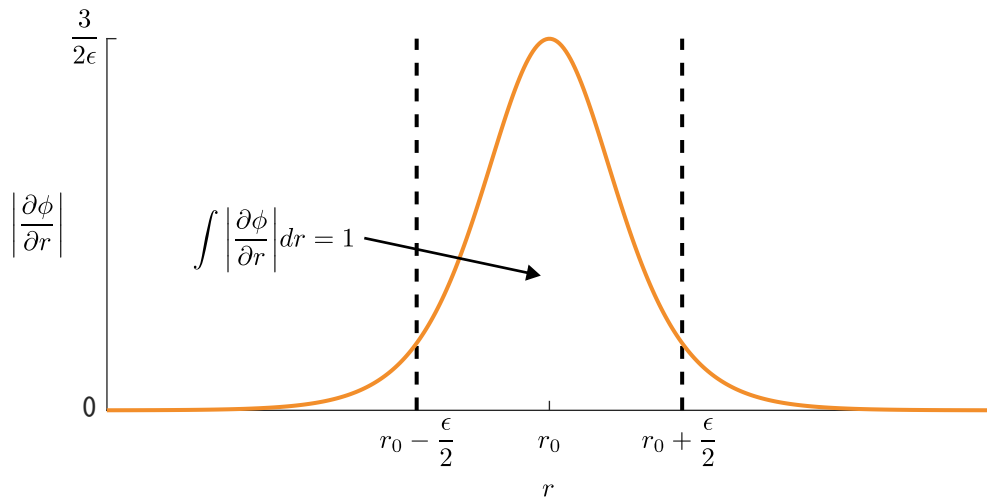


Figure 2.1: **Panel A:** Hyperbolic-tangent level-set function profile across interface region. Region inside cell is characterized by the value of 1 and outside cell by the value of 0. **Panel B:** Magnitude of gradient of the function in panel B in radial direction. Area under the curve equals 1, as annotated.

Employing a hyperbolic-tangent profile offers two key advantages. First, the diffuse profile replaces a discontinuous indicator by a transition layer of width  $\epsilon$ , which alleviates the severe CFL time-step restriction for explicit updates and improves the conditioning of the linear systems arising in implicit updates. Both of the consequences emerge from  $O(1/\epsilon)$ , interfacial gradients present with an infinitely sharp interface. Second, as we are interested in membrane processes,

the normal derivative of  $\phi$  is sharply peaked at the interface (up to normalisation,  $|\vec{\nabla}\phi|$ ) acts as a smooth approximation of the surface Dirac delta supported on  $\{\phi = 1/2\}$  (Peskin, 2002):

$$\frac{\partial\phi(r, \theta)}{\partial r} = \frac{3}{2\varepsilon} \operatorname{sech}^2\left(\frac{3}{\varepsilon}(r - r_0(\theta))\right) = \frac{6}{\varepsilon} \frac{1}{\left(e^{\frac{3}{\varepsilon}(r-r_0(\theta))} + e^{-\frac{3}{\varepsilon}(r-r_0(\theta))}\right)^2} \rightarrow \delta_\varepsilon(r_0(\theta)), \quad (2.5)$$

whose integral over  $r$  equals 1. This property is convenient for localising biochemical processes to the cell cortex, because surface integrals can be recast as volume integrals weighted by  $|\nabla\phi|$  (figure 2.1).

In the diffuse-interface framework geometric quantities, such as the interface curvature, follow directly from derivatives of  $\phi$  (Osher & Fedkiw, 2003). The unit outward normal vector is obtained from the gradient via:

$$\hat{n} = -\frac{\vec{\nabla}\phi}{|\vec{\nabla}\phi|}. \quad (2.6)$$

where the prefactor “−” is required because our convention assigns  $\phi = 1$  to the cell interior and  $\phi = 0$  to the exterior; the raw gradient therefore points inward, and the minus sign reverses its direction. (With this choice the cell area is conveniently given by  $\int_\Omega \phi \, d\Omega$ .) Gradient yields the local curvature  $\kappa$ :

$$\kappa = \vec{\nabla} \cdot \hat{n}, \quad (2.7)$$

which can be evaluated everywhere in the diffuse interface. As the LS gradient, and thus every subsequent function derived from it, is continuous across the domain this can become a problem far from the interface. Usually very high precision of calculation is needed in the regions where  $|\vec{\nabla}\phi| \ll 1$ , to obtain satisfactory approximations of  $\hat{n}$  and  $\kappa$ .

A well-known drawback of the level-set approach is that repeated advection with Eq. (2.1) gradually distorts the prescribed hyperbolic-tangent profile of  $\phi$  (Russo & Smereka, 2000). To restore the desired shape one periodically performs a reinitialisation step, evolving  $\phi$  in a pseudo-time  $\tau$  between physical time steps (for details of this procedure see section 2.2.1). We employ the conservative reinitialisation scheme proposed by Parameswaran and Mandal (Parameswaran & Mandal, 2023):

$$\frac{\partial\phi}{\partial\tau} = (1 - 2\phi) \left( \varepsilon |\vec{\nabla}\phi| - \phi(1 - \phi) \right), \quad (2.8)$$

which drives the bulk values of  $\phi$  towards 0 or 1 while sharpening the transition zone back to the hyperbolic-tangent form (2.3). The method is conservative in the sense that the integral  $\int_\Omega \phi \, d\Omega$ , and hence the cell area, remains constant during the reinitialisation sweep.

The diffuse-interface level-set formulation outlined above provides a straightforward and

robust means of tracking the boundary between two phases on any computational domain. In our framework the scalar field  $\phi$  distinguishes cytoplasm ( $\phi \approx 1$ ) from exterior ( $\phi \approx 0$ ), while the magnitude of its gradient localises the cell cortex. Because  $\phi$  is advected by the fluid velocity, interface motion is naturally coupled to the intracellular flow enabling direct interaction between cell mechanics and the reaction–diffusion system rather than through cell-shape changes alone. This allows for simple integration of the level-set formalism with other component models discussed next.

### 2.1.2 Fluid dynamics

As explained above, the level-set field is advected by the underlying fluid, hence we must supply a velocity field obtained from the governing equations of fluid mechanics. We adopt the incompressible, approximation of the Navier–Stokes equations (Landau & Lifshitz, 1987)<sup>1</sup>:

$$\frac{\partial \vec{v}}{\partial t} = -\frac{1}{\rho} \vec{\nabla} p + \nu \vec{\nabla}^2 \vec{v} + \vec{f}, \quad \vec{\nabla} \cdot \vec{v} = 0. \quad (2.9)$$

where  $\rho$  is density,  $\nu$  represents kinematic viscosity,  $\vec{v}$  the velocity field and  $p$  the pressure. We have neglected nonlinear term, guaranteeing that steady state solution will achieve stokes flow. The vector  $\vec{f}$  refers to the force density profile across the domain.

This force ( $\vec{f}$ ) acting on the fluid is confined to the cell cortex through the smoothed delta-function  $\delta_\epsilon$  (see equation (2.5)) and decomposed as (Brackbill et al., 1992; Whitfield & Hawkins, 2016; Mogilner & Oster, 2003; Barnhart et al., 2011; Fogelson & Keener, 2015):

$$\vec{f} = \left( \sigma \kappa \hat{n} + \vec{\nabla} \sigma - \hat{n} (\hat{n} \cdot \vec{\nabla} \sigma) + k_C C_a \hat{n} - \alpha (A - A_0) \hat{n} \right) \delta(r_0) - \beta \vec{v}. \quad (2.10)$$

The second and third term together represent the surface (tangential) gradient, as  $\hat{n}$  marks the outward unit normal. The surface tension:

$$\sigma = \sigma_0 + k_\sigma C_a, \quad (2.11)$$

increases linearly with the local membrane concentration of the activator species, following Whitfield *et al.* (Whitfield & Hawkins, 2016). The term proportional to  $k_C$ , in equation (2.10), represents the protrusive force generated by actin polymerization at the leading edge (Mogilner & Oster, 1996, 2003), while the penalty term  $\alpha(A - A_0)$  enforces the near-constancy of the projected cell areas observed experimentally (Barnhart et al., 2011). The linear drag term  $-\beta \vec{v}$

<sup>1</sup>For a level-set formulation of two-phase Stokes flow see Ref. (Sussman et al., 1994).

models dissipation and ensures that the flow relaxes when external forcing ceases (Fogelson & Keener, 2015).

Before proceeding, we briefly justify the specific structure of the force density in Eq. (2.10). First, a non-uniform surface tension drives a **Marangoni flow**: fluid motion tangential to the interface from regions of low to high  $\sigma$ , which can strongly bias the otherwise diffusive transport of membrane-bound proteins (Scriven & Sterling, 1960; Sens & Plastino, 2015). Second, making both the surface tension and the protrusive force depend on the local activator concentration directly couples cortical mechanics to the biochemical polarity cue: high activator activity marks the protruding edge of the cell, as discussed in chapter 1 and observed experimentally in live cells (Machacek et al., 2009; Houk et al., 2012). Because leading and trailing edges exhibit different membrane tensions (Houk et al., 2012; Whitfield & Hawkins, 2016), we represent relative changes in  $\sigma$  with the activator-dependent law (2.11) rather than adding further geometric factors. Finally, the actin-generated protrusive force is approximated as acting normal to the cortex, consistent with the mean orientation of filament polymerisation against the membrane (Mogilner & Oster, 2003).

Equations (2.9)–(2.11) thus provide a minimal yet mechanistically grounded route by which the distribution of a polarity protein modulates both cell shape and intracellular/surface flows. In what follows we model this polarity cue as the active, membrane-bound form of the activator, the associated RDA system is described in the next subsection.

### 2.1.3 Reaction–diffusion–advection system

We now turn to the reaction–diffusion–advection (RDA) component of the system, which is coupled to the motility modules described above. The main objective of the RDA model is to capture the dynamics of an activator whose concentration is coupled to the force profiles on the cell cortex and to the substrate from which the activator is produced (Turing, 1952). These coupled species constitute the core of a minimal Turing-type activator–substrate model capable of producing stationary polarity patterns (Bement et al., 2015; Goryachev & Leda, 2019). To extend the available solution space to include time-dependent (Hopf-type) and wave-pinning solutions, we need to introduce at least one additional protein species. Moreover, at least four interacting protein species are required to reproduce all of the above solution types. Including more than four species is unnecessary: it does not enlarge the solution space but does add complexity. As introduced in Section 1.5, because this extra complexity does not yield new protein dynamics, we restrict ourselves to four protein species in the model presented in the remainder of this section.

Guided by this rationale, we define four protein species. Two are cytoplasmic, i.e., restricted to the bulk region, and two are constrained to the cell cortex. One of the membrane species plays the role of the activator  $a$  that couples to the forces. One bulk species acts as the substrate for this activator, we denote its concentration by  $s$ . These two species comprise a minimal Turing-type model. To expand the solution space with wave-pinning-type solutions, we add delayed inhibition. This is achieved by introducing a second membrane species that also catalytically promotes formation of the activator  $a$ . We refer to this membrane species as  $c$ , symbolising a complex formed from the activator and another protein. The partner required to form  $c$  is an inhibitor species restricted to the bulk, which we denote  $in$ .

To summarise, we have introduced four distinct protein species. First, a cortex-bound activator  $a$  that is produced autocatalytically from the bulk substrate  $s$ . The activator  $a$  can then form a membrane-bound complex  $c$  with the bulk-restricted inhibitor  $in$ . Each species diffuses freely-two-dimensionally in the bulk cytoplasm or effectively one-dimensionally along the membrane cortex. All protein-protein reactions are restricted to the overlap between the diffuse-interface region and the bulk (Section 2.1.1). The reactions are written in coarse-grained form, with the abundance of each species represented by a surface or bulk concentration  $C_i(x, y, t)$ , where  $i$  denotes the letter assigned to the specific protein species introduced above. The net reaction terms entering the RDA equations are:

$$R_s = k_3 C_c - C_s \left( 1 - \frac{C_a}{C_a^{\text{MAX}}} \right) (k_1 + k_{11} C_a + k_{12} C_c), \quad (2.12a)$$

$$R_{in} = k_3 C_c - k_2 C_a C_{in}, \quad (2.12b)$$

$$R_a = -k_2 C_a C_{in} + C_s \left( 1 - \frac{C_a}{C_a^{\text{MAX}}} \right) (k_1 + k_{11} C_a + k_{12} C_c), \quad (2.12c)$$

$$R_c = k_2 C_a C_{in} - k_3 C_c. \quad (2.12d)$$

Here  $k_1$  is the basal rate at which cytosolic substrate  $s$  binds and activates on the membrane.  $k_{11}$  and  $k_{12}$  quantify co-operative autocatalysis mediated, respectively, by membrane activator  $a$  and by the transient complex  $c$ . The positive feedback provided by  $k_{11}$  supplies the classical activator self-activation mechanism of Turing-type systems (Turing, 1952; Goryachev & Leda, 2019). The additional, delayed feedback through  $k_{12}$  (activator  $a$  that is momentarily inactive within the complex  $c$  still promotes further activator  $a$  recruitment) has been shown to broaden the parameter range that supports pattern formation in mass-conserved models (Otsuji et al., 2007; Mori et al., 2008). Complex formation and dissociation are governed by  $k_2$  and  $k_3$ , respectively. Finally, the factor  $(1 - C_a/C_a^{\text{MAX}})$  prevents activator  $a$  from exceeding a steric saturation limit

on the membrane (Douglass & Vale, 2005; Mori et al., 2008).

To complete the description of our RDA module, we now write the full reaction–diffusion equations. The model includes diffusion both in the cytoplasm and along the membrane. Consistent with single-particle tracking and FRAP measurements, membrane diffusion coefficients are typically two orders of magnitude smaller than their cytosolic counterparts (Cowan et al., 1997; Halatek et al., 2018). Earlier theoretical work demonstrated that the absolute and relative values of these coefficients strongly influence pattern selection in mass-conserved systems: in particular, the ratio of *in* (or complex *c*, as discussed in Section 2.3.2) to activator *a* controls the range of stationary and wave-pinned solutions (Šoštar, 2022; Mori et al., 2008). In addition to diffusion, we advect all species with the fluid velocity field obtained from the Navier-Stokes module, a coupling we found essential for reproducing realistic motility phenotypes (see Chapter 4).

Thus, the evolution of any species  $C_i$  (bulk or membrane) is written in conservative form as:

$$\frac{\partial C_i}{\partial t} + \vec{\nabla} \cdot (\vec{v} C_i) = \vec{\nabla} \cdot (D_i \vec{\nabla} C_i) - \vec{\nabla} \cdot \left( \frac{D_i}{k_B T} \vec{F}_i C_i \right) + R_i. \quad (2.13)$$

with  $i$  denoting the above defined protein species. In equation (2.13),  $k_B$  is Boltzmann’s constant and  $T$  is the absolute temperature. The advection term  $\vec{\nabla} \cdot (\vec{v} C_i)$  transports each species with the fluid velocity obtained from the Navier-Stokes module. The first term on the right-hand side represents Fickian diffusion with coefficient  $D_i$ . Next,  $R_i$  collects the reaction rates given in Eqs. (2.12). The middle term,  $\vec{\nabla} \cdot (D_i/k_B T \vec{F}_i C_i)$ , is a drift flux that confines each species to its appropriate compartment. We realise  $\vec{F}_i$  as the gradient of a short-range potential. The confining-force approach is preferred over pointwise Dirichlet constraints because it preserves strict mass conservation of each species while remaining compatible with the diffuse-interface formulation of Section 2.1.1.

The construction of the potential is motivated by the assumption that, in a homogeneous steady state, the probability of finding a cytosolic protein is proportional to the level-set field  $\phi$ , whereas for a membrane-bound protein it is proportional to the smoothed delta function  $|\nabla\phi|$  introduced in Eq. (2.5). If these probabilities obey Boltzmann statistics, we can write:

$$p_{\text{Bulk}} \propto e^{-U_{\text{Bulk}}/k_B T} \propto \phi, \quad (2.14a)$$

$$p_{\text{Surface}} \propto e^{-U_{\text{Surface}}/k_B T} \propto |\vec{\nabla}\phi| \rightarrow \delta(r_0). \quad (2.14b)$$

By rearranging these equations, we explicitly obtain expressions for the localisation potentials:

$$U_{\text{Bulk}} = -k_B T \ln(\phi), \quad (2.15a)$$

$$U_{\text{Surface}} = -k_B T \ln\left(|\vec{\nabla}\phi| \frac{2\epsilon}{3}\right). \quad (2.15b)$$

The force appearing in Eq. (2.13) is  $\vec{F}_i = -\nabla U_i$ ; the factors  $k_B T$  cancel between Eqs. (2.13) and (2.12), so the drift term depends only on  $D_i$  and on  $\phi$  (or  $|\nabla\phi|$  for surface species). Reactions

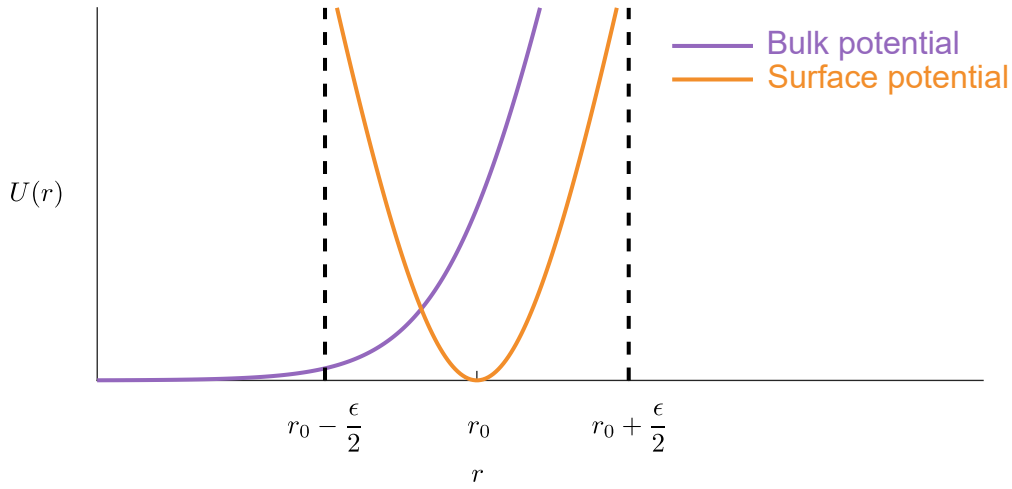


Figure 2.2: Bulk (blue) and surface (red) localisation potentials. Their overlap (purple) defines a thin region in which cytosolic and membrane species coexist and can react. Because  $k_B T$  cancels in Eq. (2.13), the potential amplitude scales with the diffusion coefficient  $D_i$ , which sets the vertical axis.

between cytosolic and membrane species are therefore confined to the finite overlap zone of the two potentials (Fig. 2.2). The effective reaction rate at a given point on the interface is obtained by integrating the local kinetics over this region along the normal direction, a procedure analogous to the surface–volume coupling used in diffuse-interface models of membrane biochemistry.

Thus, we combine a diffuse-interface level-set framework for tracking the cell cortex with an incompressible, Navier–Stokes description of cytoplasmic flow. Cell motion arises self-consistently from normal forces generated by actin polymerisation, modelled by protrusive coupling ( $k_C$  in (2.10)), and from Marangoni stresses produced by spatial variations in membrane surface tension. This mechanical module is tightly coupled to an RDA system that accounts for cycling of the activator  $a$  and its substrates and regulators, reproducing the spatio-temporal patterns observed in live cells (Das et al., 2012; Graessl et al., 2017; Michaux et al., 2018; Šoštar et al., 2024). The next section details the numerical schemes used to solve these coupled

equations.

## 2.2 Numerical Methods

In this section we detail the numerical implementation of the model presented in previous section 2.1. We present a mathematical description of the domain, the spatial and temporal discretizations, and the algorithms used to solve the model equations. After introducing these numerical details, we discuss stability, computer implementation, and finally the supplementary MATLAB (The MathWorks, Inc., 2023) routines for analysing the simulation results. Our aim is to keep the implementation procedure simple and straightforward by using a central finite-difference approximation on a periodic Cartesian domain together with forward-Euler time integration. To enable efficient simulation of the discretized model, the governing equations were implemented in the C programming language (International Organization for Standardization (ISO) & International Electrotechnical Commission (IEC), 2024), which keeps execution times short while offering low-level control.

### 2.2.1 Implementation of the model equations

To numerically solve the system of equations describing the model, we first discretize the computational domain, impose suitable boundary conditions, and approximate the spatial derivatives of the velocity, LS function, and concentration fields. Once these approximations are in place, the equations are advanced in time. As mentioned earlier, we adopt a straightforward procedure, the details of which can be found in standard textbooks (LeVeque, 2007; Morton & Mayers, 2005; Press et al., 2007). We end this section by presenting parameters used in our simulations as well as classifying the numerical performance of the simulations.

#### Simulation grid

The two-dimensional computational domain is a uniform Cartesian lattice,  $[0, L_x] \times [0, L_y]$ , in our simulations we always take  $\Delta x = \Delta y$ . It is partitioned into  $I - 1$  cells in the  $x$ -direction and  $J - 1$  cells in the  $y$ -direction. Periodic boundary conditions are applied on all sides (Fig. 2.3), so that the mesh is topologically equivalent to the surface of a torus. Operationally, the last column of nodal values is set equal to the first column and, analogously, the last row is set equal to the first; consequently, the four corner nodes represent the same physical point. We adopt a staggered marker-and-cell (MAC) arrangement (Harlow & Welch, 1965), in which scalar quantities (pressure, level-set, concentration, *etc.*) are defined at cell centres, whereas velocity

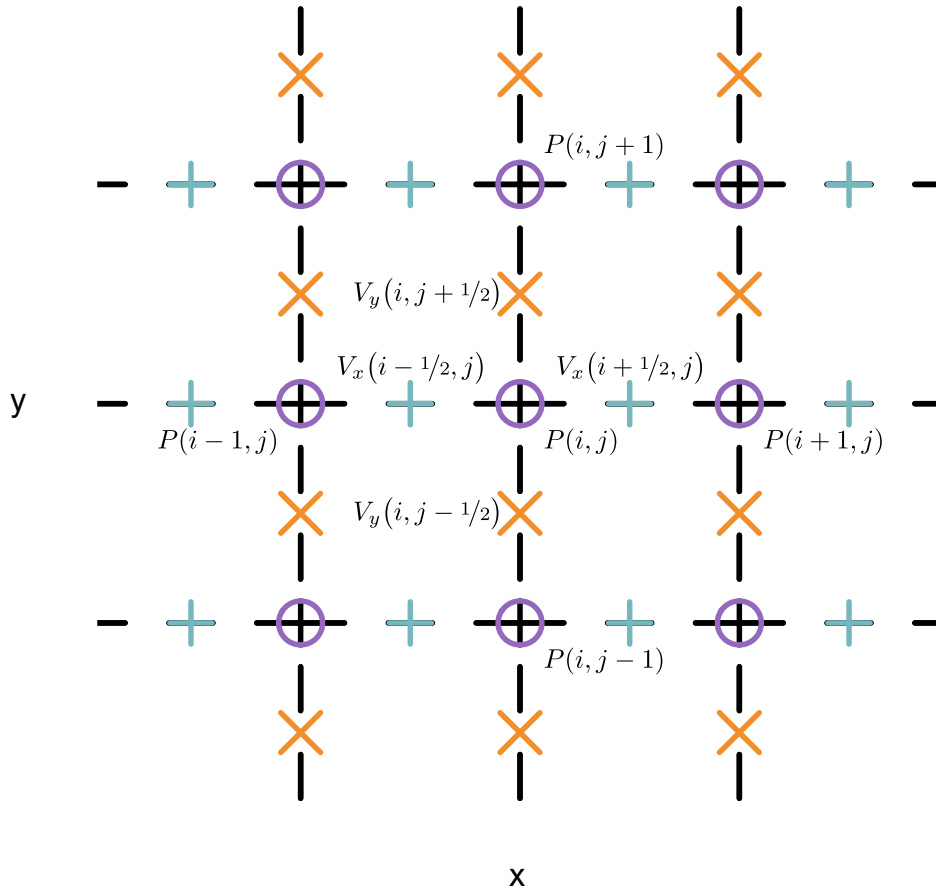


Figure 2.3: Schematic of MAC grid with indicated shifted points at which velocities  $V_x$  and  $V_y$  are defined. Purple  $\circ$  represent main grid points indexed with  $i$  and  $j$ , Orange  $\times$  represent face points at which velocity  $V_x$  is defined and teal  $+$  represent face points at which velocity  $V_y$  is defined.

components are stored on the corresponding cell faces (see Fig. 2.3). This staggered layout suppresses spurious chequerboard modes in the pressure field and yields second-order-accurate pressure gradients (Harlow & Welch, 1965).

### Spatial discretization

To discretize the model fields on the domain defined above, we employ a second-order central-finite-difference (CFD) scheme. This choice offers a good compromise between implementation simplicity and accuracy (LeVeque, 2007). Three differential operators appear in the governing equations: divergence ( $\vec{\nabla} \cdot$ ), gradient ( $\vec{\nabla}$ ), and the Laplacian ( $\nabla^2$ ), each involving first- or second-order derivatives. Throughout this section we adopt the following notation:

- **Cell-centred scalars and vectors:**  $H(i, j)$  and  $\vec{H}(i, j)$  with Cartesian components  $H_x(i, j)$  and  $H_y(i, j)$ .
- **Face-centred vectors:**  $\vec{G}$  with components  $G_x(i + 1/2, j)$  and  $G_y(i, j + 1/2)$ .

Here  $i \in [1, \dots, I]$  and  $j \in [1, \dots, J]$  index columns and rows, respectively. Depending on the variable being differentiated and the equation being discretized, several stencils are required; below we list those actually used. Coefficients and derivations can be found in textbooks about finite-difference methods (LeVeque, 2007; Fornberg, 1988)

**Face-to-cell interpolation and derivatives.** In the MAC layout the incompressible Navier-Stokes equations (2.9) are solved on cell faces, whereas pressure  $p$  and body force  $\vec{f}$  reside at cell centres. Likewise, the level-set (2.1) and reaction-diffusion-advection equation (2.13) require velocities interpolated to cell centres. For a face-centred vector  $\vec{G}$ :

$$G_x(i, j) = \frac{G_x(i + 1/2, j) + G_x(i - 1/2, j)}{2}, \quad (2.16)$$

$$G_y(i, j) = \frac{G_y(i, j + 1/2) + G_y(i, j - 1/2)}{2}. \quad (2.17)$$

First-order derivatives at the same cell centres follow as

$$\frac{\partial G}{\partial x}(i, j) \approx \frac{G_x(i + 1/2, j) - G_x(i - 1/2, j)}{\Delta x}, \quad (2.18)$$

$$\frac{\partial G}{\partial y}(i, j) \approx \frac{G_y(i, j + 1/2) - G_y(i, j - 1/2)}{\Delta y}, \quad (2.19)$$

$$\vec{\nabla} \cdot \vec{G}(i, j) = \frac{\partial G}{\partial x}(i, j) + \frac{\partial G}{\partial y}(i, j). \quad (2.20)$$

**Cell-to-face interpolation and derivatives.** For a cell-centred scalar  $H$ :

$$H(i + 1/2, j) = \frac{H(i + 1, j) + H(i, j)}{2}, \quad (2.21)$$

$$H(i, j + 1/2) = \frac{H(i, j + 1) + H(i, j)}{2}, \quad (2.22)$$

$$\frac{\partial H}{\partial x}(i + 1/2, j) \approx \frac{H(i + 1, j) - H(i, j)}{\Delta x}, \quad (2.23)$$

$$\frac{\partial H}{\partial y}(i, j + 1/2) \approx \frac{H(i, j + 1) - H(i, j)}{\Delta y}. \quad (2.24)$$

Second derivatives needed in (2.9) are evaluated on faces as:

$$\frac{\partial^2 G_x}{\partial x^2}(i+1/2, j) = \frac{G_x(i-1/2, j) - 2G_x(i+1/2, j) + G_x(i+3/2, j)}{\Delta x^2}, \quad (2.25)$$

$$\frac{\partial^2 G_y}{\partial y^2}(i, j+1/2) = \frac{G_y(i, j-1/2) - 2G_y(i, j+1/2) + G_y(i, j+3/2)}{\Delta y^2}. \quad (2.26)$$

**Cell-centred operators.** At cell centres the gradient and divergence use the standard symmetric second-order stencil:

$$\frac{\partial H}{\partial x}(i, j) \approx \frac{H(i+1, j) - H(i-1, j)}{2\Delta x}, \quad (2.27)$$

$$\frac{\partial H}{\partial y}(i, j) \approx \frac{H(i, j+1) - H(i, j-1)}{2\Delta y}, \quad (2.28)$$

$$\vec{\nabla} \cdot \vec{H}(i, j) = \frac{\partial H_x}{\partial x}(i, j) + \frac{\partial H_y}{\partial y}(i, j), \quad (2.29)$$

$$\vec{\nabla} H(i, j) = \frac{\partial H}{\partial x}(i, j) \hat{x} + \frac{\partial H}{\partial y}(i, j) \hat{y}. \quad (2.30)$$

**Laplacian at cell centres.** Two alternative Laplacian stencils are used:

(a) *Four-point, two-step stencil* (accurate for conservative balances):

$$\begin{aligned} {}_1\nabla^2 H(i, j) &= \frac{\partial^2 H}{\partial x^2}(i, j) + \frac{\partial^2 H}{\partial y^2}(i, j) \\ &\approx \frac{H(i-2, j) - 2H(i, j) + H(i+2, j)}{4\Delta x^2} + \\ &\quad + \frac{H(i, j-2) - 2H(i, j) + H(i, j+2)}{4\Delta y^2}. \end{aligned} \quad (2.31)$$

(b) *Nine-point isotropic stencil*:

$$\begin{aligned} {}_2\nabla^2 H(i, j) &\approx K_D [H(i-1, j-1) + H(i-1, j+1) + H(i+1, j-1) + H(i+1, j+1)] \\ &\quad + K_O [H(i-1, j) + H(i+1, j) + H(i, j+1) + H(i, j-1)] + K_C H(i, j), \\ K_D &= \frac{\gamma}{2\Delta x \Delta y}, \quad K_O = \frac{1-\gamma}{\Delta x \Delta y}, \quad K_C = \frac{2\gamma-4}{\Delta x \Delta y}, \end{aligned} \quad (2.32)$$

where  $\gamma = \frac{1}{3}$  gives a rotationally invariant stencil (Patra & Karttunen, 2006), while  $\gamma = \frac{1}{2}$

yields the most isotropic variant (Oono & Puri, 1987, 1988). We adopt the latter throughout.

### Temporal integration and stability conditions

To advance Eqs. (2.1), (2.9), and (2.13) in time we employ the explicit forward-Euler scheme (LeVeque, 2007; Butcher, 2016), which is first-order accurate:

$$H(i, j)^{t+\Delta t} \approx H(i, j)^t + \frac{dH^t}{dt}(i, j) \Delta t, \quad (2.33)$$

$$G_x(i + 1/2, j)^{t+\Delta t} \approx G_x(i + 1/2, j)^t + \frac{dG_x^t}{dt}(i + 1/2, j) \Delta t, \quad (2.34)$$

$$G_y(i, j + 1/2)^{t+\Delta t} \approx G_y(i, j + 1/2)^t + \frac{dG_y^t}{dt}(i, j + 1/2) \Delta t. \quad (2.35)$$

When combined with the second-order central-difference spatial discretization, forward Euler renders the pure advection terms *linearly unstable*; numerical errors grow exponentially, manifesting as high-frequency oscillations in the level-set and concentration fields (see (LeVeque, 2007) chapter 10.3). The explicit diffusion and reaction operators, however, contribute negative real parts to the eigenvalues, so a global stability bound can still be derived by von Neumann analysis:

$$\Delta t \leq \min\left(\frac{h^2}{4D_{\max}}, \frac{h^2}{4\nu}, \frac{1}{k_{\max}}\right), \quad (2.36)$$

where  $h = \min(\Delta x, \Delta y)$  is the smaller grid spacing,  $\nu$  is the kinematic viscosity, and  $D_{\max}$  and  $k_{\max}$  are the largest diffusion coefficient and reaction rate, respectively, in the RDA subsystem. Within the parameter ranges explored, the bound is dominated by the bulk substrate diffusivity  $D_s$ . A practical assessment of stability is provided in Subsection 2.2.1.

### Incompressible Stokes-pressure algorithm

When solving the Navier-Stokes system (2.9) the velocity field must remain divergence-free. A standard remedy is to solve a Poisson equation for the pressure that enforces this constraint (Harlow & Welch, 1965; Chorin, 1968). Taking the divergence of the time-discretised momentum equation yields:

$$\frac{\vec{\nabla} \cdot \vec{V}^{t+\Delta t} - \vec{\nabla} \cdot \vec{V}^t}{\Delta t} = -\frac{1}{\rho} \nabla^2 p^{t+\Delta t} + \nu \nabla^2 (\vec{\nabla} \cdot \vec{V}^t) + \vec{\nabla} \cdot \vec{f}^t, \quad (2.37)$$

where  $\rho$  is the fluid density and  $\nu$  the kinematic viscosity. By imposing the incompressibility condition  $\vec{\nabla} \cdot \vec{V}^{t+\Delta t} = 0$  we arrive at the Poisson problem:

$$\nabla^2 p^{t+\Delta t}(i, j) = \rho \vec{\nabla} \cdot \vec{f}^t(i, j) + \rho \nu \nabla^2 (\vec{\nabla} \cdot \vec{V}^t)(i, j) + \frac{\rho}{\Delta t} (\vec{\nabla} \cdot \vec{V}^t)(i, j) = Z(i, j). \quad (2.38)$$

Thus any divergence introduced at step  $t$  is projected out in the pressure update at  $t + \Delta t$ .

We solve (2.38) with a classic Jacobi iteration (Young, 1954; Saad, 2003). On a uniform grid ( $\Delta x = \Delta y = h$ ) the five-point stencil reads  $\nabla^2 p = (p_{i+1,j} + p_{i-1,j} + p_{i,j+1} + p_{i,j-1} - 4p_{i,j})/h^2$ . Re-arranging for  $p_{i,j}$  gives the Jacobi update:

$$p^{(k+1)}(i, j) = \frac{1}{4} [p^{(k)}(i+1, j) + p^{(k)}(i-1, j) + p^{(k)}(i, j+1) + p^{(k)}(i, j-1) - h^2 Z(i, j)], \quad (2.39)$$

where the superscript  $(k)$  denotes the iteration count. Iteration proceeds until either a prescribed maximum number of sweeps is reached or the root-mean-square change between successive iterates falls below a specified tolerance ( $p_{\text{TOL}}$  in parameters table 2.1). Finally, the pressure is normalised by subtracting its spatial mean so that  $\langle p \rangle = 0$ .

### Level-set re-initialisation algorithm

As introduced in Section 2.1.1, the level-set field  $\phi$  must be systematically re-initialised so that it retains the desired hyperbolic-tangent profile. Re-initialisation is performed by marching the auxiliary Eq. (2.8) in a pseudo-time  $\tau$ . A convenient way to measure the deviation from the target profile is:

$$|\vec{\nabla} \phi| = \frac{\phi}{\varepsilon} (1 - \phi), \quad (2.40)$$

which follows directly by taking the radial derivative of Eq. (2.3). At the start of every physical time step we test, for all grid nodes  $(i, j)$ ,

$$\left| \varepsilon |\vec{\nabla} \phi|(i, j) - \phi(i, j) [1 - \phi(i, j)] \right| < 1s_{\text{TOL}}, \quad |\vec{\nabla} \phi|(i, j) = \sqrt{(\partial_x \phi)^2 + (\partial_y \phi)^2}, \quad (2.41)$$

where  $1s_{\text{TOL}}$  is a user-defined tolerance and the discrete derivatives  $\partial_x \phi, \partial_y \phi$  are evaluated with Eqs. (2.27)–(2.28). If the condition (2.41) is violated at any point  $(i, j)$ , we advance the re-initialisation equation (2.8) forward by one pseudo-time step  $\Delta \tau$  and retest. The loop terminates once the condition is true everywhere. In practice we find that choosing<sup>2</sup>  $\Delta \tau \approx 100 \Delta t$  allows the procedure to converge within one or two pseudo-time iterations, and that re-initialising once every  $\sim 10$  physical steps is sufficient for the parameter ranges considered.

<sup>2</sup>See also the discussion in (Parameswaran & Mandal, 2023).

### Simulation workflow

Figure 2.4 sketches the logical flow of one simulation step, summarised here for clarity:

1. **Level-set check and (optional) re-initialisation** (Subsection 2.2.1) Test condition (2.41); if violated at any node, advance the re-initialisation equation (2.8) in pseudo-time.
2. **Auxiliary-field update** (Subsection 2.2.1)
  - Compute  $\vec{\nabla}\phi$ ,  $\nabla^2\phi$ , curvature  $\kappa$ , interface normals  $\hat{n}$ , and cell-centred velocity  $\vec{V}(i, j)$ .
  - Evaluate divergence, gradient, and Laplacian operators required by the governing equations on the appropriate grids.
3. **Gradient cut-off filter** (Subsection 2.2.1) If  $|\vec{\nabla}\phi|(i, j) < g_{CO}$  at a node, set  $\vec{\nabla}\phi$ ,  $\kappa$ , and  $\hat{n}$  to zero there. The threshold  $g_{CO}$  is tuned so that numerical noise remains bounded over the time scales of interest.
4. **Computation of body force** (Section 2.1.2) Assemble the body-force density  $\vec{f}$  from membrane tension, active stresses, and localisation potentials.
5. **Pressure projection** (Subsection 2.2.1) Solve the Poisson problem (2.38) by Jacobi iteration, terminating when either the root-mean-square update falls below  $p_{TOL}$  or a maximum of  $maxIter$  sweeps is reached. Subtract the domain-average pressure to fix the gauge.
6. **Localisation potentials and surface–bulk coupling** (Section 2.1.3) Evaluate the surface- and bulk-potential fields; if  $|\phi| < g_{CO}$  or  $|\vec{\nabla}\phi| < g_{CO}$  at a node, clamp the potential to its far-field value to avoid division by small numbers.
7. **Time integration of all fields** (Subsection 2.2.1) Advance  $\vec{V}$ ,  $\phi$ , and the concentrations  $C_s, C_a, C_{in}, C_c$  by one physical time step  $\Delta t$  using the forward-Euler update (2.33)–(2.35).

### Practical remarks.

- Initialization: All fields are initialised from user-prescribed profiles.
- Output: At user-defined intervals we record snapshots of  $\phi$ ,  $\vec{V}$ , and the concentration fields. These data are post-processed by the MATLAB scripts described in Section 2.2.3.
- Performance: For grids up to  $256^2$  (which correspond to the grids used in most of our simulations) a plain Jacobi solver suffices.

### Model parameters

Table 2.1 lists the parameters and default value ranges used in our simulations. The exact physical values, can be calculated by assuming  $1 \mu\text{m}$ ,  $1 \text{s}$ , and  $100 \text{pN}$  as units of length, time, and force, respectively, using units provided in the third column of the Table 2.1. Diffusion coefficients, reaction rates, and coupling constants were tuned to obtain sustained Hopf-type oscillations in

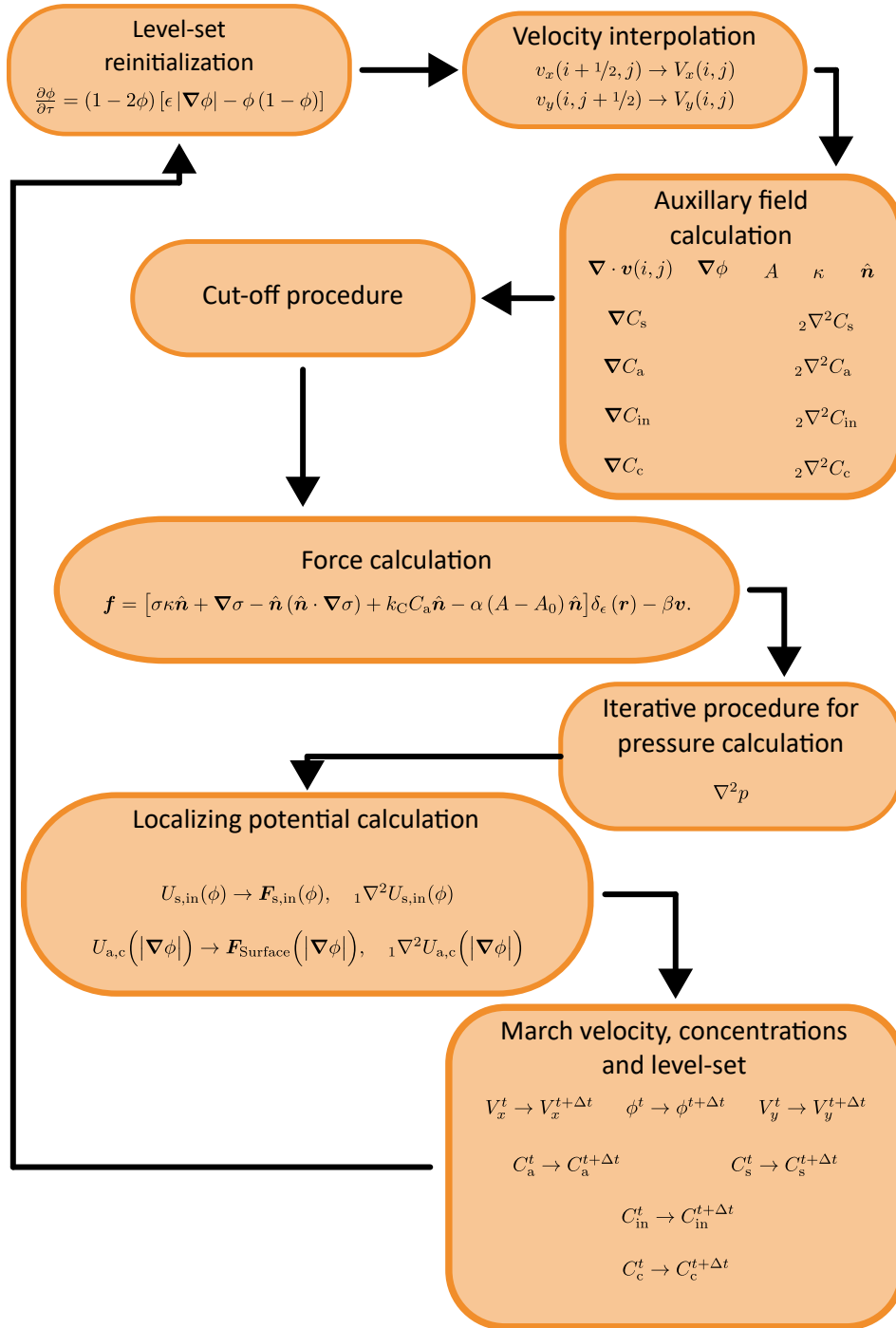


Figure 2.4: Schematic representation of the simulation work flow.

the reaction–diffusion–advection (RDA) module, while the mechanical parameters were selected to yield realistic cell morphodynamics without introducing numerical stiffness.

The diffusion coefficients and reaction constants values were adopted from previous works Ivšić, 2019; Šoštar et al., 2024. In this earlier research, the signalling network of *Dictyostelium discoideum* was reduced to only four reaction species, recovering the experimentally-observed patterns on stationary cells. Finally, some of the parameters, listed in the Table 2.1, are introduced by our numerical algorithm and have no physical meaning. For them, we have again used the trial and error method, making sure that the stability conditions of our numerical routines are satisfied. This includes the density  $\rho$  in our simulations, which was artificially upscaled to increase the time step of the simulation, while keeping the overall dynamics overdamped.

#### Rationale for parameter choices:

- **Domain and grid spacing:** The domain is at least twice the initial-cell diameter for motility simulations, ensuring that periodic images do not interact. A grid spacing of  $\Delta x = \Delta y = \epsilon/10$  resolves the diffuse interface with ten nodes across its thickness, which is sufficient for second-order accuracy (Tryggvason et al., 2011).
- **Time step:** The forward-Euler step obeys Eq. (2.36). We adopt a safety factor of 2 to account for the additional advection instability (see Subsections 2.2.1 and 2.2.1).
- **Thresholds:** The gradient ( $g_{\text{TOL}}$ ), level-set ( $l_{\text{sTOL}}$ ), and pressure ( $p_{\text{TOL}}$ ) tolerances were obtained by systematic grid-refinement tests. The reported values keep spurious oscillations below 1 % of the signal.
- **Fluid properties:** Viscosity  $\nu$  and density  $\rho$  are set to unity in nondimensional units.
- **Mechanical couplings:** The ranges for  $k_{\sigma}$  and  $k_C$  allow the surface tension to vary between 0 and  $2\sigma_0$ , spanning typical values reported for migrating *Dictyostelium* cells (Merkel et al., 2000).
- **RDA parameters:** Diffusion coefficients follow the single-cell FRAP measurements of Rac1 and GAP in Ref. (Machacek et al., 2009); reaction rates are chosen so that the well-mixed system exhibits a supercritical Hopf bifurcation, consistent with protrusion-retraction cycles.

#### Numerical stability

Over the time scales studied we did not observe spurious high-frequency oscillations in the level-set field  $\phi$  or in the concentration profiles. Re-initialisation (Subsection 2.2.1) and molecular diffusion appear to damp the forward-Euler/central-difference advection errors effectively. A second, more subtle source of error stems from the anisotropy of the second-order central-

Table 2.1: Parameters used in the simulations

Parameter	Symbol	Range / Value	Unit
Domain size	$L_x, L_y$	15–30	$\mu\text{m}$
Grid spacing	$\Delta x, \Delta y$	0.12	$\mu\text{m}$
Time step	$\Delta t$	$5 \times 10^{-5}$	s
Gradient threshold	gCO	$1 \times 10^{-3}$	—
Level-set tolerance	lsTOL	$1 \times 10^{-3}$	—
Pressure tolerance	pTOL	$1 \times 10^{-5}$	—
Maximum Jacobi iterations	maxIter	$6 \times 10^4$	—
Interface thickness	$\varepsilon$	1.2	$\mu\text{m}$
Viscosity (dynamic)	$\nu$	1	150 Pa s
Density	$\rho$	1	-
Resting surface tension	$\sigma_0$	4–5	$0.5 \text{ nN } \mu\text{m}^{-1}$
Surface-tension coupling	$k_\sigma$	-0.06–0.06	$100 \text{ pN } \mu\text{m}^2$
Protrusive-force coupling	$k_C$	0–0.06	$100 \text{ pN } \mu\text{m}$
Dissipation coefficient	$\beta$	1	$100 \text{ pN s } \mu\text{m}^{-4}$
Area-constraint coefficient	$\alpha$	0.1	$10 \text{ pN } \mu\text{m}^{-4}$
Initial cell area	$A_0$	120	$\mu\text{m}^2$
Initial cell radius	$r_0 (= \sqrt{A_0/\pi})$	6.21	$\mu\text{m}$
<b>Diffusion coefficients</b>			
substrate 1	$D_s$	34	$\mu\text{m}^2 \text{ s}^{-1}$
activator	$D_a$	0.001–1	$\mu\text{m}^2 \text{ s}^{-1}$
inhibitor	$D_{in}$	8	$\mu\text{m}^2 \text{ s}^{-1}$
complex	$D_c$	0.001–1	$\mu\text{m}^2 \text{ s}^{-1}$
<b>Reaction rates</b>			
activator attachment	$k_1$	0.19	$\text{s}^{-1}$
activator autocatalytic attachment	$k_{11}$	0.027	$\mu\text{m}^3 \text{ s}^{-1}$
Catalytic complex attachment	$k_{12}$	0.0045	$\mu\text{m}^3 \text{ s}^{-1}$
complex assoc.	$k_2$	4.5	$\mu\text{m}^3 \text{ s}^{-1}$
complex dissoc.	$k_3$	0.15	$\text{s}^{-1}$
Activator saturation conc.	$C_a^{\text{max}}$	200	$\mu\text{m}^{-3}$
Total species 1 molecules ( $a + s + c$ )	$N_1$	2000–4000	—
Total species 1 molecules ( $in + c$ )	$N_2$	500–1500	—

difference (CFD) gradient operator: numerical curvature and normal-vector estimates are slightly larger on the grid diagonals than along the cardinal directions. To quantify the resulting shape error we ran four otherwise identical simulations, varying only the gradient cut-off threshold gCO (see Subsection 2.2.1, step 3).

Each run starts from a circular interface of radius  $r_0 = 6.21$  on a  $L_x = L_y = 28$  domain with

periodic boundaries. Surface-tension coupling and protrusive forces are disabled ( $\sigma_0 = 5$ ,  $k_\sigma = k_C = 0$ ). Two physical regimes are considered:

- (i) stationary cell without damping ( $\beta = 0$ );
- (ii) translating cell without damping ( $\beta = 0$ ), initialised with  $\vec{V} = 0.1 \hat{x}$  everywhere.

All other parameters follow Table 2.1; thus the only intended dynamics are rigid translation or stationarity.

At every output time we extract the  $\phi = 0.5$  contour, interpolate its radius onto  $N = 100$  equally spaced polar angles, and compute the relative radial error:

$$\text{Error}(t) = \sqrt{\frac{1}{N} \sum_{i=1}^N \left[ \frac{R(t, i) - R_0(i)}{R_0(i)} \right]^2}, \quad (2.42)$$

where  $R(t, i)$  is the distance from the contour centroid and  $R_0(i)$  is the initial value. Domain-averaged momentum and kinetic energy are monitored via:

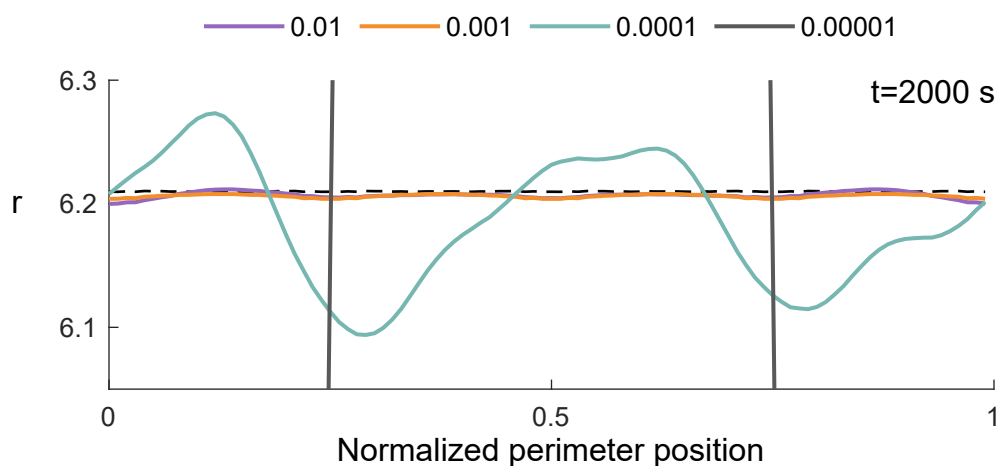
$$\bar{\vec{p}}(t) = \frac{\rho \Delta x \Delta y}{(I-1)(J-1)} \sum_{i=1}^{I-1} \sum_{j=1}^{J-1} [V_x(i, j, t) \hat{x} + V_y(i, j, t) \hat{y}], \quad (2.43)$$

$$\bar{E}_k(t) = \frac{\rho \Delta x \Delta y}{2(I-1)(J-1)} \sum_{i=1}^{I-1} \sum_{j=1}^{J-1} [V_x^2(i, j, t) + V_y^2(i, j, t)]. \quad (2.44)$$

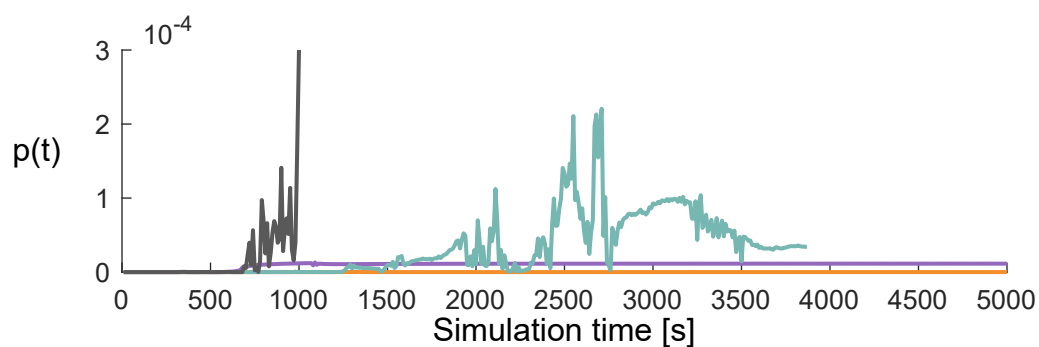
Metrics for stationary cell (i) are presented on figure 2.5, while for cell translating with the constant velocity (ii) we present metrics on figure 2.6. We can see that for stationary cell, first three (largest) cut-off values produce negligible deformation of the cell contour after 2000 s of simulation time. For the smallest cut-off value ( $g_{CO} = 0.00001$ ) the deformation of the contour is too large to fit on the presented plot and only two almost vertical lines are visible, where contour crosses the initial radius value. We remind that all of the conclusions made later in the thesis are made after 1500 s. Furthermore, if we focus on average momentum magnitude and kinetic energy associated with the grid point (panels B and C) we can observe that for the two smallest cut-off values presented ( $g_{CO} = 0.01$  and  $g_{CO} = 0.001$ ) both momentum and kinetic energy remain negligible during whole simulation time of 5000 s of simulation. Moreover, the momentum magnitude for cut-off  $g_{CO} = 0.001$  is smaller than for  $g_{CO} = 0.01$ . This was the rationale for choosing the former value for all of our simulations.

Moving on to the cell translating with constant velocity (ii), the deformations of the contour presented on figure 2.6 A, all show degradation of the initial contour. The two largest cut-off values who almost the same error while smaller cut-offs show more pronounced deformation. Shifting our focus to average momentum magnitude and kinetic energy we can again see how

A



B



C

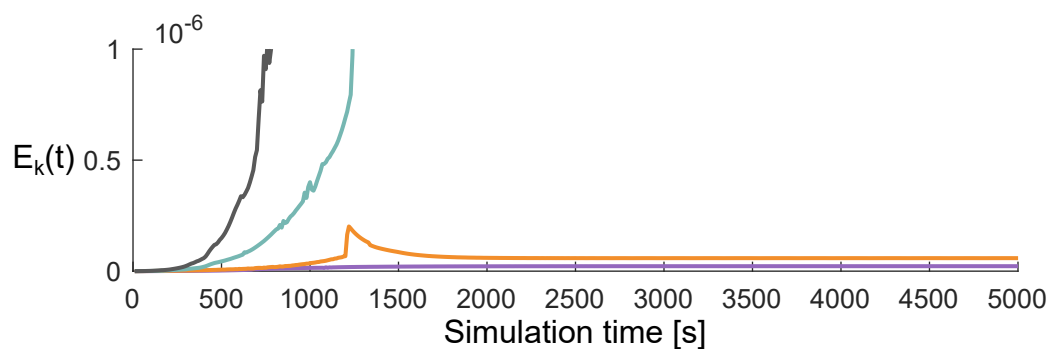


Figure 2.5: Radius error, average momentum and kinetic energy associated with the point on the mesh for stationary cell (i). **Panel A:** Radius profile after  $t = 2000$  s of simulation time. Line colors correspond to the different values of the cutoff  $g_{CO}$ . Black dashed line represents starting radius. **Panel B:** Average momentum magnitude associated with the grid point versus simulation time. Colours correspond to the legend in panel A. **Panel C:** Kinetic energy associated with the grid point versus simulation time. Colours correspond to the legend in panel A.

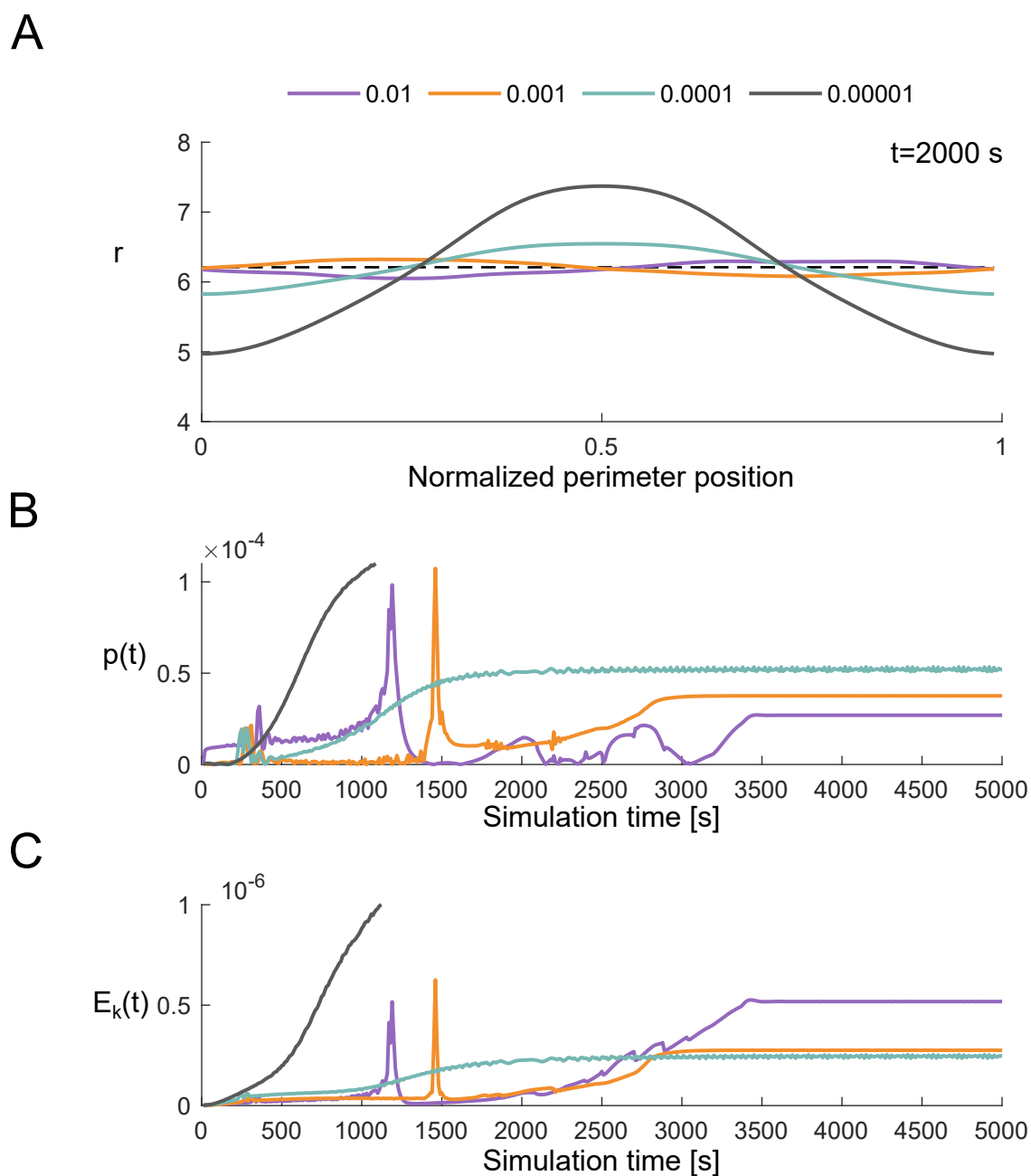


Figure 2.6: Radius error, average momentum and kinetic energy associated with the point on the mesh for cell translating with constant velocity (ii). **Panel A:** Radius profile after  $t = 2000$  s of simulation time. Line colors correspond to the different values of the cutoff  $g_{CO}$ . Black dashed line represents starting radius. **Panel B:** Average momentum magnitude associated with the grid point versus simulation time. Colours correspond to the legend in panel A. **Panel C:** Kinetic energy associated with the grid point versus simulation time. Colours correspond to the legend in panel A.

smallest cut-off value metrics diverge after less than 1000 s of simulation time. The three remaining cut-offs show similar values that saturate in the end. Again our choice of cut-off ( $gCO = 0.001$ ) for subsequent simulations is based on these graphs. We can see that orange line shows best compromise between different metrics and allows for the smallest combined error.

A too-small threshold retains noisy curvature estimates far from the interface, while a too-large threshold artificially suppresses legitimate normal vectors and slows protrusion dynamics. We recommend the following protocol:

1. Start from  $gCO \approx 0.01 \max |\vec{\nabla} \phi|$  evaluated on the initial grid.
2. Run the stationary-circle test for  $10^8$  steps and adjust  $gCO$  such that  $\text{Error}(t_{\max}) < 10^{-2}$ .
3. Re-run with half the grid spacing; if the error decreases by a factor  $\approx 4$  the choice is adequate, otherwise lower  $gCO$  and repeat.

## 2.2.2 Software implementation

This section documents the computer implementation of the discretised model equations and the associated simulation workflow. All numerical kernels are written in ISO C99, chosen for its speed, predictable memory layout, and straightforward portability. The code base consists of two translation units:

- `main.c` — reads the `.json` parameter file, loads the initial NetCDF snapshot, allocates arrays, and sets run-time options;
- `simulation.c` — contains the time-marching loop, numerical stencils, Jacobi pressure solver, and I/O wrappers.

The remainder of the section is organised as follows: Subsection 2.2.2 summarises external dependencies; Subsection 2.2.2 outlines the directory structure and data layout; Subsection 2.2.2 reports wall-times on representative grids. The full code can be obtained from publicly available GitHub repository<sup>3</sup>.

### Dependencies

Only two external libraries are required, both distributed under permissive open-source licences:

1. **netCDF-C**<sup>4</sup> — scientific array I/O; the Debian/Ubuntu package `libnetcdf-dev` or the `conda-forge` recipe `netcdf-c` installs headers and shared objects automatically. Compilation is entirely optional at run-time, so the library can be linked statically for portability.

<sup>3</sup><https://github.com/blejzara/CellRDA-LS>

<sup>4</sup><https://github.com/Unidata/netcdf-c>

2. **cJSON**<sup>5</sup> — ultra-lightweight JSON parser used to read `input.json`. The repository provides a single `cJSON.c/cJSON.h` pair that can be dropped into the project and compiled together with the simulation code.

All remaining functionality relies solely on the ISO C99 standard library, avoiding platform-specific extensions. For Windows users without a native Unix-like environment, we recommend MinGW-w64 together with the `conda-forge` channel, which supplies pre-built netCDF binaries compatible with MinGW.

### Code architecture

Translation units and entry points:

- `main.c` is the sole executable. It parses the `input.json` parameter file with `cJSON`, loads NetCDF snapshot as initial conditions, allocates all run-time arrays via the `ALLOC_ARRAY` macro (a thin wrapper around `calloc`), and opens the output NetCDF file and binary tracer files. Command-line arguments allow batch submission on a cluster or interactive runs on a workstation.
- `simulation.c` exports a single function `simulation()` that advances the solution by invoking two high-level kernels: `PrepStep()` prepares all auxiliary fields and solves the Poisson problem, while `Step()` performs the forward-Euler update of velocities, level-set, and reaction-diffusion fields.

The main advance routine organises the simulation as a double loop. Between two output times only two copies of every field are kept in memory (current and previous) so the working-set size scales linearly with grid area. At the end of an outer cycle the current state is flushed to NetCDF, and, if enabled, tracer positions are appended to binary files. All arrays are stored in 1-D row-major buffers to maximise spatial locality. The `ALLOC_ARRAY` macro aborts immediately if allocation fails, preventing silent segmentation faults. Inline accessor functions were avoided for performance; instead, index expressions like `row*I + col` are used throughout. The file `simulation.c` also implements:

- two Laplacian stencils `Laplace_1()` and `Laplace_2()`;
- bilinear interpolation `inline Interpolate()` used for tracer advection;
- a tracer-update routine `Trace()` that integrates massless particles with periodic wrapping.

A consistent set of integer error codes is defined near the top of `main.c` (codes 10–99). If any I/O or allocation call fails, the program prints a descriptive message, frees allocated memory, and returns the corresponding code to the shell-facilitating automated regression tests.

<sup>5</sup><https://github.com/DaveGamble/cJSON>

The project targets the ISO C99 standard, which the code requires for features such as `//` comments and inline functions (see `simulation.c`). A minimal GNU the recommended flags are `-std=c99 -Wall -O3 -lnetcdf`. The code has been tested with GCC 13 and Clang 17 on both Linux and Windows/MinGW-w64.

### Code performance

All benchmarks were compiled with `gcc 13.2` at the conventional high-optimisation level `-std=c99 -O3 -march=native -flto -Wall`. Tests were run on:

- **Laptop** – HP Victus 16-e1005nm equipped with an AMD Ryzen 7 6800H (8 cores/16 threads, 3.2 GHz base, 4.7 GHz boost) and 64 GB DDR5 RAM;
- **Cluster** – Padobran (part of SRCE’s “Vrančić” cloud), whose CPU nodes each contain two AMD EPYC 7713 processors (128 Zen 3 cores @ 2.0 GHz) and 512 GB RAM.

Using these settings, a typical production run of  $10^7$  steps on a  $235^2$  grid completes in  $\sim 40$  h on the laptop and  $\sim 60$  h on a single Padobran node. Multi-simulation parameter sweeps were launched as embarrassingly parallel jobs across separate cluster cores, so no OpenMP or MPI parallelism is enabled inside a single run. Adding `-fopenmp` to parallelise the outer loops was tested but gave a net slowdown of 10–15 % because the kernels are memory-bandwidth-bound and the Jacobi pressure solve is inherently serial.

Table 2.2 reports wall-times on **Laptop** per 20000 steps for three grid sizes at the default physics parameter set (Table 2.1). Each entry is the mean of first five save cycles, measured with `clock()` calls embedded in the code. Each save cycle refers to 20000 calls of `PrepStep` and 20000 calls `Step` functions. The forward-Euler update performs only  $O(1)$  flops per double

Table 2.2: Wall-time per 20000 forward-Euler steps (single thread, GCC 13.2, `-O3`).

Grid	$188 \times 188$	$235 \times 235$	$281 \times 281$
PrepStep	66.29 s	70.02 s	99.13 s
Step	11.89 s	23.18 s	33.89 s
Total	78.18 s	93.20 s	133.02 s

loaded from memory, so it is limited by memory bandwidth rather than compute throughput. Splitting the outer loops with `#pragma omp parallel` for increased bandwidth contention and introduced synchronisation overhead, dominating any speed-up from parallel execution.

All computations are performed in double precision; switching to float halves memory traffic and roughly doubles performance, but the gradient cut-off `gCO` must then be reduced 10-fold to preserve the  $< 1\%$  shape error target (see Subsection 2.2.1). Additionally to save

space the solutions could be stored as `float` to save disk space, but this is not implemented in the current version of the code.

### 2.2.3 Supplementary routines for analysis of simulation results

To present the results of simulations, we have developed supplementary routines in MATLAB R2023b (The MathWorks, Inc., 2023). For the simulations where specific metrics are presented (elongation, polarity, Péclet number, etc.) we first exported LS profile and `Rac1T` concentration profile as `.tif` files. The files were loaded into FIJI (Schindelin et al., 2012) with the QuimP plugin (version 19.08.01) (Baniukiewicz et al., 2018) and analysed as explained in the section 3.1.3 to retain consistency across experimental and simulation data.

For stationary cells, the `Rac1T` concentration profile, was plotted from the raw solution values. To extract the flow velocity field and streamlines staggered velocity was first interpolated to the main grid points by using average value at two neighbouring points (using equations (2.16) and (2.17)). Streamlines were obtained from this velocity field using MATLAB's `streamline()` function. Furthermore to extract the mean period of the oscillations and rotations depending on surface tension coupling strength  $k_{\sigma}$  we employed MATLAB's `fft()` function to transfer profile dynamics at every point along the level set contour to the frequency space. Then from the obtained frequency spectrum we determined the dominant frequency at every point using `max` function and subsequently the mean period using `mean()` function.

## 2.3 Behaviour of reaction–diffusion system

In Section 2.1.3 we have laid out basic RD system that can produce the canonical solution types. We will discuss the properties of the solutions without linking concentration profiles to the realistic protein species. One could construct different versions of the RD system but the properties of the solutions would stay largely unchanged. To provide a baseline dynamics of such systems we start by discussing solutions available on a stationary fixed circular geometry. The conditioning of RD dynamics is well documented in the literature (Halatek et al., 2018; Eroumé et al., 2021; Šoštar, 2022), and we present it here for completeness and to validate our approach.

### 2.3.1 Reaction–diffusion dynamics on circular geometry

In canonical RD systems that combine activator-inhibitor, activator-substrate, and mass-conservation properties, three characteristic activator dynamics are typically observed. The simplest of these is static polarization, which can emerge via two distinct mechanisms: the

first described by Turing (Turing, 1952) and the second, specific to mass-conserved systems, introduced by Mori *et al.* (Mori *et al.*, 2008). The other two patterns are characterized by a shifting or travelling polarization patch, as introduced by Gierer and Meinhardt (Gierer & Meinhardt, 1972; Meinhardt & Gierer, 1980). All of the above dynamics can appear with any number of high- and low-concentration zones, depending on the system size, geometry, and total protein number. In this section, we restrict our study to single-peak patterns, for clarity. Three such limit-cycle patterns produced by our model are shown in Figure 2.7.

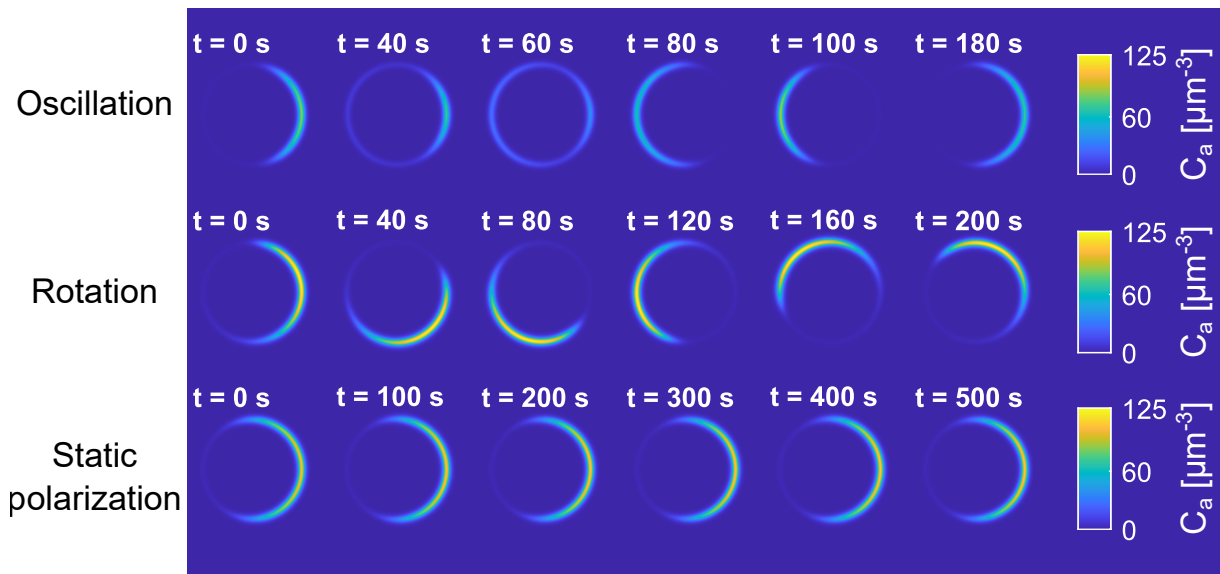


Figure 2.7: Evolution of activator ( $a$ ) concentration on a stationary circular cell. Within our model, three distinct patterns emerge: **oscillation** (top row), **rotation** (middle row), and **static polarization** (bottom row). Colour represents concentration, with colour bars shown on the right. Simulation time for each snapshot is displayed above the frame. **Oscillation** refers to two antipodal  $C_a$  peaks that exchange positions over time. **Rotation** describes a single concentration peak that continuously travels around the cortex (clockwise in this case). **Static polarization** is characterized by a stable, non-uniform concentration profile that does not change in time. Full list of parameters used is listed in Table 5.2.

In the first row of Figure 2.7, we observe how the concentration of the activator  $C_a$  evolves over time under the **oscillation** pattern. Here, the high-concentration patch alternates between opposite sides of the cortex, resembling a standing wave. As with all standing waves, this pattern can be thought of as the superposition of two waves travelling in opposite directions. In this case, the constituent waves need not be single-frequency sine waves; rather, they can be wave packets formed by the superposition of multiple frequency components. Nonetheless, this viewpoint can be useful for conceptualising the underlying dynamics. The oscillation period in this example is approximately 190 s, although it can be rescaled by adjusting the reaction and

diffusion coefficients in the model. In terms of linear stability analysis, this pattern corresponds to a symmetric Hopf-type solution, where “symmetric” refers to each wave component having a counterpart travelling in the opposite direction.

The next pattern, which we refer to as **rotation**, is characterized by a single wave travelling around the cell cortex. Importantly, the wave does not simply diffuse around the cortex; rather, it is continuously degraded at its trailing edge and regenerated at its leading edge. As in the previous case, the high activator concentration ( $C_a$ ) patch is not a simple sine wave but instead a wave packet, with a much steeper front than back. This asymmetric profile is characteristic of bifurcation dynamics. The period of the rotation shown here is approximately 220 s, although, as with oscillation, it can be rescaled by adjusting the reaction and diffusion coefficients. In terms of linear stability analysis, this behaviour corresponds to an asymmetric Hopf-type bifurcation.

The final pattern, which we refer to as **static polarization**, is characterized by a limit cycle in which the cell cortex remains non-uniformly polarized. In Figure 2.7, we observe that a region of high activator ( $a$ ) concentration remains fixed on the right side of the cell for approximately 500 s of simulation time. In the literature, two distinct mechanisms for the formation of static polarization are described. The first, introduced by Turing (Turing, 1952), arises when diffusion and reaction processes balance such that degradation and production (attachment) rates are equal. The second mechanism, specific to mass-conserved systems and first described by Mori *et al.* (Mori *et al.*, 2008), occurs when polarization depletes the pool of available protein molecules, thereby stabilizing the pattern. The example shown in the last row of Figure 2.7 can be considered a Turing-type pattern. A detailed proof is beyond the scope of this thesis, and the reader is referred to the work of Šoštar (Šoštar, 2022; Šoštar *et al.*, 2024) for further discussion.

The three patterns presented above demonstrate that canonical solutions of RD systems emerge naturally in our model. Although we will not return to the detailed discussion of dynamics on a static circular geometry, we will continue to use the naming scheme for the characteristic dynamics established here throughout the remainder of this thesis. With this foundation in place, we now turn to the discussion of geometry-induced modifications to the limit-cycle dynamics described above.

### 2.3.2 Shape effects on reaction–diffusion dynamics

The effect of domain geometry on RD systems has been well documented in both numerical simulations and live-cell experiments (Halatek *et al.*, 2018; Eroumé *et al.*, 2021; Singh *et al.*, 2022; GeBele *et al.*, 2020). Alignment with the long axis occurs because the characteristic length scales of the system are closely linked to the transport processes within the cell. For example,

elongating the cell changes the ratio between the principal axes, thereby altering the length scales in the cardinal directions. These length scales determine the possible positions and sizes of concentration peaks (whether single or multiple). To illustrate this, we repeated the simulations from Figure 2.7, but on a static elliptical geometry (with the same area as the circular domain) and with the initial patch aligned along the shorter axis. The resulting montages are shown in Figure 2.8A.

In Figure 2.8A, we can observe how initiating the simulation on an elongated geometry alters the system dynamics. The most pronounced change occurs for the rotation pattern, which transforms into oscillation aligned with the long axis within a single rotation period ( $< 200$  s). Initially, the patch travels clockwise, but upon reaching the curved end of the ellipse, its motion stalls. After one complete pass around the cortex, the characteristic rotation dynamics are no longer observed, having been replaced by oscillation. This transition occurs reproducibly when the axis ratio exceeds the threshold  $a/b \sim 1.7$ . Alignment with the long axis is evident in Figure 2.8B, where the orange line settles around  $0^\circ$  first, earlier than for the other two patterns.

The remaining two patterns also align with the long axis, although on a longer time-scale. In Figure 2.8B, we see that oscillation (purple line) undergoes two full periods ( $\sim 500$  s) while gradually progressing toward alignment with the long axis, where it eventually settles. In the last row of Figure 2.8A, we observe how this alignment affects static polarization: the patch slowly drifts toward one of the narrow ends of the ellipse, taking approximately 300 s of simulation time. This time-scale lies between the alignment times of the other two patterns, as shown in Figure 2.8B. Once aligned, the patch remains fixed in that position.

Geometry thus has a profound effect on the dynamics of RD systems. This sets the stage for the utility of the full model: once geometry is coupled to the dynamics, we can expect an enriched solution space arising from shifts in the system’s characteristic length scales. Before exploring this coupling, we first examine the effects of transport in RD systems.

### Transport effects on RD dynamics

Since Turing’s seminal work (Turing, 1952), it has been well established that diffusion plays a major role in determining which solutions are possible in an RD system. More precisely, it is the ratio of the time-scales of diffusion and reactions that governs the resulting patterns. To investigate the effects of transport in our RD model, we now examine how the solutions depend on the diffusion coefficients. For this purpose, we initiated two batches of simulations on a stationary circular geometry, using oscillation and rotation snapshots as the initial concentration profiles. The two initial conditions differ in the total protein content in the system: oscillation with  $N_1 = 2300$  and  $N_2 = 700$ , and rotation with  $N_1 = 4000$  and  $N_2 = 1200$ . The label 1 refers

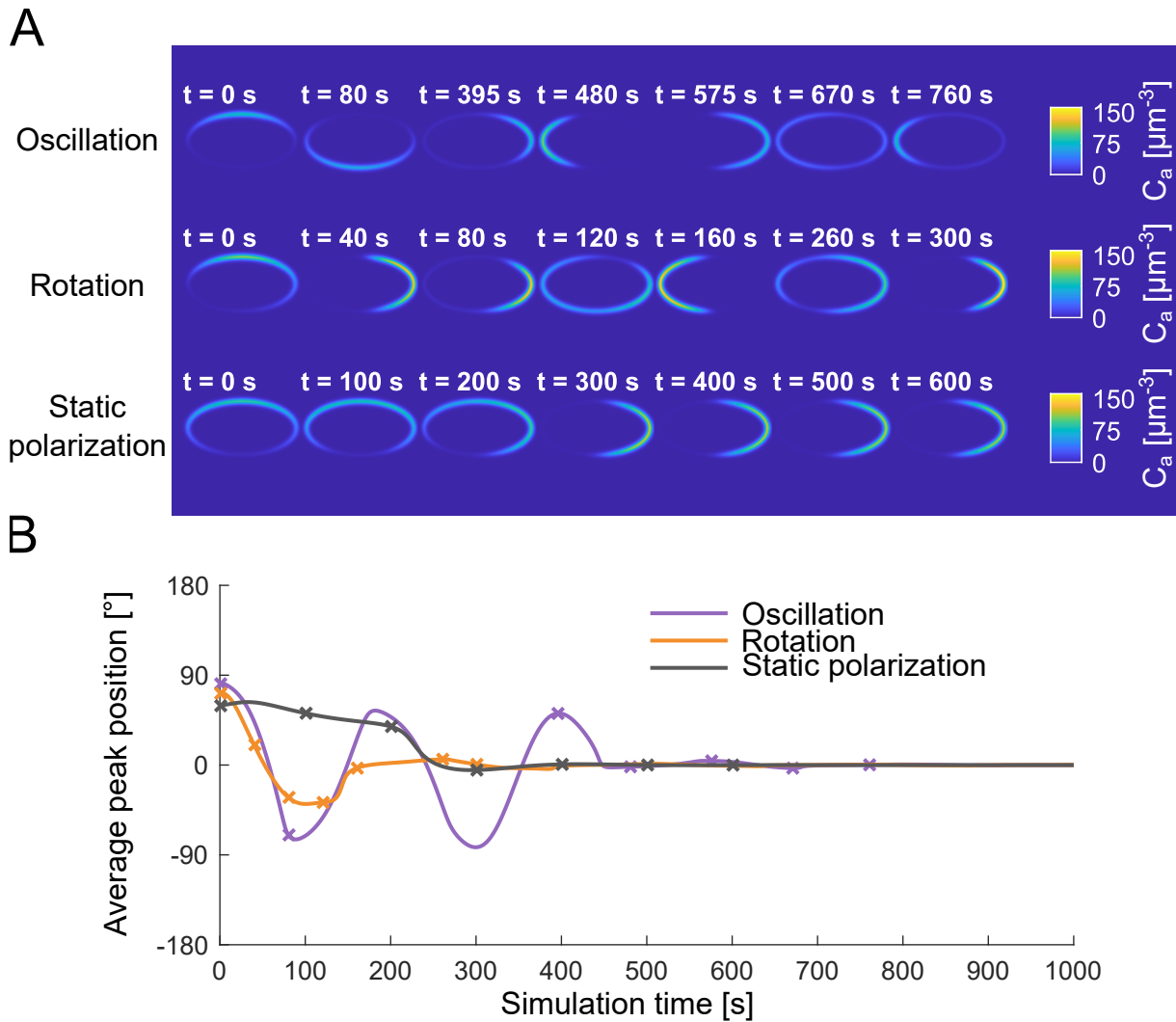


Figure 2.8: Alignment of the dynamics with the long axis of the cell shape. **Panel A:** Same three patterns as in Figure 2.7, initiated on an elongated geometry (axis ratio  $\sim 2$ ). Colour represents concentration, with colour bars shown on the right. Simulation time for each snapshot is displayed above the frame. All three patterns align with the long axis of the ellipse, with the rotation pattern transforming into oscillation. **Panel B:** Weighted average position of the patch versus simulation time for each simulation in Panel A. The angle is given in degrees, with zero defined by the positive  $x$ -axis in the simulations. Crosses on each curve mark the frames shown in Panel A. Depending on the initial pattern, the patch aligns first for rotation and last for oscillation. Full list of parameters used is listed in Table 5.3.

to combined number of molecules of activator  $a$ , substrate  $s$  and complex  $c$ , and the label 2 refers to combined molecule number of inhibitor  $in$  and complex  $c$ .

To explore the effects of transport, we varied two surface diffusion coefficients: those of activator  $a$  and of the complex  $c$ . Bulk diffusion coefficients are at least an order of magnitude higher than the surface values, making their variational effects negligible on the time-scales accessible to our simulations. To further support our choice of surface diffusions for this analysis, we recall the roles of these two protein species in our model. In RD models, it is common to compare the diffusion of the activator with that of the inhibitor or substrate. Accordingly, we selected the activator  $a$  diffusion coefficient as one of the variables. The complex  $c$ , on the other hand, acts as a delayed inhibition mechanism: although it still promotes attachment of  $a$  from the cytoplasmic  $s$  pool, it does so at a rate an order of magnitude lower than  $a$  itself. Furthermore, it sequesters inhibitor  $in$  molecules, preventing them from participating in further reactions. The replenishment of cytoplasmic inhibitor  $in$  therefore depends directly on the transport of this complex around the cortex. Comparing these two diffusion coefficients allows us to subtly tune the overall dynamics of the RD system.

In Figure 2.9, we present the limit-cycle patterns obtained by varying the two selected surface diffusion coefficients for the two initial concentration profiles described above. In both diagrams, the system exhibits a similar response. Increasing activator diffusion promotes the emergence of rotations. This arises because the oscillation pattern is highly sensitive to small asymmetries in the system, which scale with the transport rate. As introduced earlier, oscillation can be viewed as the superposition of two waves travelling in opposite directions around the cortex. If the system is perturbed (e.g., by numerical noise), one of these waves typically overpowers the other. Furthermore, for very low activator ( $a$ ) diffusion ( $D_a = 0.01$ , the smallest value on the diagram), we observe mesa-like concentration profiles. This occurs because the activator diffusion is too slow to smooth out the profile, a phenomenon known as **wave pinning**. This dynamic is specific to mass-conserved systems; for further discussion, the reader is referred to (Šoštar, 2022; Mori et al., 2008).

The effect of increasing complex  $c$  diffusion is the stabilization of static polarization profiles at high values. In both diagrams, the limit cycle transitions to static polarization at a threshold value of approximately 0.7. Furthermore, high activator and complex diffusion coefficients can push the system into a stationary uniform state, effectively shutting down the dynamics, when initiated with higher protein numbers and rotational concentration profiles. Conversely, the same effect occurs for low activator diffusion and high complex diffusion when initiated with lower protein numbers and oscillatory concentration profiles. In the former case, the over-abundance of activator molecules, coupled with their rapid diffusion, suppresses dynamic behaviour. In the

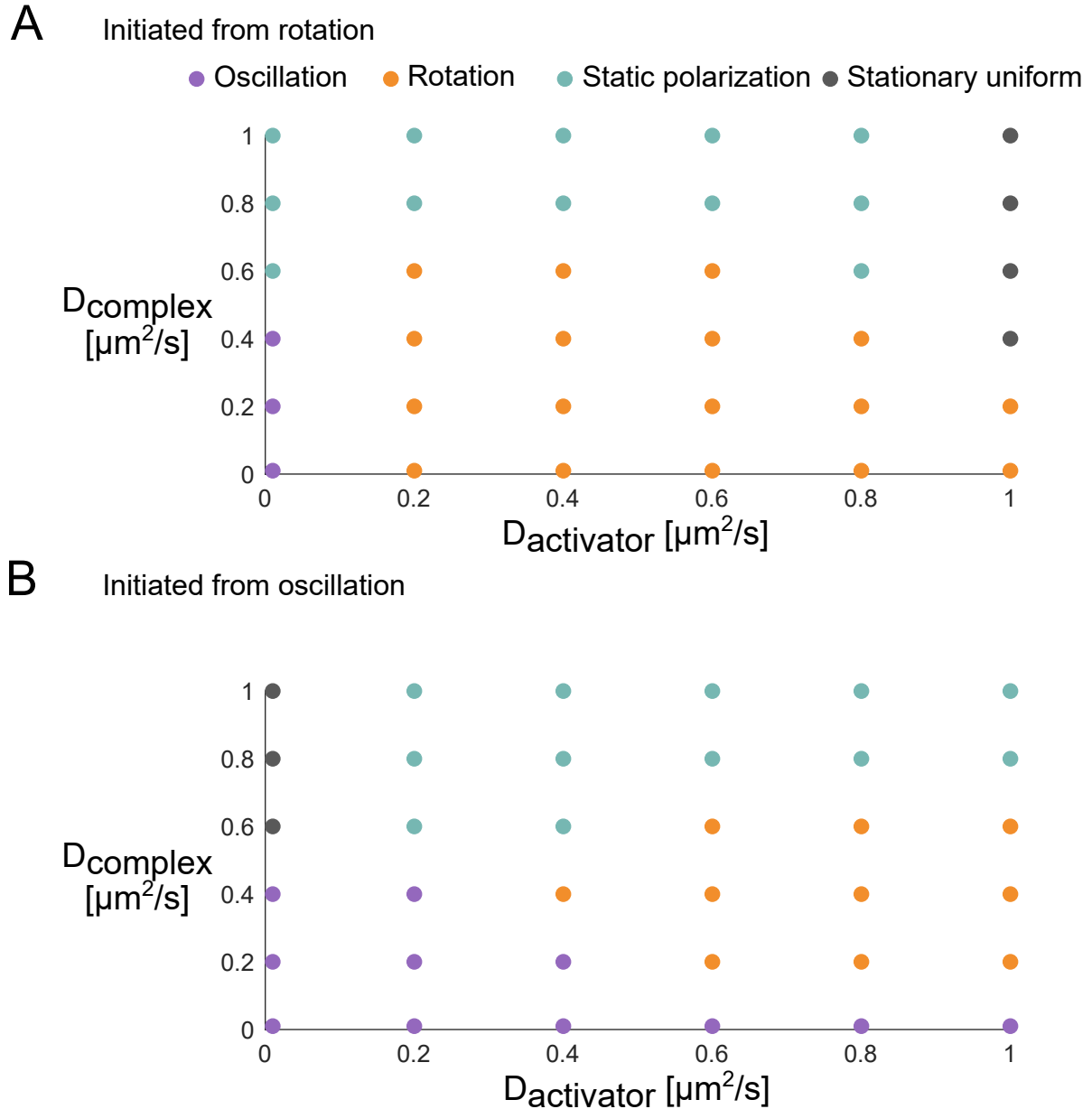


Figure 2.9: Phase diagrams showing limit-cycle patterns on a static circular geometry for different values of surface diffusion coefficients. Activator  $a$  cortex diffusion is plotted on the horizontal axis, and complex  $c$  cortex diffusion on the vertical axis (both panels). The smallest value for both axes is 0.01. The **stationary uniform** state refers to a configuration in which all protein concentration profiles are uniform across their respective compartments and remain stable over time. Limit-cycle classification was determined after 1000 s of simulation time. **Panel A:** Phase diagram obtained from the rotation snapshot as the initial concentration profile, with  $N_1 = 4000$  and  $N_2 = 1200$ . **Panel B:** Phase diagram obtained from the oscillation snapshot as the initial concentration profile, with  $N_1 = 2300$  and  $N_2 = 700$ . Full list of parameters used is listed in Table 5.4.

latter case, the lack of protein molecules, combined with low transport of the activator, leads to the same outcome.

We can thus conclude that, in addition to geometry aligning the activator patch position, diffusion-and therefore transport-plays an important role in determining the expressed dynamics of the system. For all subsequent simulations, we set the diffusion coefficient to a fixed value  $D_a = 0.3$  and  $D_c = 0.1$ . These values place the system well away from the thresholds observed in Figure 2.9, while still allowing the initial state to be shifted with a moderate increase in transport. With this, we conclude our discussion of the RD system and turn our focus to the coupling-induced flows predicted by our model.

## 2.4 Behaviour of fully coupled model

In this section we present the properties of the solutions obtained by our model laid out in Section 2.1. As we have already covered basic RD dynamics we move on to the flows induced by the forces originating from coupling to the activator. One of the flows is generated by protrusive coupling and the other by surface tension coupling force. After we have delineated all of the models properties we present the classification of the solutions available to our model. To conclude this section, we summarize our finding with a phase diagram relating coupling strengths to class and shape of the simulated cells.

### 2.4.1 Flows induced by coupling

As shown in the previous section, our model successfully reproduces the main canonical RD patterns. Moreover, it responds to both imposed geometry and the reaction-diffusion balance. To further analyse this behaviour, we included two coupling mechanisms through which the activator,  $a$ , can induce motility and shape change. Specifically, these are: (i) **protrusive coupling**, which mimics the force generated by polymerizing actin filaments that push the cortex forward, and (ii) **surface-tension coupling**, which modulates cortex tension depending on the concentration of the activator. The system's behaviour is therefore directly determined by the strengths of the coupling constants  $k_C$  (protrusive coupling) and  $k_\sigma$  (surface tension coupling). For more details on these couplings, we refer the reader to Section 2.1.2 and Equations (2.10) and (2.11).

The forces arising from the two couplings induce a flow of the underlying fluid, which transports both the level-set (LS) function and the protein species localized in their respective compartments (bulk or surface). As discussed in Section 2.3, the transport of protein species, and specifically its relation to the reaction rates, strongly influences the limit-cycle patterns

observed in the simulations. We next present the cytoplasmic and cortex flows generated by the two coupling constants separately. This approach allows for a deeper understanding of how these two forces affect the reaction–diffusion–advection dynamics.

### Protrusive coupling

We first discuss the force that mimics the protrusive effects of actin filaments. Our model does not explicitly include actin protein species; instead, it couples the activator concentration  $C_a$  directly to a normal force via the coupling constant  $k_C$ . In our formulation,  $k_C$  is strictly non-negative ( $k_C \geq 0$ ) and therefore produces a force directed outward from the interface. This force generates a flow in the underlying fluid, propelling the cell and transporting the protein species within it. Recent findings, both numerical and experimental (Niwayama et al., 2016; Htet & Lauga, 2025), report that two characteristic vortices form inside a moving cell. In this configuration, fluid flows along the cortex from the front toward the rear, where the two vortices meet, and then returns toward the front along the cell’s central axis, aligned with the direction of movement.

To analyse the flow generated by protrusive coupling within the cytosol, we initiated a simulation of a circular cell with an oscillatory initial protein concentration profile. The protrusive coupling strength was set to  $k_C = 0.04$ , while surface tension was kept constant across the cell cortex. Under these conditions, the simulated cell began moving in the direction of the activator patch. Once the cell reached an approximately steady velocity and shape, we extracted the vector field of the underlying fluid in both the cytosol and on the cortex. The results are shown in Figure 2.10.

In Figure 2.10A, we observe two vortices forming inside the cytosol. The flow pattern is in close agreement with that reported by (Htet & Lauga, 2025). Fluid is carried from the front to the rear of the cell along the cortex, where the two flows meet and turn, transporting fluid from the rear back to the front along the cell’s long axis. Furthermore, inspection of the streamlines reveals that particles trapped within the vortices seldom leave the closed loops along which they circulate.

This type of flow facilitates polarization at the front, where the patch is located. This occurs because it increases the transport of protein species from the rear of the cell directly toward the centre of the patch. This effect can be seen by comparing the direction of flow along the cell’s long axis with the black arrow above it, which represents the polarity vector, and thus the weighted position of the patch on the cortex relative to the centroid. When the two are aligned, the flow carries molecules directly to the most active region of the cortex.

In Figure 2.10B, we see how cortex flow is affected by the cell’s movement. As the cell moves through the surrounding fluid, the flow streams along its cortex, inducing stress on the

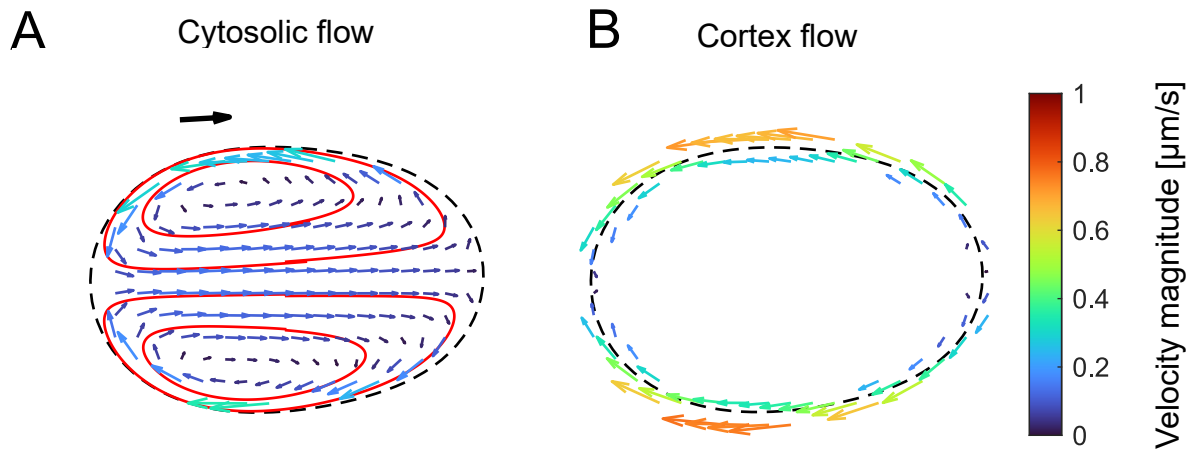


Figure 2.10: Cytosolic and cortex flows in the cell's centre-of-mass frame during movement under the influence of protrusive coupling. The black arrow marks the polarity direction (and, consequently, the direction of motion and the position of the activator patch). Red lines represent streamlines inside the cytosol. The colour scale for both plots is shown on the right. **Panel A:** Cytosolic flow induced by protrusive coupling. Two vortices form, each carrying fluid from the front to the rear along the cortex, meeting at the rear, and then returning fluid from the rear to the front along the cell's long axis. The upper vortex rotates counterclockwise, while the lower vortex rotates clockwise. **Panel B:** Cortex flow induced by protrusive coupling. Flow runs along the cortex from the front to the rear, with the largest magnitude occurring as it passes the cell midpoint. Full list of parameters used is listed in Table 5.5.

cortex as it is dragged along. The resulting cortex flow runs from the front to the rear of the cell along the perimeter. Furthermore, we observe that the largest flow magnitudes occur at the  $x$ -coordinate of the cell's centroid, on both the upper and lower regions of the cortex.

The induced cortex flow carries cortical protein species from the mean patch position toward the rear along the perimeter. If the cell moves in a straight line with the patch located at the leading edge, this flow enhances the transport of proteins from the front to the rear. This direction coincides with that in which diffusion acts to disperse the activator  $a$ , thereby effectively amplifying it. As shown in Section 2.3.2, increasing the transport of both surface species (activator  $a$  and the complex  $c$ ) promotes the formation of a static polarization pattern on the cell cortex. In our simulations, we observe a similar effect: once the cell begins to move, it develops a concentration profile resembling static polarization and then persists in travelling along a straight path.

Our model successfully reproduces the cytosolic flow patterns reported by other researchers. Furthermore, by comparing the induced transport directions with the effects of diffusion variation on a stationary geometry, we have shown how such flows influence the dynamics of the RDA

system. Specifically, cortex flow transports complex protein species along the cortex toward the rear, while cytosolic flow resupplies bulk species to the front. Before presenting the combined results of the full model, we now turn our attention to the flows induced by the second coupling force in the following subsection.

### Surface tension coupling

Motile cells are typically polarized, exhibiting a front-rear asymmetry in cortex mechanics (often higher cortical tension at the rear for cell-body retraction) while advancing via actin-based protrusions such as filopodia or pseudopodia at the front (Chugh & Paluch, 2018). To capture this behaviour, our model includes a direct coupling between activator concentration  $C_a$  and cortex tension. The strength of this coupling is given by the constant  $k_\sigma$  (see Equation (2.11)), which may be either positive or negative, allowing us to study cases with either higher or lower frontal cortex tension depending on the sign of the coupling.

The flow arising from variable surface tension is known as **Marangoni flow**, which is directed from regions of lower surface tension toward regions of higher surface tension. As introduced above, we distinguish two cases of surface tension coupling: one for a positive and one for a negative coupling constant. Positive coupling increases the surface tension at the position of the activator patch, whereas negative coupling decreases it. Consequently, for positive coupling, the flow is directed toward the maximum activator concentration, while for negative coupling, it is directed in the opposite direction (toward regions of lower surface tension). We refer to the positive-coupling ( $k_\sigma > 0$ )-induced flow as **constrictive**, and the negative-coupling ( $k_\sigma < 0$ )-induced flow as **dispersing**, both defined with respect to the peak of the activator concentration profile along the cortex.

To analyse the flow emerging from this coupling, we initiated two simulations starting from a circular cell with oscillatory initial concentration profiles. The coupling strength was set to  $k_\sigma = -0.03$  and  $k_\sigma = +0.03$ , respectively. The induced flows inside the cytosol and along the cell cortex are shown in Figure 2.11. As these cells do not necessarily form static polarization patterns, the snapshots were selected to represent general flow profiles in both the cytoplasm and on the cortex.

In Figures 2.11A and B, we observe the flow induced in the cytosol and on the cortex, respectively, for positive coupling. As introduced earlier, this produces a constricting flow that carries fluid toward the peak of the activator. Because the force originates along the cortex, the flow is strongest there (Figure 2.11B). This, in turn, drags the cytosolic fluid, again forming two vortices. The flow carries fluid along the cortex toward the activator patch at the front of the cell and cycles back to the rear along the  $x$ -axis. Comparing Figure 2.11A with Figure 2.10A shows

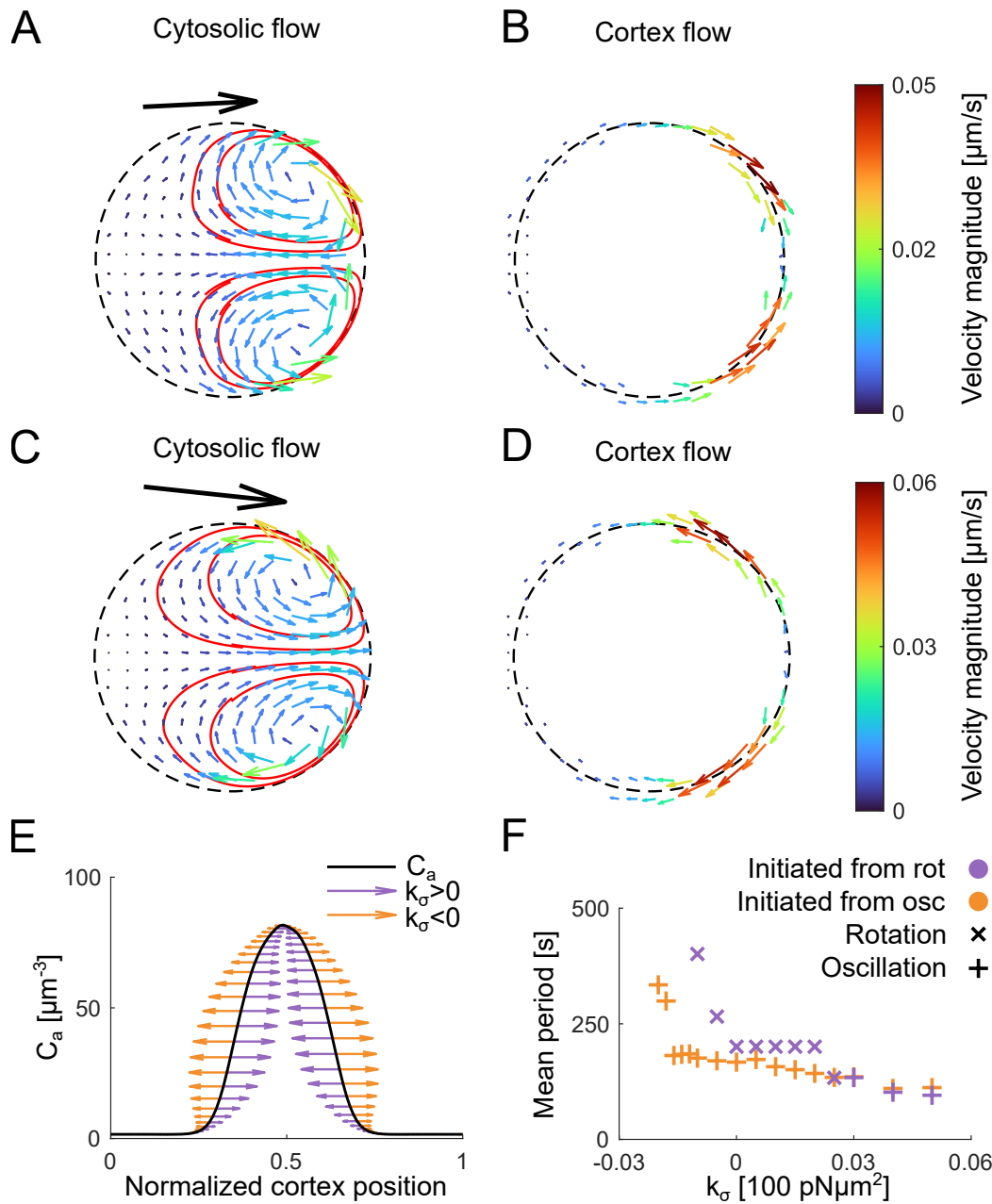


Figure 2.11: Cytosolic (**Panels A and C**) and cortex flows (**Panels B and D**) for the two signs of the coupling constant. Streamlines inside the cytosol are shown as red lines; arrows represent flow direction, and colour indicates magnitude. The colour bar is the same for Panels A and B, and for Panels C and D, and is shown on the far right of each row. The black arrow in Panels A and C represents the polarity vector. **Panel E:** activator concentration profile along the cortex (black line). Relative magnitude and direction of the cortex flow are indicated by arrows for the two coupling signs. **Panel F:** Mean period of oscillation or rotation profile, averaged over 900–1300 s of simulation. Marker determines the pattern at 1300 s, while color reflects the initial concentration profile.

that, in the present case, the streamlines are concentrated at the front of the cell, indicating that transport in the rear is negligible compared to the front. For negative coupling (Figures 2.11C and D), the flow is naturally reversed: fluid moves toward the front along the  $x$ -axis and returns to the rear along the cortex. However, the streamlines reveal that the overall flow characteristics remain the same as in the positive-coupling case (Figures 2.11A and C), with the vortices located at the front of the cell.

The consequence of localized constrictive or dispersive flow is that the rear of the cell becomes largely segregated from the system's dynamics. In other words, protein transport can bypass the rear of the cell, cycling without returning to the back. Nevertheless, two distinct flow directions are still present, meaning the effects on the system are inherently different. Drawing an analogy with the protrusive-flow case, the dispersive flow ( $k_{\sigma} < 0$ , Figures 2.11C and D) influences the system in a similar manner: transport along the cortex is enhanced in the direction of diffusion, and the induced cytosolic flow delivers proteins from the sides of the patch directly to the front. In contrast, constrictive flow counteracts diffusion, effectively squeezing the patch, while the cytosolic flow carries bulk species away from the front and delivers them not to the cell's rear, but rather toward the sides of the patch.

To better understand how this type of flow affects the dynamics of protein species, we need to discuss its origin. The magnitude of the force from which the flow arises (see Equation (2.10)) depends on the tangential gradient of surface tension and, therefore, on the gradient of activator concentration  $C_a$ . In Figure 2.11E, we present a snapshot of the activator concentration profile along the cortex, with arrows indicating the relative force magnitude and direction for the constrictive (purple) and dispersive (orange) cases. The force is largest at the midpoints of the slopes on either side of the peak. Connecting the arrowheads reveals the peak profile that the current force is attempting to achieve: in the dispersive case, it acts to bulge out the peak from its centre, whereas in the constrictive case, it acts to compress it.

As hinted earlier, dispersive flow facilitates static polarization in a manner similar to protrusive flow. To understand the effect of constrictive flow on oscillatory dynamics, it is useful to consider the oscillation as two wave packets travelling in opposite directions along the cortex. When these packets meet, they form a large peak; when separated, a trough forms between them. As shown in figure 2.11 E, the constrictive force pushes the packets toward each other and increases their propagation speed. Consequently, constrictive flow accelerates the oscillation dynamics, reducing the oscillation period as the coupling strength increases (figure 2.11 F). In contrast, dispersive flow slows oscillations at small negative coupling strengths and eventually abolishes them entirely once a negative coupling threshold is reached.

Rotation dynamics respond differently to the two flow types. Under constrictive flow, rotation

transitions to oscillation once a positive coupling threshold is exceeded (0.03 in figure 2.11F). This arises from the inherent asymmetry of the rotating peak: its leading edge (facing the direction of motion) is steeper than its trailing edge. This asymmetry generates a left–right force imbalance, with the constrictive flow preferentially accelerating waves travelling opposite to the peak’s motion. This rebalances the strengths of clockwise and counterclockwise modes, ultimately shifting the pattern from rotation to oscillation. In contrast, strong dispersive flow affects rotation in the same way as oscillation, driving the system into static polarization once a negative coupling threshold is surpassed.

### 2.4.2 Classification of solution phenotypes

We have thus demonstrated how varying the strength and sign of the coupling can produce a wide range of tunable changes in the system’s dynamics. With the underlying transport mechanisms now clarified, we proceed to present the full set of dynamical classes that emerge from different coupling ratios. In our simulations, we observed a wide range of distinct cell behaviours depending on the coupling strengths. Before presenting the full coupling phase diagram, it is useful to introduce each behavioural class. Simulated cells are first divided into **stationary** and **motile** categories, where the stationary cell is defined as a cell if its trajectory remains entirely within the contour that encloses the cell for the entire duration of the simulation. This classification is straightforward in simulations since nearly every simulated cell reaches a stereotypical limit cycle behaviour within the maximum simulation length of  $\sim 1500$  s.

#### Stationary cells

As introduced above, we classify a cell as **stationary** if, for the entire duration of the expressed behaviour, its trajectory remains fully enclosed within the cell’s contour. In our simulations, stationary cells are typically initiated from oscillatory or rotational protein distributions, which remain the dominant modes of RD dynamics in this category. However, with the variation of total number of protein species, we have also observed oscillation dynamics with two simultaneously active regions. Even though number of active regions does not change the inherent RD dynamics, we can clearly distinguish the oscillation pattern with one or two patches by observing the characteristic shape changes. Representative examples of these dynamics are shown in figure 2.12.

In the first row in Figure 2.12 we can observe similar rotational dynamics as presented in Figure 2.7. However, in the example show here one can clearly see the elongated oval shape of the cell. Furthermore, the centroid trajectory of the cell forms a circle, indicating a circular

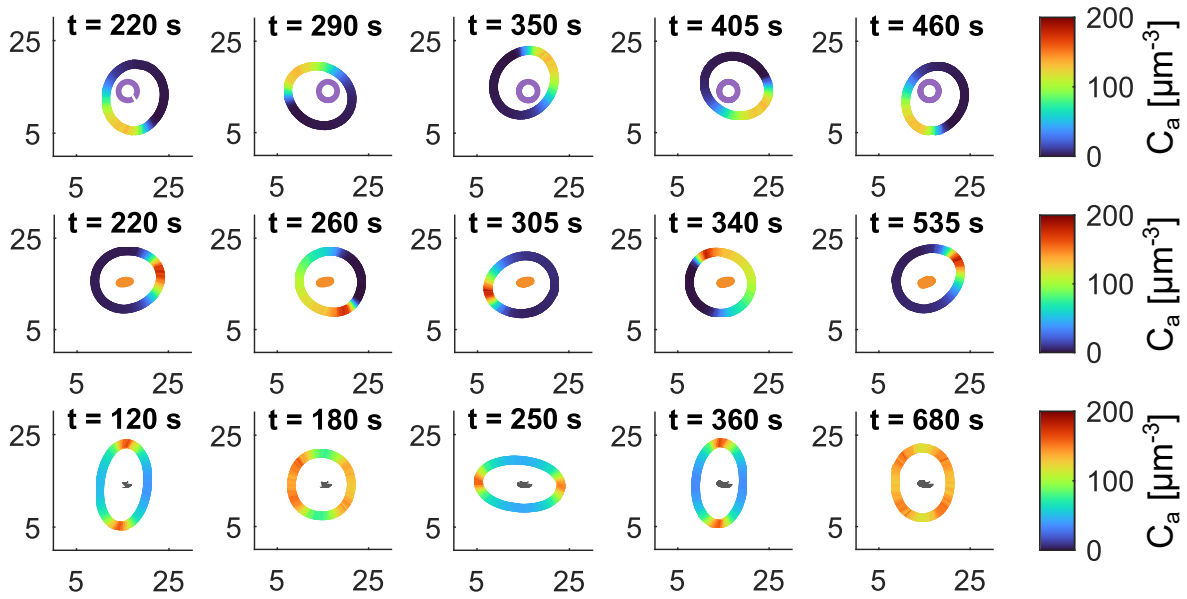


Figure 2.12: Examples of three simulated stationary cells expressing different protein dynamics: **rotation** (top row), **oscillation** (middle row) and **double oscillation** (bottom row). Colour of the contour represents activator concentration ( $C_a$ ), with colour bars shown on the right. Simulation time for each snapshot is displayed above the frame. Purple, orange and gray lines inside the contours represent cell trajectory during the expressed behaviour. Axis labels were omitted for clarity, and represent  $x$  and  $y$  axis of the simulation domain. Full list of parameters used is listed in Table 5.7.

motion of the cell. In the second row in Figure 2.12 we can also see how couplings affect the shape of the cell during an oscillatory activator dynamics. As this cell was initiated with positive surface tension coupling ( $k_\sigma > 0$ ) we can observe the constrictive mechanics that result in an egg-shaped cell. The cell presented here is transitioning from rotational to oscillation pattern resulting in the asymmetry between the two wave packets travelling in the opposite direction. With the longer simulation horizon this asymmetry would eventually disappear because of the effect of constrictive surface tension induced flow (see Section 2.4.1). In the last row in Figure 2.12, we present oscillation pattern with two simultaneously active regions. Similar to oscillation pattern with one patch, activator dynamics can be viewed as four waves travelling around the cortex. As the two wave packets travelling in the opposite direction meet they form a sharp peak in the activator profile. However two such peaks appear on the opposite parts of the cell in within a double oscillation pattern. On the figure, we can see how the cell remains almost perfectly stationary during the expressed behaviour, elongating first in one direction and then

perpendicularly to it.

The most prominent change observed in stationary cells is the acceleration of RD dynamics. As demonstrated in section 2.4.1, large positive values of the surface tension coupling constant  $k_\sigma$  lead to shorter oscillation periods. Similarly, rotational dynamics transition to oscillatory dynamics once  $k_\sigma$  exceeds a positive threshold. This behaviour indicates that RD dynamics dominate over motility, thereby keeping the cell stationary under our classification. In general, cells in our simulations remain stationary when the dynamics of the RD system outweigh advection. However, stationary cells *in silico* can still undergo considerable shape changes, with stronger couplings producing more pronounced deformations. Cells can exhibit egg-like, oval or circular shapes depending on coupling strength. A circular shape arises only for very low couplings. The pointed, egg-like morphology requires sufficient protrusive coupling to sharpen the leading tip as it oscillates with shifts in activator concentration. Conversely, for large positive surface-tension coupling and low protrusive coupling, the cell adopts an oval shape with its long axis perpendicular to the axis of patch oscillation. This arises because the constrictive flow pinches one side before the patch shifts to the other. Nevertheless, for all stationary cells, the RD dynamics consistently lead the shape response. Before turning our attention to purely motile classes we examine one more class.

### Run-and-stop cells

**Run-and-stop** cells fall somewhere between stationary and motile classes. These cells clearly do move, however if the RD dynamics die down or the cell expresses certain static polarization profiles the cell stops after initial sprint. In Figure 2.13, we present the cell which stops after the initial motile segment as the activator dynamics are shut down. This leads to the cell stopping and adopting the circular shape.

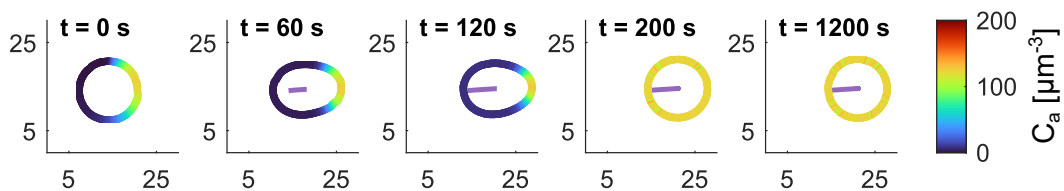


Figure 2.13: Example of simulated run-and-stop cell. Colour of the contour represents activator concentration ( $C_a$ ), with colour bars shown on the right. Simulation time for each snapshot is displayed above the frame. Purple line represents cell trajectory during the expressed behaviour. Axis labels were omitted for clarity, and represent  $x$  and  $y$  axis of the simulation domain. Full list of parameters used is listed in Table 5.8.

Presented cell starts moving in the direction of the polarization vector, while the activator dynamics is shutting down leading to the cell to a still. Within 200 s of simulation time all dynamics has ceased and the cell becomes circular as the forces cancel out due to uniform activator concentration along the cortex. During the motile segment, the cell shown in Figure 2.13 barely translated the length bit longer than its radius. However in our simulations we have also observed cells that move more than this distance, as well as ones which change direction once before the motility stops.

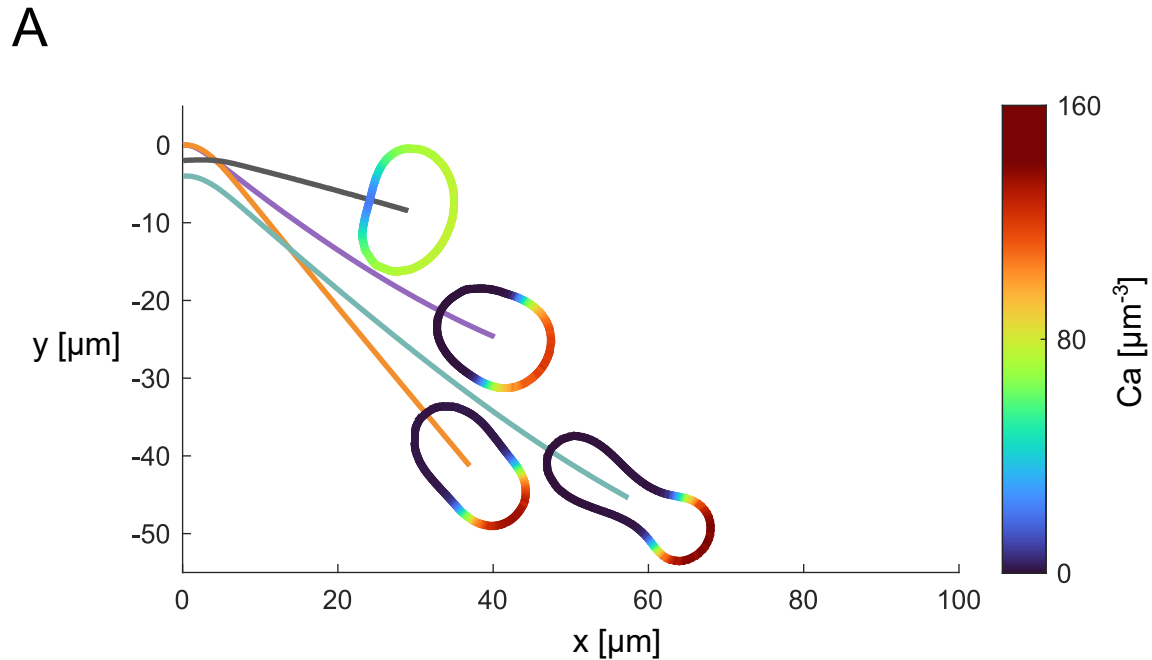
Another type of cell behaviour which falls into this class is characterized by static polarization profiles with two patches. These two active regions on the opposite side of the cell pull in the opposite directions, the cell stays stationary and forms a dumbbell-shape. As the activator profile remains frozen in time the forces cancel out. However, it can occur that the protrusive forces are greater than the surface tension force trying to prevent the cell rupture. In this case the cell splits into two, and we discard such simulation result. Furthermore, as the cell stretches it can cross the periodic boundary of the simulation domain and form a band looping with the boundary. Again we discard such results and will not consider them further here.

### Persistent runners

As introduced in the previous chapter, cytosolic flow arising from protrusive coupling and negative surface tension coupling ( $k_\sigma < 0$ ) promotes stable polarization. Increasing the magnitude of these couplings initiates cell movement, which in turn triggers a positive feedback loop: the accelerating cell induces flows (see sections 2.4.1 and 2.4.1) that transport additional cytosolic protein species to the front, reinforcing the static polarization pattern. Persistent runner cells settle into a stable limit-cycle state, characterised by continuous, straight-line motion.

The shape of persistent runner cells varies with the coupling strengths, as does their centroid velocity. Figure 2.14 presents four examples of persistent runners, each obtained with different coupling ratios and total protein number. However, based on centroid trajectories and RDA dynamics alone, these cells cannot be distinguished. Cell 1 forms a characteristic fan shape, frequently observed in live cells. Elongation and axis orientation depend on the specific ratio of the two coupling constants, a point discussed in more detail later. Cell 2 adopts a stadium-like shape, often with a slightly narrower front compared to fan-shaped cells. For very large protrusive coupling and minimal surface tension coupling ( $k_C \lesssim 0$  and  $k_\sigma \approx 0$ ), the cells take on a dumbbell shape, with a distinct constriction near the midsection. The remaining cell, obtained by total protein number variation, forms keratocyte-like shape with curved front and straight rear cortex. Once the limit cycle is reached, all these shapes remain stable in persistent runner cells.

In the table in figure 2.14 B, we list characteristic values of velocity, elongation, polarity, and



**B**

Simulation	$k_C$	$k_\sigma$	Velocity [ $\mu\text{m s}^{-1}$ ]	Elongation	Polarity magnitude	Péclet number	$N_1$	$N_2$
<b>Cell 1</b>	0.02	-0.03	0.07	0.34	0.8	0.83	4000	1200
<b>Cell 2</b>	0.03	0	0.06	0.84	1.0	0.78	4000	1200
<b>Cell 3</b>	0.04	0	0.10	1.76	1.4	0.80	4000	1200
<b>Cell 4</b>	0.04	-0.04	0.04	0.54	0.1	0.68	2400	200

Figure 2.14: Four simulations belonging to the persistent runner class. The trajectory color corresponds to the cell in the table (panel B). **Panel A:** Cell trajectories (solid coloured lines) and cell contours after 800 s of simulation time (variable coloured lines). Contour color represents activator concentration ( $C_a$ ) along the cortex (color bar on the right). **Panel B:** Coupling strengths ( $k_C$  and  $k_\sigma$ ), protein number and characteristic metrics averaged over  $\pm 50$  s around the time of the plotted contour. For full information about the parameters of the simulation see Table 5.9.

Péclet number for these simulations. Velocity increases with protrusive coupling strength, and its order of magnitude is comparable to experimentally measured values (see figure 3.12). However large negative surface tension couplings do impair this velocity slightly. Elongation depends on the ratio between the two coupling constants: protrusive coupling promotes stretching along the polarity axis, while negative surface tension coupling favours elongation perpendicular to it. This trend is evident in the contours shown in figure 2.14 A and in table B, with Cell 4 exhibiting the greatest elongation perpendicular to the direction of the motion. Cells 2 and 3, on the other hand display larger elongations along the velocity vector.

Polarity magnitude proved to be a strong indicator of motion persistence, a point that will be revisited when discussing other classes. For persistent runners, this magnitude remains nearly constant and reflects the strength of transport driven by cytosolic flow. Only outlier here is Cell 4, whose activator concentration profile is almost uniform around the curved front. Regarding the Péclet number, we used activator surface diffusion coefficient ( $D_a$ ), while the characteristic length and velocity were determined in the same manner as in the experiments to ensure comparability (see Section 3.1.4). In this class, the Péclet number is not necessarily greater than 1, although higher values occasionally occur, particularly for strong protrusive couplings. As shown in figure 2.14 B, persistent runners are not defined by advection-dominated dynamics but rather by characteristic cytosolic flows that amplify, rather than alter, the transport of protein species. In other words, similar solutions could be obtained by increasing surface diffusion, thereby locking the RD system into static polarization.

### Alternating runners

In our simulations **alternating runner** class naturally emerged in cells initiated with oscillatory protein concentration profiles. Once these cells begin to move, the underlying activator dynamics remains largely unchanged, giving rise to the characteristic motion shown in figure 2.15.

As can be seen from the trajectory in figure 2.15 A, the activator patch does not necessarily relocate to the exact opposite side of the cell but instead drifts slightly with each shift. Unlike the rotation pattern observed in stationary cells, here the concentration decreases as the patch transitions to a new location, producing a staggered motion of the cell. This is evident from the contours in panel A, where each snapshot corresponds to a characteristic stage of the patch shift. By “shift” we refer to the time interval between the patch disappearing at one location and reappearing at another, effectively, the period between consecutive runs. This process is also reflected in the polarity magnitude shown in panel B: polarity drops when the entire cortex becomes active. A similar polarity profile can be observed for stationary cells in figure 2.7.

As shown in figure 2.15 B, each run is accompanied by an elongation of the cell body in

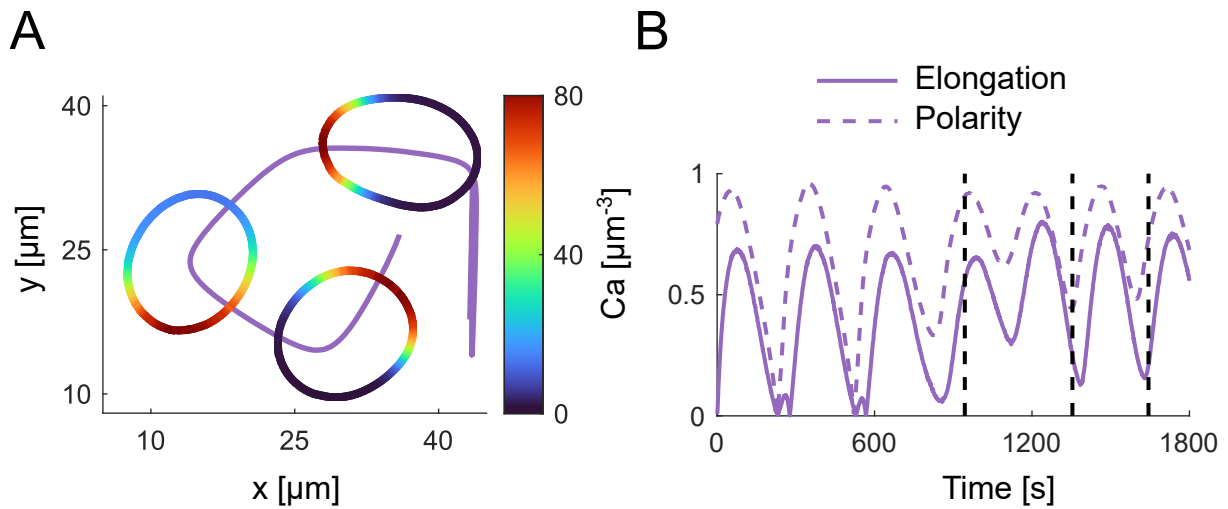


Figure 2.15: Example of an alternating runner cell *in silico*. **Panel A:** trajectory of the cell with contours at three different time points. The color of the contour represents activator concentration ( $C_a$ ) along the cortex, with the color bar shown on the right. **Panel B:** magnitudes of elongation (solid) and polarity (dashed) over the course of the simulation. Dashed black lines indicate the times at which the contour snapshots in panel A were taken. For full information about the parameters of the simulation see Table 5.10.

the direction of motion. This elongation follows the peak polarity expressed during a given sprint. Once the activator patch begins to shift, the forces along the cortex become more evenly distributed, causing the cell to contract back toward a circular shape.

As noted above, this class emerges naturally when the coupling constants are increased in cells initiated with an oscillatory concentration profile. However, alternating runner cells also arise when simulations are initiated with a rotational profile, provided that the surface tension coupling is slightly positive. Recall that positive surface tension coupling ( $k_\sigma > 0$ ) stabilizes and accelerates oscillations in stationary cells; the same mechanism can stabilize cells that initially display rotation. In such cases, the cells typically undergo a transient phase, during which other characteristic behaviours may appear, before settling into alternating runs once the simulation reaches its limit cycle.

### Circular runners

Similar to the previous class, circular runners emerge naturally from stationary cells exhibiting rotation dynamics. In simulations, however, we distinguish two variants. Both trace circular trajectories about a fixed point, but they differ in the alignment between shape and motion (i.e., between the long shape axis and the centroid velocity/polarity). This distinction depends primarily on the ratio of protrusive to surface-tension coupling. For sufficiently negative surface-

tension coupling ( $k_\sigma < 0$ ), the long shape axis tends to be approximately perpendicular to the centroid velocity; conversely, for moderate positive coupling ( $k_\sigma > 0$ ), the long shape axis aligns with the centroid velocity during motion.

Comparison between these two classes is presented in Figure 2.16. As seen in Figure 2.16A,

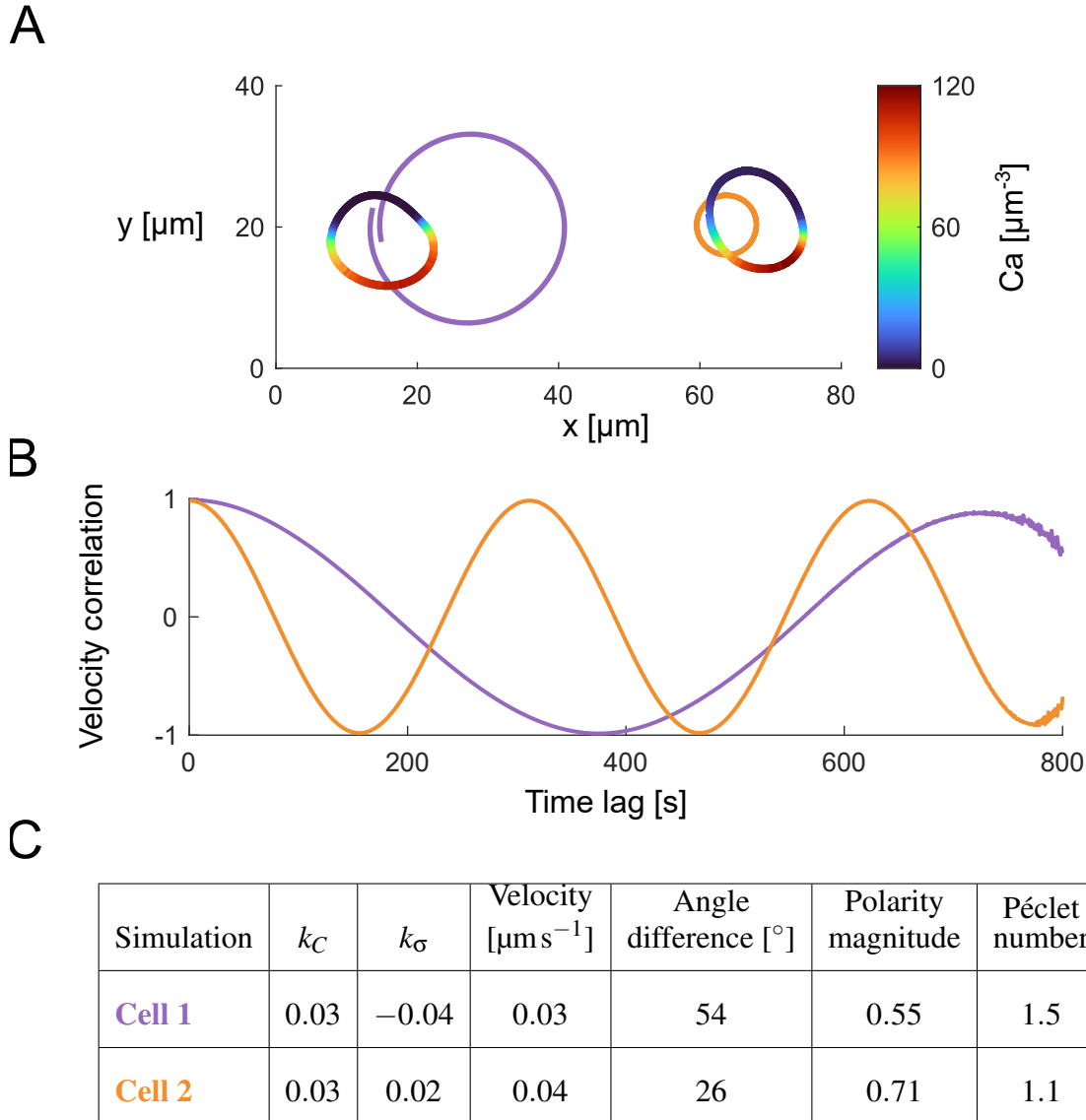


Figure 2.16: Two simulations belonging to the circular runner class. The trajectory colour corresponds to the cell in the table (**panel C**). **Panel A**: Cell trajectories over 800 s of stable limit-cycle dynamics (solid coloured lines) and cell contours at the last frame (variable coloured lines). Contour colour represents  $\text{Rac1}_T$  concentration along the cortex (colour bar on the right). **Panel B**: Velocity autocorrelation function during the time period of the plotted trajectory. **Panel C**: Coupling strengths ( $k_C$  and  $k_\sigma$ ) and characteristic metrics averaged over  $\pm 50$  s around the time of the plotted contour. For full information about the parameters of the simulation see Table 5.11.

the two cells differ markedly in the radius of their trajectories, despite having similar mean velocities (table in Figure 2.16C). The variant with shape approximately perpendicular to the centroid velocity traces a trajectory with about six times the radius. Both cells exhibit relatively high Péclet numbers, consistent with strong coupling-induced advection (Figure 2.16C), indicating advection-dominated transport along the cortex. Notably, however, their centroid velocities are comparable to (or lower than) those of persistent runners; the higher Péclet numbers here reflect stronger internal flows rather than faster centroid motion.

Referring to cells as aligned “parallel” or “perpendicular” with respect to the polarity-shape angle (fourth column in the table in Figure 2.16C) is slightly misleading. Because the rotational initial concentration profile is inherently asymmetric, this asymmetry is reflected in the cell shape. As evident from the contours in Figure 2.16A, an ellipse fitted to each cell would not be exactly parallel or perpendicular to the polarity vector. The angles in Figure 2.16C reflect this: the variant we label “perpendicular” has a mean polarity-shape angle of about  $50^\circ$ , whereas the “parallel” variant is around  $25^\circ$ . We therefore use “perpendicular” and “parallel” only as convenient shorthand for these two typical alignment regimes.

A better way to distinguish between these two variants is by measuring the polarity magnitude. Cell 1 exhibits substantially lower values than Cell 2 (see the table in figure 2.16C). This is a consequence of elongation being aligned with the shape in Cell 2, which adapts an oval shape. On the other hand Cell 1 forms characteristic fan shape with elongated perpendicular to the motion. Finally, as shown in figure 2.16B, both cells produce velocity autocorrelation functions that are essentially indistinguishable from each other and from those measured *in vitro*, the principal difference lies in the period.

### Run-and-turn cells

Finally, we consider the run-and-turn class in simulations. As introduced in the experimental results (Section 3.2.1), this motility class is characterised by straight runs, followed by elongation in a direction perpendicular to motion, which causes the activator patch to shift and the cell to turn. In our simulations, cells expressed this behaviour as a stable limit-cycle solution. One such simulation over 1200 s of simulation time is shown in figure 2.17. The cell appeared as a persistent runner for the first 700 s after which the turning began.

In Figure 2.17A, the cell executes two left turns and one right turn during this time segment. The final turn is further dissected with contour montages in Figure 2.17B. Initially, the cell is fan-shaped and elongated parallel to the direction of motion; as it travels, it elongates perpendicular to the direction of motion. This elongation causes the patch to spread and the concentration to decrease slightly, both of which slow the cell. As the cell decelerates, the patch splits

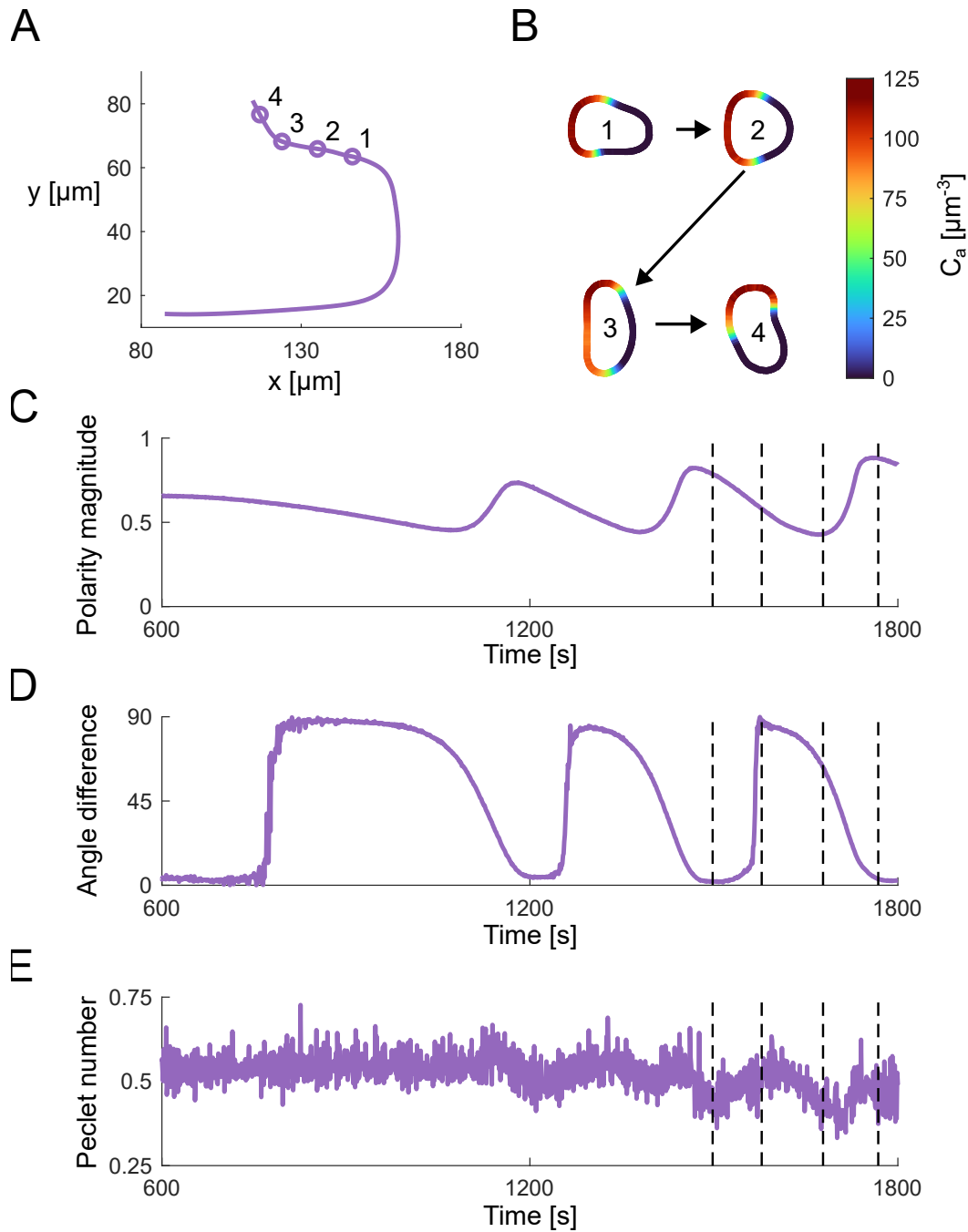


Figure 2.17: Example of a run-and-turn cell *in silico*. **Panel A:** Trajectory of the cell; circles mark the time points at which the contours in **Panel B** were sampled. **Panel B:** Cell contours at four time points. Contour colour represents Rac1<sub>T</sub> concentration along the cortex (colour bar on the right). Dashed lines in **Panels C, D** and **E** indicate the sampling times for the contours in **Panel B**. **Panel C:** Polarity magnitude. **Panel D:** Angle difference between the long shape axis and polarity. **Panel E:** Péclet number. For full information about the parameters of the simulation see Table 5.12.

(Figure 2.17B, contour 3), and ultimately one peak prevails; the cell turns toward this peak and re-forms a fan shape.

Run-and-turn phases are clearly visible in the time series of polarity, Péclet number, and the angle difference between polarity and shape (figure 2.17C–E). Polarity reaches a maximum at the onset of each run and then decreases steadily as the cell elongates perpendicular to the direction of motion. When the patch relocates, the polarity magnitude is abruptly restored, with a much steeper rise than the preceding decay, and the cycle repeats. A corresponding cycle is seen in figure 2.17D, where the angle difference alternates between approximately  $0^\circ$  (alignment) and  $90^\circ$  (perpendicular) and back. As in the experimentally observed run-and-turn cells, the Péclet number distinguishes runs from turns (figure 2.17E): it rises at run onset, indicating increased advective transport, and then drops as the cell slows and reorients, coinciding with patch realignment.

The realignment of the patch with the long axis recalls the results in Section 2.3.2, where the patch consistently aligns with the long shape axis. Inspecting Figures 2.17D and E, we see that realignment begins before the Péclet number starts to decline, suggesting that geometry-driven alignment dominates over advective transport at this stage. In the next section, we examine in detail how the system shifts from persistent runner cells to run-and-turn cells as the requisite ratios and magnitudes of the coupling constants are satisfied.

### 2.4.3 Phase diagrams as a function of coupling strengths

With the classes established, we now examine how the characteristic behaviours arise from the ratio of coupling strengths. In our simulations, the behaviour that determines the class typically manifests as a limit cycle over the simulated duration. Cells were classified at 1000 s of simulation time, and the asymptotic limit cycle may, in principle, differ from the one observed at this horizon. Because substantially longer simulations would require code modifications, we restrict our conclusions to those supported within the stated duration.

To better convey the outcomes of our simulations, we present the phase space defined by the coupling constants ( $k_C$  and  $k_\sigma$ ) in figure 2.18, marking both class identity and characteristic cell shape. We initiated simulations with two different initial concentration profiles, rotation (panel A) and oscillation (panel B), on a circular cell (see Section 2.3.1). The characteristic shapes do not necessarily correspond to the end-of-simulation shape; rather, for each parameter pair we selected the contour that best represents the typical morphology over the simulated interval. The corresponding shape keys are outlined in figure 2.18C.

The two initial conditions were chosen to showcase the broader range of dynamics reproduced

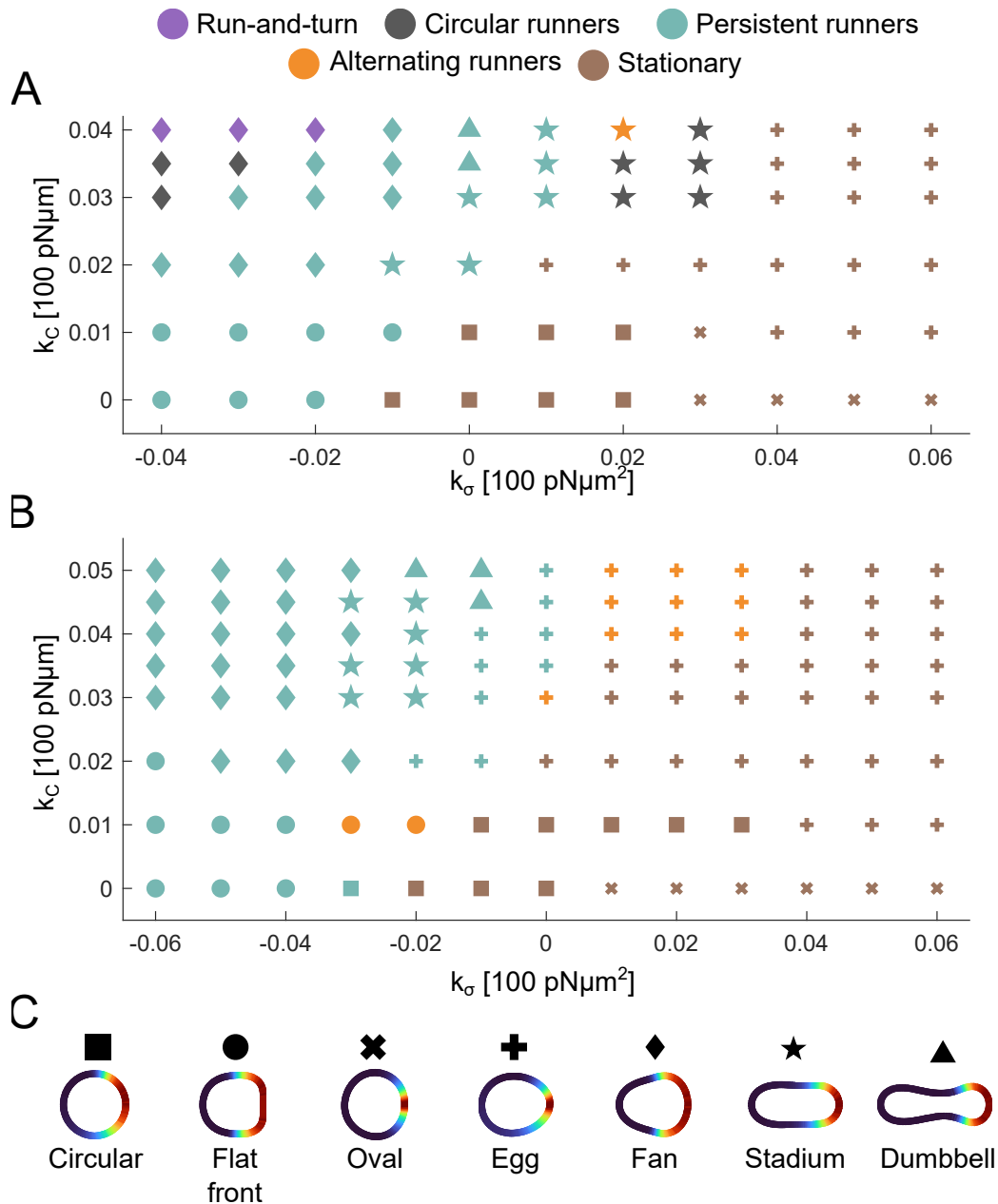


Figure 2.18: **Panel A:** Phase diagram for simulations initiated from a rotational concentration profile (see Section 2.3.1) on a circular cell. The horizontal axis is  $k_\sigma$  and the vertical axis is  $k_C$ . Each marker denotes a simulated parameter pair; marker *colour* encodes the resulting limit-cycle class (e.g., persistent runner, alternating runner, circular runner, run-and-turn), and marker *shape* encodes the characteristic cell shape. Classification was assessed at 1000 s of simulation time. **Panel B:** As in Panel A, but for simulations initiated from an oscillatory concentration profile. **Panel C:** Legend linking marker shapes to representative cell contours. Contours are coloured by activator concentration along the cortex to indicate patch position. The contour shown for each class is a representative shape from the trajectory, not necessarily the final frame. For full information about the parameters of the simulation see Table 5.13.

by our model. Because the oscillatory and rotational initial states differ in total protein numbers, their peak amplitudes also differ; consequently, larger coupling strengths are required for cells initiated from oscillation to achieve the same dynamics as those initiated from rotation. A second key difference lies in the concentration profiles: the oscillatory state is symmetric, providing no built-in symmetry breaking, whereas the rotational state is inherently asymmetric. This lack of initial asymmetry in the oscillatory case affects the cell's ability to express certain behaviours (e.g., those that require directional bias) unless the couplings are sufficiently strong to break symmetry. Below, we interpret the class and shape dependencies observed in figure 2.18.

### Motility phenotypes across coupling ratios

Current state-of-the-art models and experiments (Liu et al., 2021; Eroumé et al., 2021; Htet & Lauga, 2025; Brückner & Broedersz, 2024) indicate that cytosolic flow, cell shape, and reaction–diffusion (RD) dynamics are tightly coupled in motile cells, jointly enabling a wide range of complex behaviours. Recent work also links signalling dynamics to energetic partitioning at the cortex (Chen et al., 2024). Our formulation encapsulates these interacting processes and is consistent with this energy-partitioning perspective.

Reading the phase diagrams in Figure 2.18 along the bottom-right to top-left diagonal in  $(k_\sigma, k_C)$  space (from  $k_C \lesssim, k_\sigma \gtrsim 0$  to  $k_C \gtrsim, k_\sigma < 0$ ), the simulated classes organise as follows. In the lower-right sector (small  $k_C$ , positive  $k_\sigma$ ) we encounter **stationary** cells. As introduced in Section 2.4.1, increasing  $k_\sigma > 0$  accelerates the RDA timescales, stabilising oscillatory RD patterns and preventing sustained shape change or persistent motility. Consequently, for moderate positive  $k_\sigma$ , cells oscillate around a fixed point: protrusion is insufficient to stabilise a static polarisation because the direction of motion reorients too quickly. If  $k_\sigma$  is increased further, the constrictive Marangoni flow compresses the activator patch into a near-point concentration, leading to numerical breakdown; we therefore restrict the diagrams to parameter values for which simulations remain stable.

Moving towards lower (negative)  $k_\sigma$  and higher  $k_C$ , cells become **motile**. For  $k_\sigma < 0$ , the RD dynamics slow down and the dispersive Marangoni flow, together with protrusive forcing, establishes cytosolic and cortical recirculation that reinforces static polarisation. In energetic terms, the flow/shape partition increases, reflected by an abrupt rise of the Péclet number and advection-dominated transport. Because the model is deterministic (perturbed only by numerical noise), trajectories settle into stable limit cycles of directed motion: **persistent runners**. In Figure 2.18B this class occupies the whole top-right corner, whereas in panel A it forms a thinner band; the difference arises because the smaller protein number set by the oscillation-seeded initial condition limits the activator amplitude, and thus forces and flow speeds (Sections 2.3.1,

2.4.3).

Between stationary and persistent-runner regimes lie the **alternating** and **circular** runner classes (Figure 2.18A,B). These are natural continuations of *oscillation*- and *rotation*-type RD patterns on stationary cells, respectively. Constrictive flow at moderate  $k_\sigma > 0$  can convert cells initiated with a rotational profile into alternating runners as their limit cycle; the opposite transition is not observed for oscillation-initiated cells, indicating that an initial asymmetry is required to seed circular runners. Two circular-runner regimes are observed on opposite sides of the persistent-runner region in Figure 2.18A: with large negative  $k_\sigma$ , cells typically exhibit a polarity-shape angle of about  $50^\circ$  (see figure 2.16, Cell 1, purple), whereas for small  $k_\sigma$  (near zero or slightly positive) the long axis aligns with the polarity vector (see figure 2.16, Cell 2, orange). In circular runners the patch remains effectively fixed on the cortex, and turning arises from residual asymmetry in the concentration field. In alternating runners, however, advective transport must at least not oppose RD-driven relocations, so energy redistributes between RD and flow partitions over the run/shift cycle.

At high  $k_C$  with  $k_\sigma < 0$  (upper-left of Figure 2.18) we find the **run-and-turn** class. Strong coupling is required to drive the substantial shape deformations characteristic of this behaviour, and the combination of dispersive Marangoni flow with protrusion-induced flow facilitates alternation between runs and turns. Mechanistically, geometry mediates the decision: as shown in Section 2.3.2, the activator patch tends to align with the long axis. In run-and-turn trajectories this geometry-driven realignment often begins before the Péclet number drops, indicating that shape can dominate advective effects at the turning point. Although run-and-turn emerges robustly in the rotation-initiated diagram (panel A), it does not appear in panel B within the simulated range. We attribute this to the smaller protein number and our chosen coupling limits rather than to a fundamental requirement for initial asymmetry.

In summary, across increasing  $k_C$  and decreasing  $k_\sigma$  the organisation progresses from **stationary** to **persistent runners** to **run-and-turn**, with **alternating** and **circular** runners along the boundary between stationary and persistent-runner regimes. Differences between Figure 2.18A,B reflect shifts in phase boundaries due to initial protein number and symmetry (Section 2.3.1) and the 1000 s classification window.

### Morphology across coupling ratios

Shapes and classes do not align perfectly, a single class can exhibit multiple characteristic shapes. We therefore treat shape separately from motility phenotype and summarise the typical morphologies across coupling ratios. Naming scheme used for characterizing different shapes is presented in Figure 2.18C.

For stationary cells (bottom-left of the diagrams), very low couplings yield a circular shape. With increasing  $k_C$  at positive  $k_\sigma$ , the front constricts and an egg-like shape emerges; here protein dynamics outpace the response of shape and flow, so front constriction pushes opposite the activator patch and net motion is suppressed. Conversely, large positive  $k_\sigma$  with low  $k_C$  can produce a stadium shape whose long axis is perpendicular to the axis of patch oscillation: the constrictive flow pinches one side before the patch shifts, producing a pinching mechanism.

Within the persistent-runner band, a spectrum of morphologies appears (see figure 2.14): oval, fan, and dumbbell shapes arise depending on the coupling ratio. Stadium shapes typically occur at moderate negative  $k_\sigma$  with modest  $k_C$ ; increasing  $k_C$  at small  $|k_\sigma|$  elongates the stadium into a dumbbell, and beyond a threshold the neck pinches and the dumbbell splits (simulations with higher  $k_C$  then fall outside the current model). These shapes are mostly located around very large  $k_C$  at  $k_\sigma \approx 0$

At large negative  $k_\sigma$  with small  $k_C$ , low frontal surface tension straightens the leading cortex, producing a flat-front geometry in which the straight edge coincides with the activator patch (circles in panel C of figure 2.18). Increasing  $k_C$  gradually from this corner elongates the cell in the direction of the motion facilitating fan-shape. The diamond shape (not shown in the diagrams) can arise as a transient between flat-front and fan-shaped cells. When the leading edge becomes highly compliant due to reduced surface tension while protrusive coupling still generates sufficient force to propel the cell, the front transforms from flat to sharp shape. Mechanically, this is analogous to pulling a flexible bag through a fluid by two lateral attachments: the front inflates into a semicircle, while straight segments connect the lateral edges to the pulling point, yielding a diamond-like contour. However given enough time the cell will eventually adopt a fan-shape due to the redistribution of the activator patch.

Our simulations recover fan-shaped geometry when frontal surface tension is sufficiently lower than at the rear ( $k_\sigma < 0$ ). While most motility classes can exhibit a fan-like outline, lower frontal tension appears to be a prerequisite for this specific morphology. Finally, on the right side of the diagrams at small  $k_C$  and positive  $k_\sigma$ , cells can adopt an elliptical shape whose long axis is perpendicular to the polarity vector (marks  $\times$  in figure 2.18C). This typically coincides with oscillatory protein dynamics that pinch the patch-containing region and elongate the cell perpendicular to polarity. Increasing  $k_C$  from this regime yields the aforementioned egg-like morphology (marks  $+$ ).

With this we conclude our analysis of the solutions available to our model. Before we discuss the validation of the model, we need to set the baseline with the behaviour of some motile cells. To this end we present the experiments done on motile amoeba *Dictyostelium discoideum* in the next chapter, after which we present adaptation of our model to this specific organism.

# Chapter 3

## Motility and signalling dynamics in *Dictyostelium Discoideum*

To validate the model presented in chapter 2, we first analyse live-cell behaviour. For this task, we image motile amoebae (*Dictyostelium discoideum*) and classify their motility characteristics. These cells, as introduced in Section 1.4, rely on simplified cytoskeletal machinery to achieve rapid changes in locomotion. Their motile characteristics are governed almost entirely by the actomyosin cortex, with microtubules playing a primarily scaffolding role, and they lack intermediate filaments entirely. This makes them an excellent model organism for studying cell motility.

Furthermore, we are able to image the localisation of the active form of Rac1, a Rho-family GTPase that regulates motility and cytoskeletal reorganisation in *Dictyostelium*. This allows us to track cell shape and motility and relate these to the dynamics of a key regulatory protein. The ability to distinguish between the active and inactive states of this GTPase provides a direct link to the activator in our reaction–diffusion (RD) component. From prior work (Šoštar et al., 2024), we know that cells with minimal displacement in the vegetative state display Rac1-GTP dynamics similar to canonical RD solutions. Taken together, this genetically modified strain of *Dictyostelium discoideum* expressing a fluorescent probe that binds specifically to Rac1-GTP provides a powerful system for validating our model.

### 3.1 Experimental methods

Before presenting and classifying vegetative cell behaviour, we first detail the experimental methods used to acquire live-cell data. We begin by describing cell culture and imaging protocols,

then outline the computational analysis used to extract quantitative measurements. Finally, we define the metrics used to classify cell behaviour; these metrics are applied in the subsequent analysis of motile cell behaviour.

### 3.1.1 Cell culture

*Dictyostelium discoideum* cells, used in experiments were cultivated in polystyrene culture dishes at 23 °C in axenic medium as described in (Faix et al., 2001). Two different cell cultures of parental lineage AX2 were used in experiments. First expressed only the DPAKa(GBD)-DYFP probe constructed as previously described (Filić et al., 2012). The second co-expressed DPAKa(GBD)-DYFP and mRFP-DGAP1. AX2 cells stably expressing mRFP-DGAP1 were transfected with the pDEX-DPAKa(GBD)-DYFP vector also described in (Filić et al., 2012). Cell transfection by electroporation and clonal selection was performed as described (Kimmel & Faix, 2006).

### 3.1.2 Cell Imaging

Prior to imaging, cells were washed with phosphate-buffered saline (PBS, 6.8 pH) to remove residual nutrients. This buffer exchange ensured compatibility with previously established imaging protocols and reduced autofluorescence. Cells were plated in glass-bottom petri dishes and the room temperature was maintained at 22 °C during imaging

The imaging was conducted using a Leica TCS SP8 X confocal microscope equipped with supercontinuum excitation laser (Leica Microsystems) and a 40x/1.3 NA oil immersion objective. Fluorescence signals were excited and detected with the following parameters:

- **DYFP**: Excitation: 511 nm; Detection: 520 nm - 565 nm.
- **mRFP**: Excitation: 575 nm; Detection: 585 nm - 630 nm.

For detection Hybrid HyD detectors were used and operated in gated mode to suppress the parasite reflection from the coverslip surface, and the delay time between excitation and detection was set to 0.3 ns. Time delay between consecutive images in the series was set to 1.27 s or 1.7 s.

In experiments only cells that didn't over or underexpress the probes were selected and imaged for around 10–15 min with the laser power of around 10 % to prevent bleaching. Fluorescence signals were averaged over two frames to improve image quality.

### 3.1.3 Quantitative image analysis

Quantitative image analysis was carried out in FIJI<sup>1</sup> (Schindelin et al., 2012) using the open-source QuimP plugin (version 19.08.01) (Baniukiewicz et al., 2018). The procedure comprised the following steps.

#### Importing and image preprocessing protocols

Raw image stacks in `.lif` format generated with LAS X (Leica Microsystems) were imported into FIJI via *Bio-Formats* as hyperstacks, with the *Autoscale* option enabled. The DYFP channel was then inspected frame-by-frame to identify cells suitable for further analysis on the basis of signal-to-noise ratio, contrast and undisturbed morphology. When available, the mRFP and transmitted-light channels were likewise examined to determine whether the imaged cell came into contact with neighbouring cells at any time point. Cells passing these preliminary checks were flagged, and their entire time series was reviewed once more. Frames in which the selected cell contacted another cell were manually annotated so that they could be excluded in the subsequent qualitative-analysis step.

The image stack was split into individual channels with FIJI's *Split Channels* function in *Color* mode, and each channel was saved as an unscaled `.tif` hyperstack (no bit-depth conversion or additional scaling applied). Because only the DYFP channel carried intensity information for the Rac1-GTP probe and provided the highest signal-to-noise ratio, the mRFP and transmitted-light channels were discarded after the initial screening. The retained Rac1-GTP series comprised  $\sim 500$  frames of  $512 \times 512$ -pixel, 8-bit images (Figure 3.1). This stack was duplicated: one copy served for cell-boundary segmentation, while the second remained unmodified for subsequent fluorescence-intensity quantification.

Before cell tracking and segmentation, the duplicate stack earmarked for segmentation was further pre-processed (Figure 3.2). Background was suppressed by subtracting a constant baseline from every frame with FIJI (*Process*  $\rightarrow$  *Math*  $\rightarrow$  *Subtract*). Baseline values, re-estimated for every cell, ranged from 5–20 grayscale units, obtained by sampling background-only regions and rounding the modal intensity. To enhance edge contrast, the entire stack was then rescaled with *Process*  $\rightarrow$  *Math*  $\rightarrow$  *Multiply*, using an empirically chosen factor (typically 1.5–8). (These operations were applied exclusively to the segmentation pre-processed copy; the duplicate retained for fluorescence-intensity quantification remained unaltered.)

To facilitate segmentation, the pre-processed stack was re-examined frame by frame. Minor artefacts-predominantly background speckles and very thin membrane protrusions (Figure 3.2)-

---

<sup>1</sup>ImageJ, version 1.54p

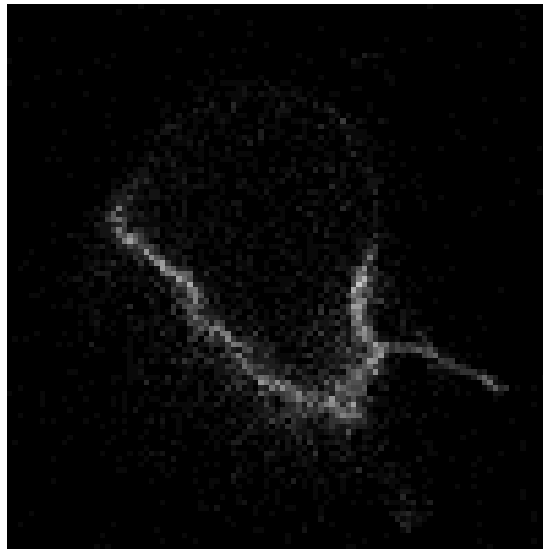


Figure 3.1: Example of raw Rac1-GTP probe DYFP channel after separation.

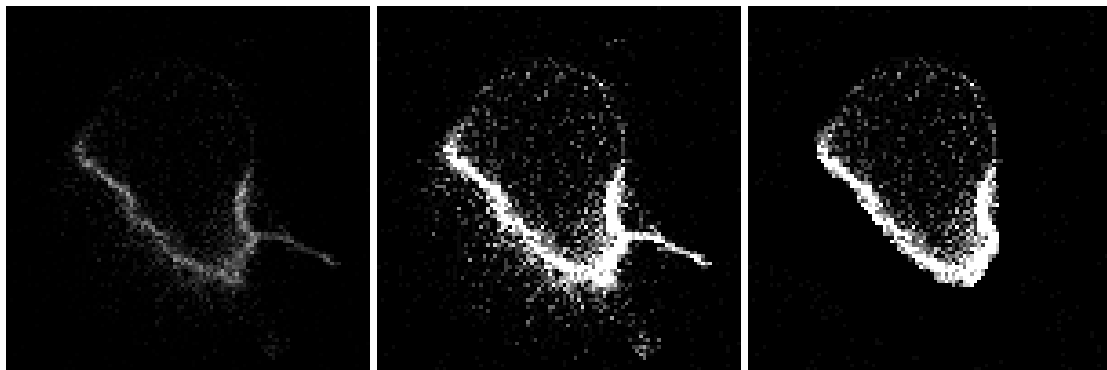


Figure 3.2: Example of intensity data after base value of 7 subtraction (left), after subsequent multiplication by 8 (center) and after manual noise removal (right).

were manually removed with FIJI's *Paintbrush* tool (default radius: 10 px), leaving the genuine cell boundary intact. This step was performed because present study focuses on global Rac1-GTP intensity along the main cortex and on overall cell morphology rather than on every individual filopodium.

### Segmentation and fluorescence analysis

The pre-processed DYFP stack was segmented with Quimp's BOA (Boundary-based Object Analysis) module to obtain a closed cell outline for every frame. Robust results were obtained with the following parameter set: *node spacing* = 2 px; *maximum iterations* = 4000; *critical velocity* = 0.003; *Image F* (image force) = 0.15–0.25; and *Final Shrink* = 2–5. All other BOA

settings were left at their default values or adjusted only marginally.

After the batch run (Figure 3.3) every frame was visually inspected. Frames in which the contour appeared jagged or failed to follow the true membrane were re-segmented with minor parameter tweaks (typically a  $\pm 1$ -step change) until the cortex was accurately delineated.

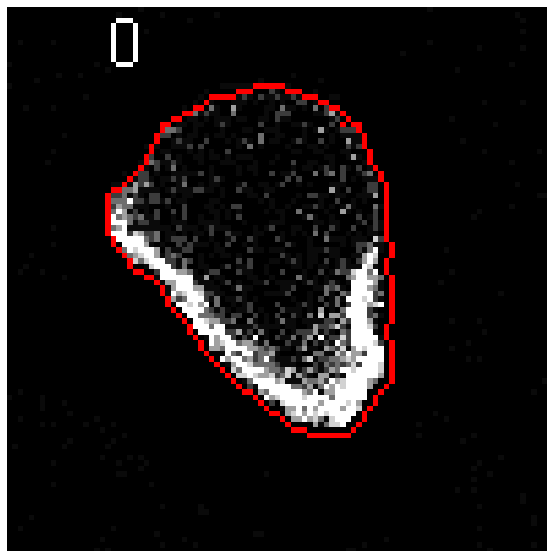


Figure 3.3: Example of preprocessed segmented cell. Red line represents the extracted piecewise linear contour

After segmentation was finished, the pre-processed DYFP stack (used solely for contour extraction) was closed, and all further measurements were performed on the duplicate, unprocessed DYFP stack. QuimP stores segmentation output in its proprietary “QP” format, producing five files for each movie-`.pgQP`, `.paQP`, `.snQP`, `.stQP.csv`, and a master `.QCONF`-that together record the pixel grid, perimeter coordinates, skeleton, time-resolved statistics, and global settings. Spatial correspondence between successive contours was then established with QuimP’s ECMM (Electrostatic Contour Migration Method) module (Figure 3.4). ECMM links homologous nodes frame-to-frame, appending the resulting track information to the existing QP set. The enriched dataset served as the basis for subsequent fluorescence-intensity sampling along the mapped cortex. The details of the tracking method can be found in (Tyson et al., 2010).

The final step of the quantitative work flow was to sample Rac1-GTP fluorescence along the mapped cortex with QuimP’s ANA module (Figure 3.5). The sampling band was set to 0.7–1.4  $\mu\text{m}$ , wide enough to encompass the cortical fluorescent belt while excluding most cytoplasmic signal. The Normalise to interior option was enabled so that, at each frame, membrane intensities were rescaled to the mean fluorescence of the cell interior, compensating for photobleaching and for occasional laser-power adjustments during acquisition. ANA constructs

Frame map 1 to 2

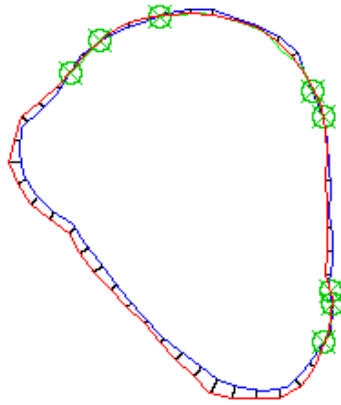


Figure 3.4: Example of mapping contours from one frame to the next using ECMM.

this interior reference automatically from the inner contour generated by shrinking the cortex by the user-defined width. For every node of the outer contour (node spacing was 2 px, as set during BOA segmentation), ANA migrates the node radially inwards to the inner contour while recording the maximum of a  $3 \times 3$ -pixel stencil of intensities encountered en route. This procedure provides one fluorescence datum per contour node and therefore inherits the same angular resolution as the segmentation.

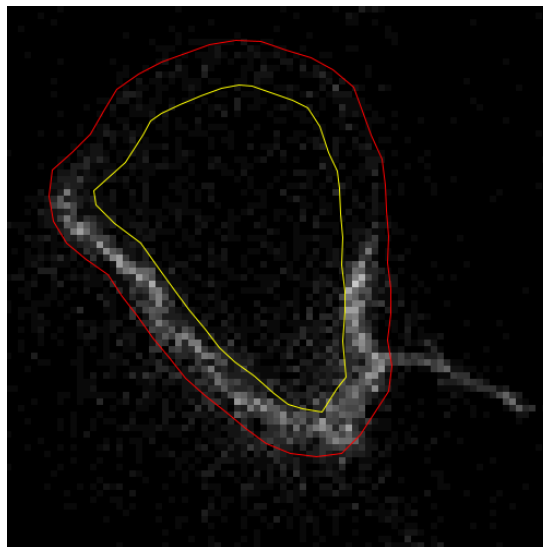


Figure 3.5: Example of outer (red) and inner (offset contour - yellow) contours used for ANA analysis.

The node- and frame-resolved data stored in the QP files were converted to MATLAB

matrices (MATLAB R2023b (The MathWorks, Inc., 2023)) with the unmodified conversion scripts supplied by the QuimP authors. The resulting datasets were saved as `.mat` files for downstream statistical analysis and visualisation. For transparency and reproducibility, the MATLAB routines (`convertQP2Mat.m`, `assembleAnaMat.m`, etc.) can be obtained from the project’s supplementary repository at [warwick.ac.uk/.../quimp/test\\_data/](https://warwick.ac.uk/.../quimp/test_data/)<sup>2</sup>

### 3.1.4 Qualitative Image Analysis

The qualitative analysis sought to characterize both cell morphology and Rac1-GTP dynamics over time. All post-processing was performed in MATLAB R2023b (The MathWorks, Inc., 2023) (build 23.2.0.2409890 Update 3) with Statistics & Machine Learning Toolbox and Image Processing Toolbox v23.2. Custom scripts received (i) contour tables exported by the BOA module and (ii) membrane-intensity profiles produced by the ANA module.

For every frame, BOA and ANA return arrays of contour nodes and their fluorescence intensities. Because the physical node spacing is fixed (in pixels), the number of nodes varies with the instantaneous cell perimeter. The ECMM module links homologous nodes between consecutive frames and re-orders them such that node  $i$  always refers to the same relative position along the cortex. Thus each frame is represented by an array of  $N_F$  nodes where node  $i$  stores (i) its normalized arc-length coordinate  $s_i \in [0, 1]$ , (ii) its Cartesian position  $(x_i, y_i)$  in pixels, convertible to  $\mu\text{m}$  through the microscope’s pixel size, and (iii) the associated membrane intensity  $I_i$ .

Raw QuimP outlines were used as is only for moment-invariant and curvature calculations. For all other analyses the node arrays were resampled with `interp1` onto a fixed grid of  $N = 100$  equally spaced  $s$ -positions. Arc-length parametrization is essential: highly non-convex shapes would map multiple distinct membrane points to identical polar angles, causing aliasing and loss of spatial detail.

#### Moment invariants

Moment invariants provide compact, rotation- and scale-independent descriptors of cell shape. Following Dunn & Brown (Dunn & Brown, 1990) and Teague (Teague, 1980), we computed raw, central and normalised central moments of the discrete outline.

<sup>2</sup>Direct download of the routine bundle: [https://warwick.ac.uk/fac/sci/dcs/people/till\\_bretschneider/quimp/test\\_data/quimp11\\_matlab.zip](https://warwick.ac.uk/fac/sci/dcs/people/till_bretschneider/quimp/test_data/quimp11_matlab.zip).

For a set of outline points  $(x,y)$  the  $(j,k)$ -th raw moment is

$$m_{jk} = \sum x^j y^k. \quad (3.1)$$

The zeroth moment  $m_{00}$  equals the area enclosed by the interpolated outline. The centroid is obtained from the first-order raw moments:

$$\bar{x} = \frac{m_{10}}{m_{00}}, \quad \bar{y} = \frac{m_{01}}{m_{00}}. \quad (3.2)$$

Central moments, invariant to translation, are

$${}'m_{20} = m_{20} - m_{00}\bar{x}^2; \quad {}'m_{11} = m_{11} - m_{00}\bar{x}\bar{y}; \quad {}'m_{02} = m_{02} - m_{00}\bar{y}^2. \quad (3.3)$$

Scale invariance is achieved by normalizing the central moment with area enclosed by the outline

$${}''m_{jk} = \frac{{}'m_{jk}}{m_{00}^{j+k+2/2}}. \quad (3.4)$$

Hence  ${}''m_{00} = 1$  and  ${}''m_{10} = {}''m_{01} = 0$ . The outline is rotated so that its second-order inertia axis aligns with the  $x$ -axis. The required angle is

$$\phi = \frac{1}{2} \arctan\left(\frac{2{}''m_{11}}{{}''m_{20} - {}''m_{02}}\right), \quad -\frac{\pi}{2} < \phi < \frac{\pi}{2}. \quad (3.5)$$

After rotation the mixed second-order moment vanishes, leaving the principal moments

$${}'''m_{20} = {}''m_{20} \cos^2(\phi) + 2{}''m_{11} \cos(\phi) \sin(\phi) + {}''m_{02} \sin^2(\phi), \quad (3.6)$$

$${}'''m_{02} = {}''m_{20} \sin^2(\phi) - 2{}''m_{11} \cos(\phi) \sin(\phi) + {}''m_{02} \cos^2(\phi). \quad (3.7)$$

The equimomental (Legendre) ellipse that matches these principal moments has semi-axes

$$a = 2\sqrt{{}'''m_{20}}; \quad b = 2\sqrt{{}'''m_{02}}. \quad (3.8)$$

Following Dunn & Brown, two log-transformed descriptors are used:

$$E = \log_2\left(\frac{a}{b}\right), \quad D = \log_2(\pi ab), \quad (3.9)$$

where  $E$  measures elongation (zero for a circle) and  $D$  measures dispersion, i.e. how much extra area the outline occupies relative to its inertia ellipse. Moment invariants decouple size,

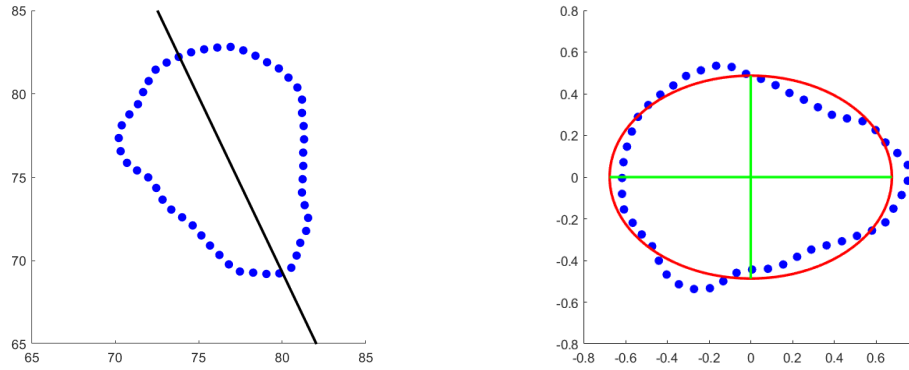


Figure 3.6: Left: original cell outline (*blue*). Right: inertia-aligned outline (*blue*) with fitted Legendre ellipse (*red*); major and minor axis in *green*.

orientation and pure shape, enabling consistent comparisons between cells and across time points.

Raw QuimP sample points (i.e. the original, non-resampled nodes) were used to compute the raw moments and the resulting shape descriptors. The rotation angle  $\phi$  was obtained with MATLAB's `atan2` function, which returns values in the required range  $(-\pi/2, \pi/2)$ . After elongation and dispersion had been calculated, their time series were smoothed with `smoothdata` (method 'gaussian', temporal window = 10 frames).

### Area, radial distance and curvature

For consistency we used the per-frame area reported by QuimP; the value obtained from the zeroth raw moment was discarded, because the raw node set can under-sample highly concave outlines and hence underestimate area. To obtain the distance from the centroid, *i.e.* the cortex radius  $r(s)$ , the raw centroid-centred outline was transformed to polar coordinates with `cart2pol`. The radial component was then interpolated with `interp1(..., 'linear')` onto the common  $N = 100$  arc-length grid defined above.

Curvature  $\kappa(s)$  was evaluated on the same grid. Cartesian coordinates were first resampled with `interp1(..., 'makima')` to guarantee  $C^1$ -continuity. First- and second-order derivatives were approximated by five-point finite-difference stencils

$$x'_i = \frac{x_{i-2} - 8x_{i-1} + 8x_{i+1} - x_{i+2}}{12\Delta s}, \quad x''_i = \frac{-x_{i-2} + 16x_{i-1} - 30x_i + 16x_{i+1} - x_{i+2}}{12\Delta s^2}, \quad (3.10)$$

with identical formulas for  $y(s)$  and periodic (wrap-around) indexing; here  $\Delta s$  is the arc-length

step. Curvature was then approximated with

$$\kappa_i = \frac{x'_i y''_i - y'_i x''_i}{[(x'_i)^2 + (y'_i)^2]^{3/2}}. \quad (3.11)$$

`smoothdata(..., 'gaussian')` was used throughout:

- area time series – temporal window = 10 frames;
- radius and curvature – spatial window = 5 nodes, followed by temporal window = 10 frames.

All radii and curvature values are expressed in physical units after conversion from pixels using the microscope pixel size.

### Intensity signal extraction and polarity calculation

Fluorescence profiles exported by the ANA module were resampled to the common  $N = 100$  arc-length grid with `interp1(..., 'spline')`, and smoothed with `smoothdata(..., 'gaussian')` (spatial window = 5 nodes, temporal window = 10 frames). Let  $I(s, t)$  denote the smoothed intensity matrix (space index  $s \in [0, 1]$ , frame index  $t$ ). Extracted intensity was then used for visualizations and polarity calculation.

We define polarity vector as weighted average radial position with respect to the centroid:

$$\vec{P}(t) = \frac{\int_0^1 I(s, t) \vec{r}(s) ds}{\int_0^1 I(s, t) ds}. \quad (3.12)$$

Were  $\vec{r}$  is radial vector from centroid to the position on the contour. In discrete terms used in analysis the above relation can be written as:

$$\vec{P}(t) = \frac{\sum_s I(s, t) \vec{r}(s)}{\sqrt{a(t)b(t)} \sum_s I(s, t)}. \quad (3.13)$$

The direction of polarity vector marks the mean position of the intensity profile, which for single peak relates to its mean position. The magnitude of the polarity on the other hand relays the information how far away from the centroid is the active region on the cortex. We normalize this value with characteristic cell length  $\sqrt{ab}$  to obtain dimensionless vector quantity. Where  $a$  and  $b$  are semi axes of the Legendre ellipse fitted to the contour of the cell.

### Time correlation and orientation of centroid velocity

Step length of a cell's trajectory was calculated as difference between centroid positions in subsequent steps. To obtain velocity this value was further divided by frame interval. As before,  $\text{atan2}$  was used to provide the velocity angle with respect to x axis. To provide a measure of how the velocity vectors are correlated over time, velocity autocorrelation function (VACF) was determined using the following formula

$$\chi(t) = \frac{(N-t) \sum_{i=1}^{N-t} \vec{v}_i \cdot \vec{v}_{i+t} - \left( \sum_{i=1}^{N-t} \vec{v}_i \right) \cdot \left( \sum_{i=1}^{N-t} \vec{v}_{i+t} \right)}{\sqrt{\left[ (N-t) \sum_{i=1}^{N-t} \|\vec{v}_i\|^2 - \left\| \sum_{i=1}^{N-t} \vec{v}_i \right\|^2 \right] \cdot \left[ (N-t) \sum_{i=1}^{N-t} \|\vec{v}_{i+t}\|^2 - \left\| \sum_{i=1}^{N-t} \vec{v}_{i+t} \right\|^2 \right]}}. \quad (3.14)$$

Here,  $\vec{v}_i$  and  $\vec{v}_{i+t}$  represent the velocity vectors at time points  $i$  and  $i+t$ , respectively,  $N$  is the total number of frames, and  $t$  is the time lag between frames. The numerator measures the covariance between velocity vectors separated by a lag  $t$ , while the denominator normalizes the autocorrelation by the variances of the velocity vectors at the two time points. This ensures that  $\chi(t)$  is dimensionless and lies between  $-1$  and  $1$ , where values close to  $1$  indicate strong positive correlation, and values near  $-1$  indicate strong negative correlation.

### Edge velocity and Péclet number

Quimp analysis provides the immediate velocity of a tracked point. Sign of this velocity depends on whether the point is being extended away or retracted towards centroid, positive for former and negative for latter. As with all other quantities we interpolated this velocity to a fixed  $N = 100$  point grid for every frame of the analysed segment. This velocity was used to obtain the Péclet number approximation.

We defined Péclet number using  $L = \sqrt{ab}$  for characteristic length at each frame, where  $a$  and  $b$  are semi axes of extracted Legendre ellipse. Secondly, when analysing experimental data we opted for a value of  $D = 0.1 \mu\text{m}^2 \text{s}^{-1}$  for diffusion coefficient of membrane bound Rac1-GTP. This value roughly aligns with the literature range which is  $D = 0.05 - 0.3 \mu\text{m}^2 \text{s}^{-1}$  (Machacek et al., 2009). The number was calculated for every frame  $F$ :

$$Pe(t) = \frac{\sqrt{a(t)b(t)} \frac{1}{N} \sum_i |v_{\text{cortex}}(i,t)|}{D} \quad (3.15)$$

### Cell classification method

To classify the cells we used extracted contours and centroid positions. We want to classify cell as stationary if the trajectory of the cell is enclosed by outline for all frames in

the segment. However this strict definition needs to be softened to be useful. We cycled through each of the segment frames and created polygonal shape object in MATLAB using `Shape=polyshape(OutlineX,OutlineY)`, where `OutlineX` and `OutlineY` are arrays holding position of segmentation points, for given frame. We applied a buffer of half a pixel on the `Shape` with `polybuffer(Shape,0.5*PixelSize)`. Then we checked what percentage of trajectory points fall inside the outline and stored the result for that frame.

With the percentage of enclosed points for each frame obtained, we calculated quartile range  $Q$  with `quantile(...,0.05)`. Where 0.05 flag was added to exclude 5 % of the outlier frames. If this quartile range was above a threshold of 0.9 we classify the cell as stationary. Lowering this threshold to 0.85 would include only one more cell into stationary class. This cell could be considered as both stationary oscillation cell or motile alternating runner cell. Because this decision does not affect results presented in this thesis we decided to use the former threshold of 0.90.

## 3.2 Experimentally observed phenotypes

This chapter presents the results of the live-cell imaging analysis. We first describe the criteria used to categorise cell behaviours and then summarise the main statistical findings. As outlined in the *Experimental Methods* section, all experiments were performed with wild-type (WT) AX2 *Dictyostelium discoideum* in the vegetative phase, each sample expressing one or two fluorescently tagged proteins. The maximum imaging duration was 1 h. Before presenting the imaging results, we begin by outlining the methods used for cell classification.

Vegetative AX2 cells exhibit seemingly random, exploratory motility while searching for nutrients (Van Haastert & Bosgraaf, 2009; Li et al., 2011). In contrast, starved cells secrete cAMP, initiating chemotactic migration and subsequent multicellular aggregation, as discussed in the *Introduction* (see Section 1.4). The trajectories of vegetative cells are sometimes described by analogy to bacterial **run-and-tumble** motion, as they alternate between straight or gently curving trajectories and turning or circling phases. Van Haastert *et al.* (Van Haastert & Bosgraaf, 2009) reported that the number of straight-running segments increases as the cells become starved. These motility characteristics could be used to classify cell behaviour; however, such criteria do not account for changes in cell shape or protein dynamics.

Before defining the classification used in this thesis, it is useful to briefly review existing schemes for classifying shape and protein dynamics. In terms of characteristic shapes, *Dictyostelium* cells are most commonly described as either fan-shaped or amoeboid-shaped (Asano et al., 2004; Miao et al., 2017). The latter category is particularly broad, encompassing a wide

array of possible morphologies, and is therefore not always optimal for precise classification. Moreover, the shape of individual cells changes continuously over time. Maeda *et al.* (Maeda *et al.*, 2008) classified these morphological dynamics into three fundamental patterns—*oscillation*, *rotation*, and *elongation*. In the *elongation* pattern, the cell outline becomes persistently stretched, approximating an ellipse and remaining largely stationary with respect to its long axis. The two remaining patterns are intrinsically time-dependent: in *oscillation*, the cell alternates its elongation axis, first extending in one direction and then along an orthogonal direction; in *rotation*, the elongated region of the cortex gradually pivots around the centroid of the cell, producing a rotational motion.

Next, focusing on protein dynamics, spatio-temporal patterns have also been observed in the activity of the small GTPase Rac1. Using a fluorescent Rac1-activity biosensor, Šoštar *et al.* (Šoštar *et al.*, 2024) reported that vegetative cells typically harbour either one or two discrete membrane domains enriched in Rac1-GTP. Based on both the number of domains (monopole vs. dipole) and their temporal evolution, the authors distinguished three dynamic classes: (i) *rotating monopoles/dipoles*, in which the active domain(s) propagate as a travelling wave around the cell perimeter; (ii) *oscillating monopoles/dipoles*, representing standing waves whose intensity fluctuates periodically without lateral displacement; and (iii) *stationary monopoles/dipoles*, where one or two Rac1-rich regions remain fixed at defined membrane sites for intervals exceeding half the characteristic period of the oscillatory and rotational modes.

Our goal here is to classify as many experimentally observed cell behaviours and dynamics as possible. However, none of the classifications presented above can, on its own, satisfy the needs of this thesis. Motivated by this, we developed a custom classification scheme. Before introducing it, we briefly describe how the cell segments to be classified and analysed were obtained. We examined the experimental image data to identify the types of dynamics outlined above, considering both Rac1 intensity patterns and cell motion/shape changes. We restricted our selection to cells expressing only one predominant Rac1 patch on the cortex. In total, we extracted 38 microscopy video segments, each ranging 170–860 s.

As this thesis is primarily focused on motility, we first distinguish between motile and non-motile cells. The classification method is described in detail in the *Experimental Methods* chapter (Section 3.1.4); briefly, cells are divided into two classes: **stationary** and **motile**. A cell is classified as stationary if, for at least 90 % of its outlines (across all frames in the segment), at least 90 % of the cell’s trajectory lies within the outline. Applying this criterion yielded  $N = 7$  stationary segments (2287 s) and  $N = 31$  motile segments (10527 s). We begin by describing the stationary class, followed by each motile class in turn.

### 3.2.1 Phenotype classes

With the primary classification now established, we present the results of the motility-based classification. We further subdivided **motile** cells according to their behaviour in the analysed segments, distinguishing four classes: **Alternating runner** ( $N = 9$  and 4125 s), **Circular runner** ( $N = 8$  and 2450 s), **Run-and-stop** ( $N = 4$  and 626 s), and **Run-and-turn** ( $N = 9$  and 2638 s) cells. Each of these classes is described below, with statistical results presented in the following section. As the focus of this thesis is on motile behaviour, the entire **stationary** class is presented as a single combined group.

One motile cell remained unclassified, as it exhibited alternating runner, circular runner, and run-and-turn dynamics across the full 860 s of microscopy imaging. This cell is presented here as an example of constantly shifting behaviour, illustrating how rapidly a cell can transition between the classes defined above. We therefore selected segments in which cells displayed only one of the presented behaviours throughout the analysed frames. A cell was assigned to a single class and excluded from others, even if it exhibited different behavioural stereotypes in frames outside the selected segment. Our classification thus encompasses the most representative examples we could identify and does not necessarily reflect the true frequency of these characteristic behaviours in the overall population.

#### Stationary

We begin with **stationary** cells. Even though these cells do not move appreciably, their shape can still change. As there is little to discuss regarding their motility, we focus instead on classifying their Rac1 dynamics. Among the 7 stationary cell video segments, we observed only one instance of the **oscillation** pattern, in which the Rac1 patch shifts from one region of the cortex to another. The remaining 6 cells exhibited the **rotation** pattern, where the Rac1 patch travels around the cortex. In stationary cells, this motion of the Rac1 patch is independent of any rotation of the cell body itself. Both patterns were previously reported by Šoštar *et al.*, who referred to them as *rotating monopole* and *oscillating monopole*. As our analysis was restricted to cells with a single predominant Rac1-active region, we note briefly that while dipole and tripole oscillations were also observed, only monopole rotations occurred in our stationary dataset.

For completeness, we present a single oscillation segment and the most clearly visible rotation segment in Figure 3.7. In both examples shown in the figure, the red trajectory line lies entirely within the cell outline. In Panel A, the Rac1-GTP patch (white) circulates counter-clockwise around the cortex. The polarity vector confirms this motion, changing direction periodically while maintaining an almost constant magnitude across frames. In Panel B, the Rac1-GTP patch

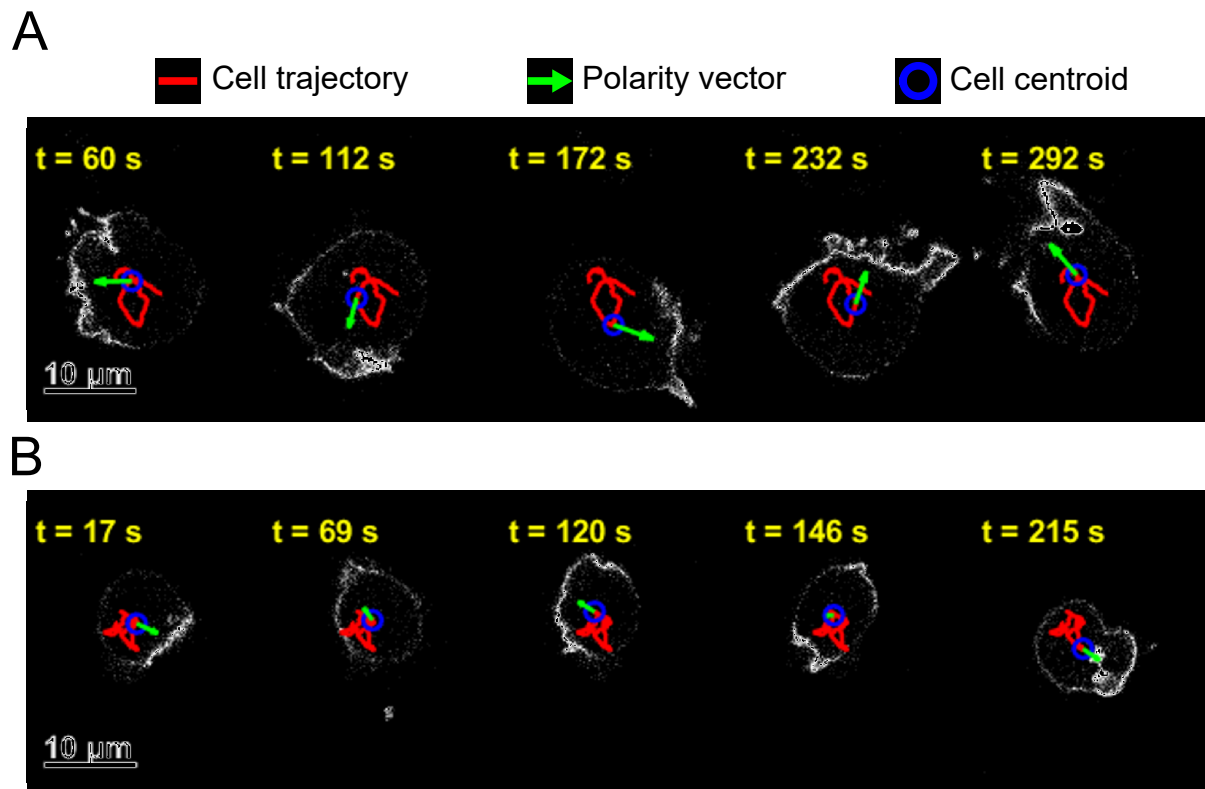


Figure 3.7: Stationary cells. Microscopy image montages showing characteristic Rac1-GTP cortex dynamics. The intensity signal of the Rac1-GTP probe is displayed in grey-scale. The red line marks the cell trajectory across the entire segment, the green arrow represents the polarity vector in the given frame, and the blue circle indicates the current cell centroid. Both panels have equal scale. The time of each snapshot, relative to the start of the classified segment, is shown in yellow above each frame. **Panel A**:: stationary rotation pattern. **Panel B**:: stationary oscillation pattern.

shifts from the south-east region of the cell to the north-east and back. During the shift, the patch transiently splits, producing two smaller patches ( $t = 146$ s) that propagate along the cortex between the main positions of the patch.

The cell shape changes considerably in both examples; however, as noted above, the cell remains essentially stationary relative to its size. These two cases illustrate classic reaction-diffusion (RD) dynamics that are not strongly influenced by cell motion or shape changes. As our primary interest lies in motility, we conclude our discussion of stationary cells here and focus on motile classes for the remainder of this chapter.

### Alternating runner cells

The **alternating runner** class exhibits dynamics most similar to the stationary oscillation pattern. However, these cells traverse appreciable distances between shifts in the Rac1 patch position. Depending on the thresholds used in our classification procedure (see Section 3.1.4), lowering them could result in some alternating runners being reclassified as stationary. An example of the motility dynamics characteristic of this class is shown in Figure 3.8.

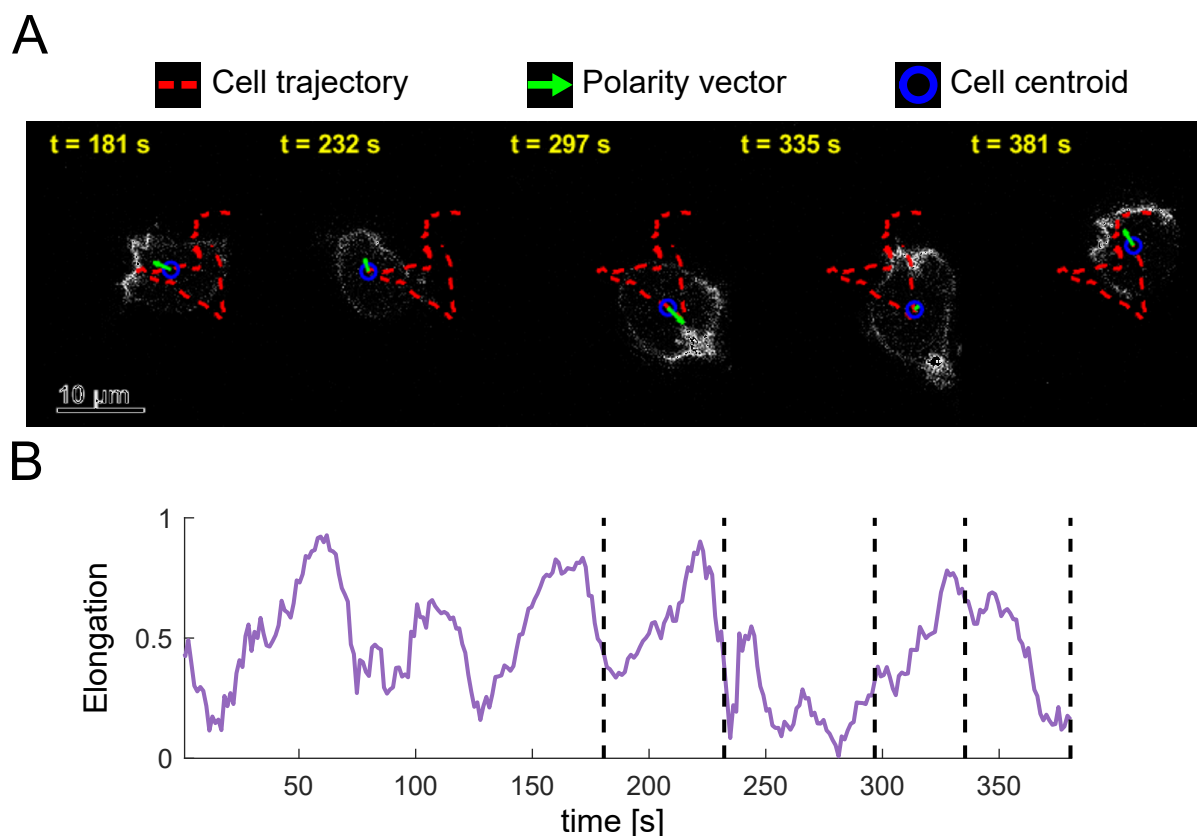


Figure 3.8: Alternating runner cells. **Panel A:** Microscopy image montages showing Rac1-GTP cortex dynamics. The intensity signal of the Rac1-GTP probe is displayed in grayscale. The red dashed line marks the cell trajectory across the entire segment, the green arrow represents the polarity vector in the given frame, and the blue circle marks the current cell centroid. The time of each snapshot, relative to the start of the classified segment, is shown in yellow above each frame. **Panel B:** Elongation versus time. Black dashed lines indicate the frames shown in the montage in Panel A.

One clear difference from the oscillation dynamics observed in stationary cells is the drift of the Rac1 patch along the cortex in alternating runner cells. In other words, subsequent patch positions do not necessarily align along the same axis but can appear at any angle between  $90-180^\circ$  relative to the previous position. The trajectory in Figure 3.8A clearly shows these

changes in direction, with the cell's path ultimately forming a triangular shape.

As the Rac1 patch shifts around the cortex, the cell changes its direction of motion and then pauses before proceeding in a new direction. This behaviour causes the cell body to elongate along the direction of motion and contract to a more circular shape as the Rac1 patch relocates. As noted earlier, such shape dynamics were reported by Maeda *et al.* (Maeda *et al.*, 2008). These elongation cycles can also be observed in Figure 3.8B.

### Run-and-stop cells

In the available data, only four **run-and-stop** cells were observed. This is expected and aligns with the findings of Van Haastert *et al.* (Van Haastert & Bosgraaf, 2009), who reported that non-starved cells display fewer straight runs and more turns or zig-zag trajectories. This trend is reflected in the shorter total duration of video data for this class compared with others. Nonetheless, we did observe this behaviour, which was further characterised by cells coming to a complete stop after a run. As the cell halted, the Rac1 fluorescence intensity faded across the entire cortex, and the cell began contracting in all directions. A montage illustrating one such cell behaviour is shown in Figure 3.9.

As the cells move, they adopt a characteristic fan shape, as seen in Figure 3.9A. The presented cell sprints for approximately 80 s, which is reflected in the decay of the velocity autocorrelation function in Figure 3.9B. Although the short duration of the run results in a relatively noisy correlation function, a decay trend, consistent with pseudo-random persistent motion, is still apparent. Approximately 10–30 s after the cell came to a complete stop and the Rac1 signal was extinguished, it resumed movement and exhibited other behavioural patterns.

### Circular runner cells

At first glance, **circular runner** cells appear similar to stationary rotation cells. However, these cells clearly cover considerable distances, albeit following a circular trajectory. Most of the time, the Rac1 patch appears static on the cell cortex, and the cell's turning motion seems to arise from shape asymmetry. At times, however, the Rac1 patch slips and shifts position around the cortex, always in the direction of the turn. Furthermore, these cells predominantly circle with their axis of rotation nearly coinciding with the inner side of the cell cortex. The motion resembles a body braking on the inside edge and accelerating on the outside edge, thereby running in circles. This characteristic motion is illustrated in Figure 3.10.

The cells frequently display this type of behaviour. For this class, we extracted only those cells that completed a full circular trajectory. Often, cells perform only a half or quarter turn

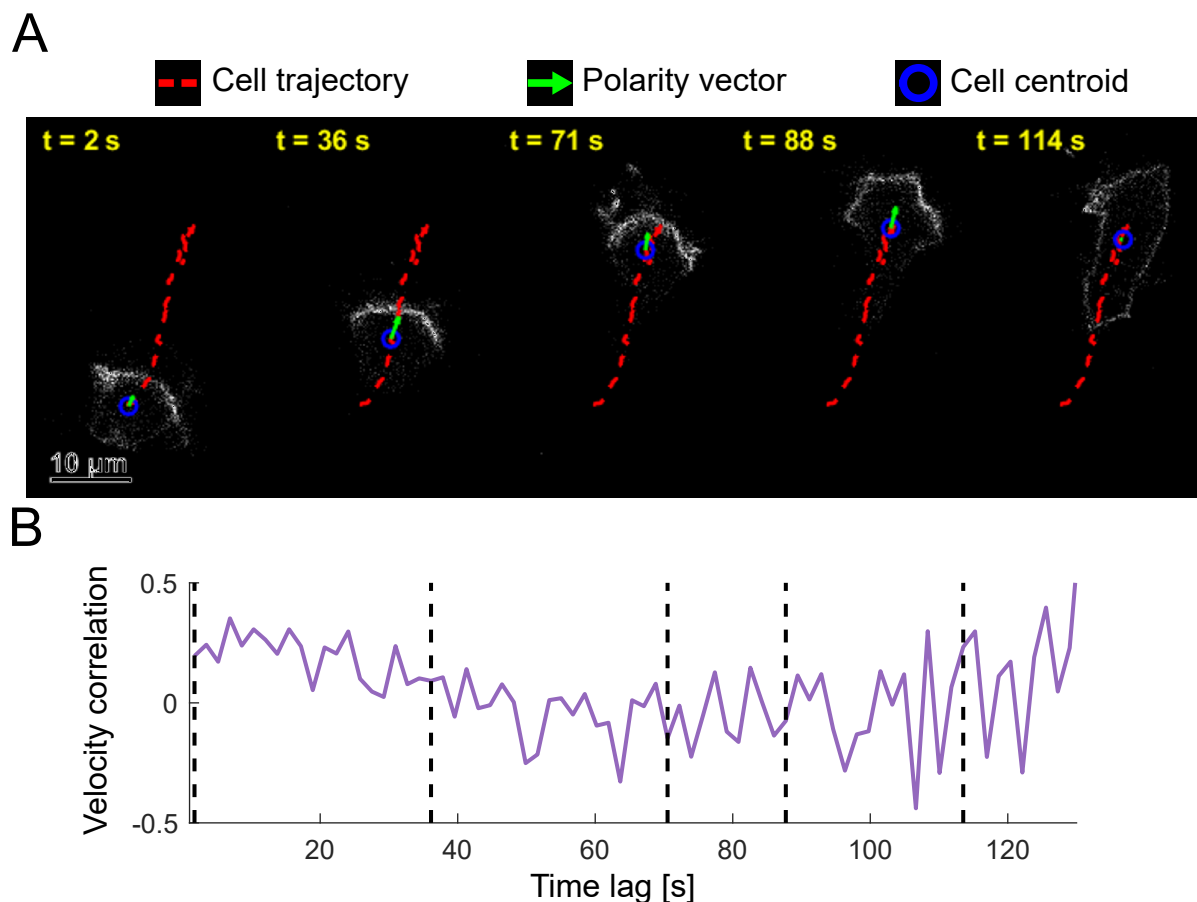


Figure 3.9: Run-and-stop cells. **Panel A:** Microscopy image montages showing Rac1-GTP cortex dynamics. The intensity signal of the Rac1-GTP probe is displayed in grey-scale. The red dashed line marks the cell trajectory across the entire segment, the green arrow represents the polarity vector in the given frame, and the blue circle marks the current cell centroid. The time of each snapshot, relative to the start of the classified segment, is shown in yellow above each frame. **Panel B:** Velocity autocorrelation function versus time lag. Black dashed lines indicate the frames shown in the montage in Panel A.

before switching to an entirely different behaviour. The regularity of this motion is best seen in the velocity autocorrelation function in Figure 3.10 B. The example shown maintained this circular motion for the maximum imaging duration (860 s), resulting in an exceptionally smooth raw autocorrelation curve that clearly reflects the regularity of the motion.

These cells typically exhibit a shape intermediate between a fan shape and an ellipse. Most often, the long shape axis is nearly perpendicular to the polarity direction, as shown in Figure 3.10C. Although the cell occasionally becomes circular or extends in the direction of motion, during the full circular trajectory shown in Figure 3.10 A the angle difference remains greater than  $50^\circ$  until the final frame. In such cases, when the cell becomes more circular, the Rac1

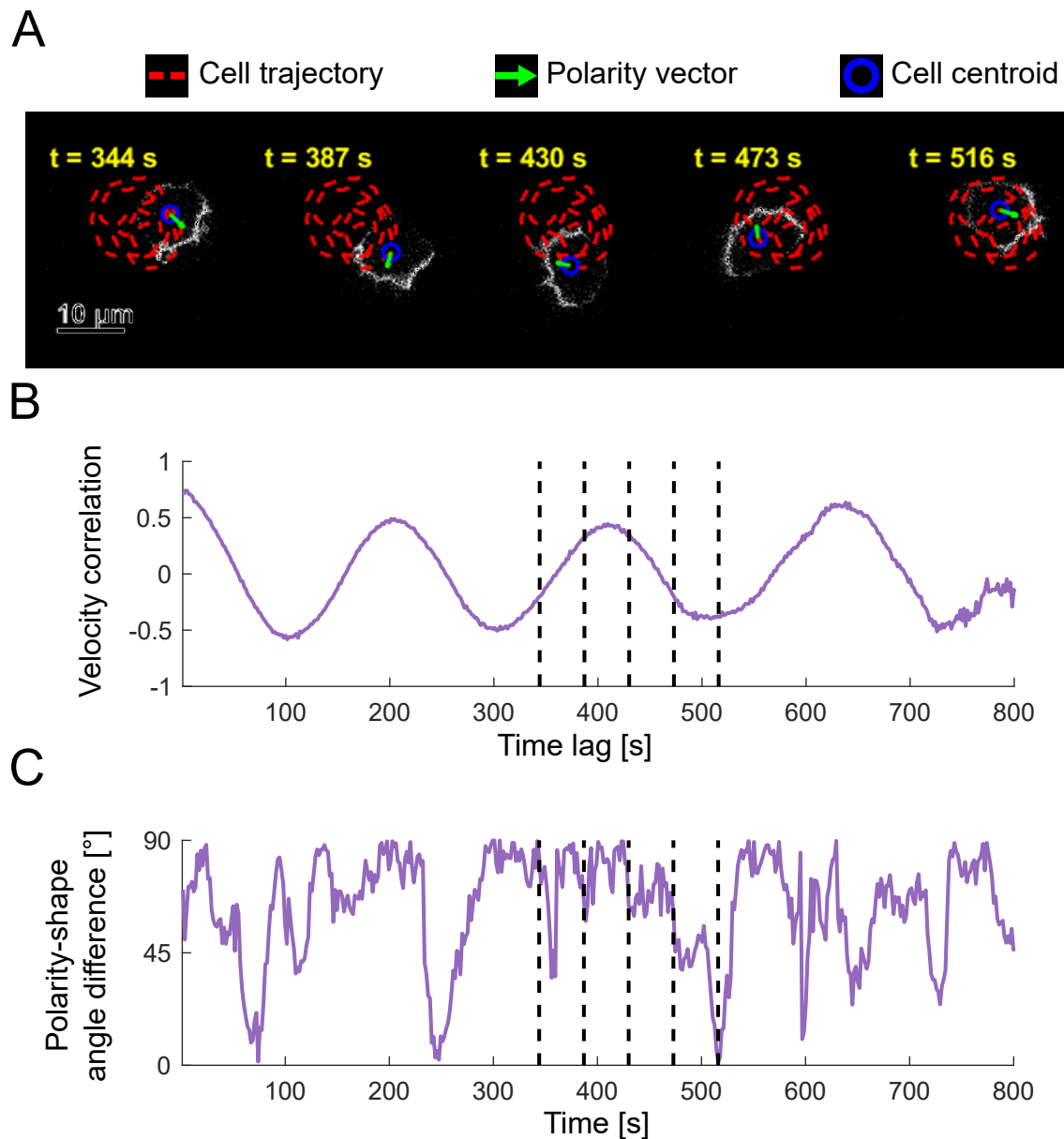


Figure 3.10: Circular runner cells. **Panel A:** Microscopy image montages showing Rac1-GTP cortex dynamics. The intensity signal of the Rac1-GTP probe is displayed in grey-scale. The red dashed line marks the cell trajectory across the entire segment, the green arrow represents the polarity vector in the given frame, and the blue circle marks the current cell centroid. The time of each snapshot, relative to the start of the classified segment, is shown in yellow above each frame. **Panel B:** Velocity autocorrelation function versus time lag. Red  $\times$  markers indicate the frames shown in the montage in Panel A. **Panel C:** Angle difference between the long shape axis and polarity vector versus time. Black dashed lines indicate the frames shown in the montage in Panel A.

patch slips slightly around the cortex, producing the jitter observed in the plot in Figure 3.10 C.

### Run-and-turn cells

The **run-and-turn** dynamics are among the most widely observed across all cells. Almost every motile cell imaged displayed similar motion at some point. However, because each cell was assigned to only one class in the classification procedure, and we required that analysed cells did not contact other cells during the segment and exhibited a sufficient signal-to-noise ratio, this class is not proportionally represented in the dataset.

Characteristic motility in this class consists of a straight run followed by a  $\sim 90^\circ$  turn, which is then followed by another straight run. This pattern is illustrated in Figure 3.11. During the run segment, the cell elongates and adopts the familiar fan shape. As it moves, the Rac1 patch spreads while the cell elongates perpendicularly to the direction of motion. Once the cell exceeds the elongation threshold and the patch has spread sufficiently, the cell slows down, the patch splits, and the two resulting patches migrate to opposite ends of the cortex at the narrow points of the elongated shape. One of these patches eventually dominates, and the cell proceeds into another straight run.

One could argue that the montage in Figure 3.11A could also be classified as an alternating runner or circular runner. However, in the **run-and-turn** class, the characteristic splitting of the patch is observed at every turn, and the secondary patch completely disappears once the cell changes direction, rather than continuing to travel around the cortex. This relationship between patch position and shape elongation can be observed in Figure 3.11C, where the cell cycles between alignment and misalignment of the shape axis and the patch.

The dynamics of the Rac1 patch appear to be related to the ratio between diffusion and advection. In Figure 3.11B, we show the Péclet number for each frame. An oscillation between turns and runs can be distinguished by following the red markers on the graph and comparing them with the montage segments in Panel A. Each time the cell stops, RD dynamics have an opportunity to dominate, as the Péclet number drops below one, which is seemingly reflected in the repositioning of the patch on the cortex.

### 3.2.2 Comparison of motile classes

With the classification established, we now compare the different classes to further distinguish their behaviours. **Run-and-turn** and **circular runner** dynamics can be difficult to distinguish, so it is useful to compare classes using statistical metrics. In Figure 3.12 we present mean velocity, polarity-shape angle difference, travel distance, and displacement. In panels A and

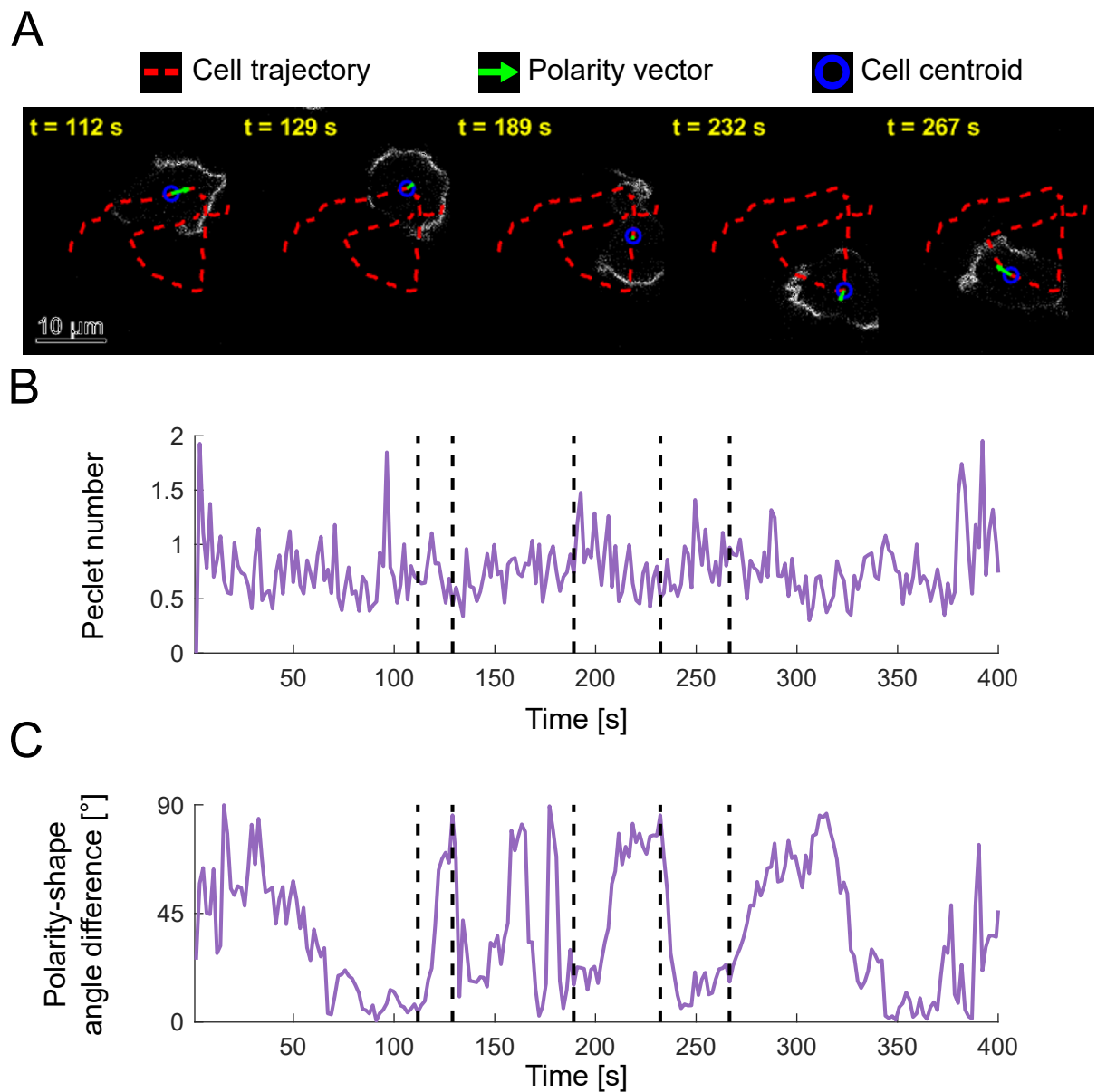


Figure 3.11: Run-and-turn cells. **Panel A:** Microscopy image montages showing Rac1-GTP cortex dynamics. The intensity signal of the Rac1-GTP probe is displayed in grey-scale. The red dashed line marks the cell trajectory across the entire segment, the green arrow represents the polarity vector in the given frame, and the blue circle marks the current cell centroid. The time of each snapshot, relative to the start of the classified segment, is shown in yellow above each frame. **Panel B:** Péclet number versus time. Black dashed lines indicate the frames shown in the montage in Panel A. **Panel C:** Angle difference between the long shape axis and polarity vector versus time. Black dashed lines indicate the frames shown in the montage in Panel A.

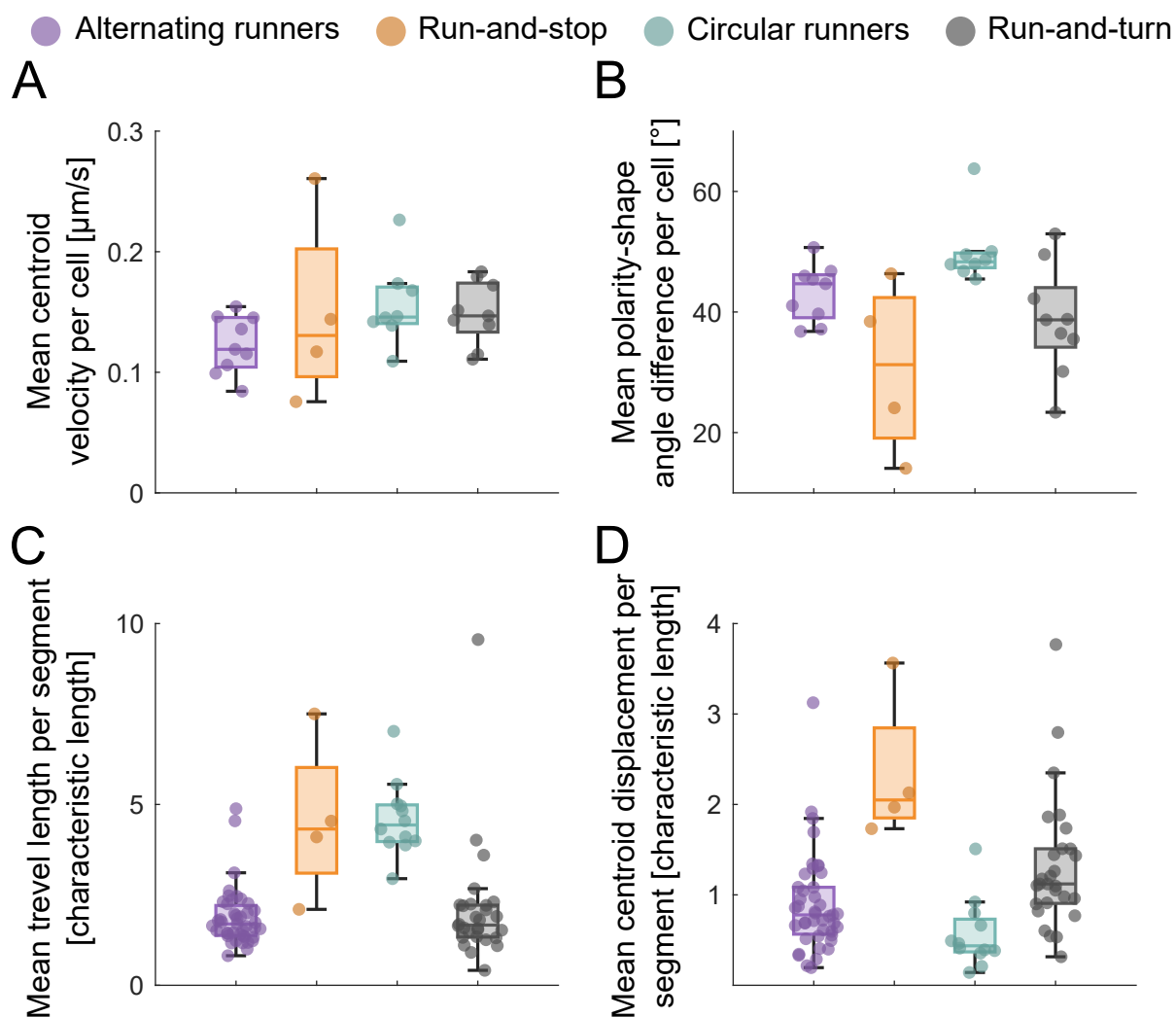


Figure 3.12: Statistics for cell classes. Every panel uses the same colour code defined at the top. For **Panels A** and **B**, the points represent the mean value across all frames in which the cell exhibited the characteristic behaviour. For **Panels C** and **D**, the points represent the mean value for a run segment. We define a run segment as a series of frames constituting one persistent run. For alternating runners, this corresponds to the motion between two successive relocations of the Rac1 patch; for run-and-stop cells, the whole segment; for circular runners, one full circle; and for run-and-turn cells, one run between two turns. **Panel A:** Mean centroid velocity per cell per class. **Panel B:** Mean angle difference between the long shape axis and polarity per cell per class. **Panel C:** Mean distance travelled during one run segment, expressed in characteristic cell lengths. **Panel D:** Mean centroid displacement during one run segment, expressed in characteristic cell lengths.

B, the metrics are presented for each classified cell across all frames in which it displayed the characteristic behaviour. In contrast, for travel distance and displacement (panels C and D), each point corresponds to a run segment as defined above. For run-and-stop and run-and-turn cells, the definition of a run segment is self-explanatory.

In Figure 3.12A, we observe that all motile cells move with similar velocities. Alternating runner cells have slightly lower mean velocities, as expected, due to frequent reversals in direction. The mean value for run-and-stop cells is likely influenced by the small number of examples in this group. Circular runners and run-and-turn cells display nearly identical mean velocities, highlighting the similarity between these two classes.

For the mean angular difference between the long shape axis and the polarity vector, we again observe the expected low values for run-and-stop cells. Furthermore, alternating runner cells have a mean angle of approximately  $45^\circ$ , consistent with the Rac1 dynamics characteristic of this class. During running segments, the Rac1 patch is aligned with the shape axis. However, when the patch shifts to a new location, part of it travels around the cortex, realigning the polarity perpendicular to the elongated shape. As discussed for circular runner cells, the cell shape in this class is predominantly elongated in a direction perpendicular to motion. Since the polarity determines the direction of motion, it is offset by slightly less than a right angle relative to the shape axis. Because the Rac1 patch leads the motion, the mean angle for circular runners ends up closer to  $50^\circ$ . In contrast, run-and-turn cells show a much smaller mean angle, indicating greater alignment between polarity and the long shape axis, with values that are also more widely scattered.

In the distance travelled during a single run segment (Figure 3.12C), we observe clear outliers in both the run-and-stop and circular runner classes. Circular runners show the highest values, as we consider only full circles in this analysis. If we wished to compare circular runners directly to run-and-turn cells, it would be more appropriate to consider a quarter of a circle, which would shift their values to a range comparable with those of the alternating runner and run-and-turn classes. The run-and-stop class, despite its small sample size, still reflects notable persistence in travel distance. Alternating runner cells, undergoing the most frequent velocity reversals, occupy the lowest range on the plot. For run-and-turn cells, however, a few outliers indicate that this class can occasionally traverse considerable distances between turns.

Lastly, we consider the displacement during a single run segment. As expected, the run-and-stop class dominates over the others. However, we also observe that run-and-turn cells cover more area than both circular and alternating runners. The latter two classes remain largely confined to a single region of the substrate, as their motility dynamics involve predominantly back-and-forth motion. Without the distance travelled and mean velocity plots, one might even

assume that circular runner cells are stationary, yet these metrics clearly demonstrate that they are not.

# Chapter 4

## Adaptation of the model to *Dictyostelium Discoideum*

With the live-cell motility of the amoeba *Dictyostelium discoideum* characterised, we now apply the model introduced in chapter 2 to this specific cell type. The main objective of this chapter is to relate simulated results to experimentally observed characteristics. After comparing *in vitro* and *in silico* cells, we conclude by proposing the mechanism by which cells shift between different motility phenotypes. To this end, we present phase diagram of motility classes as a function of the total system protein number.

### 4.1 Adaptation of reaction–diffusion system

The model presented in chapter 2 serves as a baseline for motile cells. Because the original formulation of the forces aligns well with the information summarised in section 1.4.2, we retain the same formulation of the Navier–Stokes equations and the included forces presented in section 2.1.2. The level-set formalism also remains unchanged, as it does not depend on cell type. We keep parameter ranges as close as possible to experimentally observed values or those reported in the literature. This leaves only the RD component to be adapted to *Dictyostelium*. For this purpose, we follow the rationale for RD reactions provided in (Šoštar et al., 2024) to specify the protein species included and to relate them to the experimentally observed dynamics of Rac1-GTP.

As introduced in Section 1.4.3, *Dictyostelium discoideum* possesses a simplified regulatory machinery compared with higher eukaryotes (Filić et al., 2021). This is reflected in the central role of Rac1 as the main regulator of the cytoskeleton, whose active conformation we can track

experimentally (Chapter 3). Although we could keep the protein species in the RD system abstract, it is advantageous to leverage current knowledge of signalling mechanisms to build equations grounded in known protein interactions.

As noted earlier, we implement a simplified version of the model introduced by Šoštar *et al.* (Šoštar *et al.*, 2024). Here we summarise only the essential elements, referring the reader to that work for a detailed account of all interactions and parameter choices. The main objective of the reaction–diffusion–advection (RDA) model is to capture the dynamics of Rac1, a Rho-family GTPase (Sections 1.3 and 1.4.3), whose key role in actin-cytoskeleton regulation and cell motility is well established (Jaffe & Hall, 2005; Seetharaman & Etienne-Manneville, 2020; Heasman & Ridley, 2008).

Realistic Rac1 dynamics require multiple interacting molecular species. At a minimum, one must distinguish between the inactive GDP-bound form (Rac1<sub>D</sub>) and the active GTP-bound form (Rac1<sub>T</sub>), as well as account for their different localisations on the membrane versus in the cytoplasm (Ridley, 2001; Pertz *et al.*, 2006). These coupled species constitute the core of a minimal Turing-type activator–substrate model capable of producing stationary polarity patterns (Bement *et al.*, 2015; Goryachev & Leda, 2019) (see Section 2.1.3). To include realistic temporal dynamics, at least one additional molecular component is required. Following (Šoštar *et al.*, 2024), we include a GTPase-activating protein (GAP), which accelerates the hydrolysis of GTP to GDP, thereby inactivating Rac1 (Rittinger *et al.*, 1997; Amin *et al.*, 2016). As a result, the cycling of Rac1 between cytoplasm and membrane is tightly coupled to GAP activity. The full reaction cycle represented in our model is sketched in Figure 4.1.

Thus our RDA module tracks four chemical species: cytosolic Rac1<sub>D</sub>, membrane-bound Rac1<sub>T</sub>, cytosolic GAP, and the membrane complex Rac1<sub>T</sub>–GAP. Each species diffuses freely, two-dimensionally in the bulk cytoplasm or effectively one-dimensionally along the membrane cortex. The reaction cycle proceeds as follows. Cytosolic Rac1<sub>D</sub> attaches to the membrane and, in the same step, exchanges GDP for GTP to become Rac1<sub>T</sub>. *In vivo* this two-step process (membrane recruitment followed by activation) is mediated by guanine-nucleotide-exchange factors (GEFs) (Hart *et al.*, 1991; Cook *et al.*, 2014). We lump the two events into a single instantaneous reaction. This simplification is justified by observations that most membrane-bound Rac1 is indeed in the active, GTP-loaded state (Golding *et al.*, 2019) and that Rac1 activation on the membrane displays strong autocatalytic behaviour (Goryachev & Leda, 2019). Consequently, Rac1<sub>D</sub> is assumed to reside exclusively in the cytoplasm, whereas Rac1<sub>T</sub> is confined to the membrane. The predominance of inactive Rac1 in the cytosol is supported by its high-affinity binding to RhoGDI, which sequesters Rac1 and suppresses spontaneous activation (Garcia-Mata *et al.*, 2011) (see Section 1.3.1). Next, membrane-bound Rac1<sub>T</sub> can bind

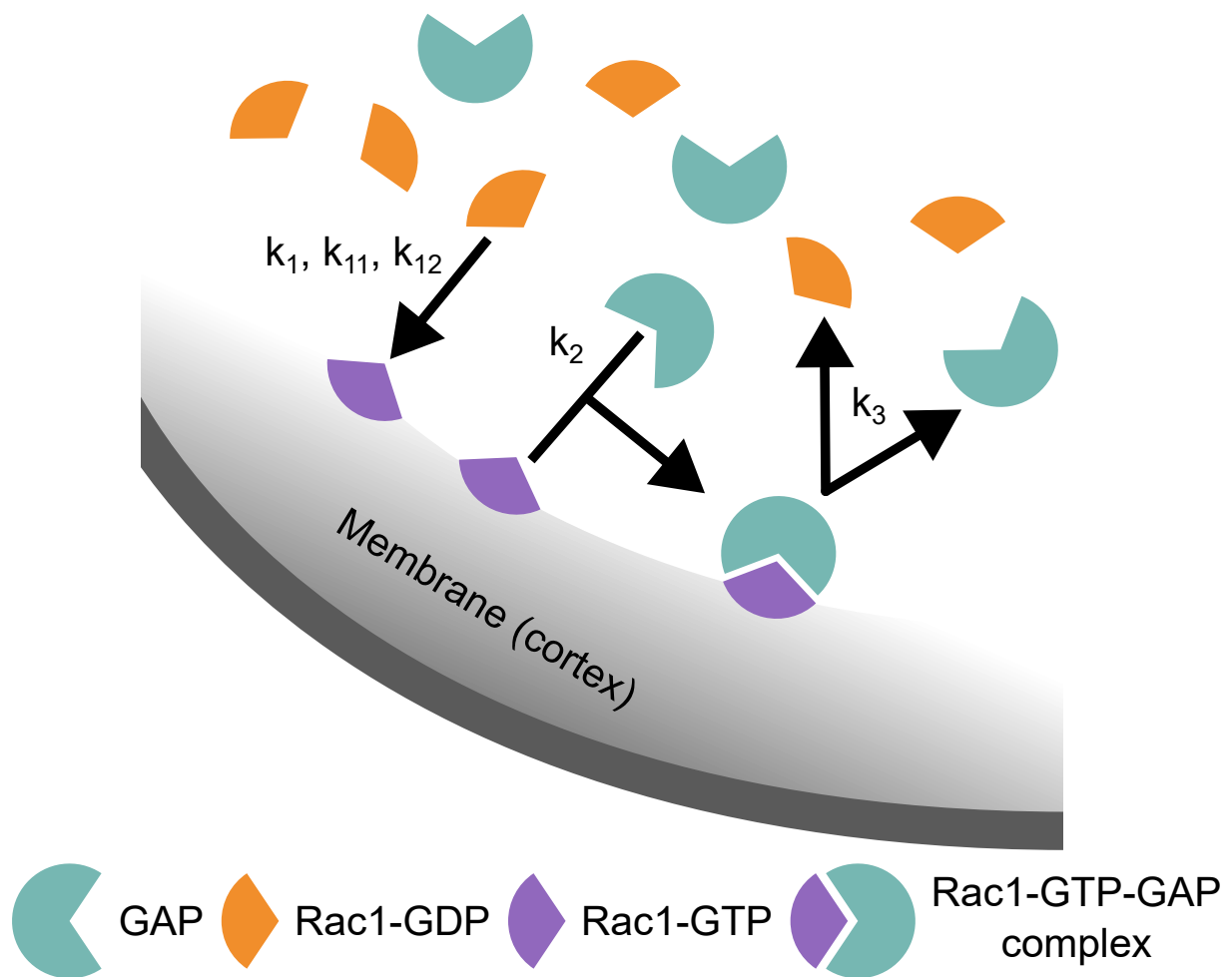


Figure 4.1: Schematic of Rac1 cycling and interactions with GAP. Marker legend is located below the schematic. Arrows indicate the direction of the reaction with governing constants for that reaction annotated beside them. Cytosolic Rac1<sub>D</sub> binds to the membrane and exchanges GDP for GTP to become Rac1<sub>T</sub>. Membrane-bound Rac1<sub>T</sub> can form a complex with cytosolic GAP, GAP–Rac1<sub>T</sub>. The cycle ends when this complex dissociates, releasing GAP and Rac1<sub>D</sub> back into the cytoplasm.

cytosolic GAP to form a Rac1<sub>T</sub>-GAP complex. GAP accelerates the intrinsic GTP hydrolysis rate of Rac1, effectively terminating its signalling activity (Amin et al., 2016). In our cycle, this catalytic step is followed by dissociation of the complex and release of both proteins into the cytoplasm, with Rac1 returning in its inactive GDP-bound form, a sequence consistent with live-cell measurements of Rac1 inactivation dynamics (Johnson et al., 2009).

The reactions are written with the abundance of each species represented by a surface or bulk concentration  $C(x, y, t)$ . The net reaction terms entering the RDA equations are:

$$R_{\text{Rac1}_D} = k_3 C_{\text{Rac1}_T\text{-GAP}} - C_{\text{Rac1}_D} \left( 1 - \frac{C_{\text{Rac1}_T}}{C_{\text{Rac1}_T}^{\text{MAX}}} \right) (k_1 + k_{11} C_{\text{Rac1}_T} + k_{12} C_{\text{Rac1}_T\text{-GAP}}), \quad (4.1a)$$

$$R_{\text{GAP}} = k_3 C_{\text{Rac1}_T\text{-GAP}} - k_2 C_{\text{Rac1}_T} C_{\text{GAP}}, \quad (4.1b)$$

$$R_{\text{Rac1}_T} = -k_2 C_{\text{Rac1}_T} C_{\text{GAP}} + C_{\text{Rac1}_D} \left( 1 - \frac{C_{\text{Rac1}_T}}{C_{\text{Rac1}_T}^{\text{MAX}}} \right) (k_1 + k_{11} C_{\text{Rac1}_T} + k_{12} C_{\text{Rac1}_T\text{-GAP}}), \quad (4.1c)$$

$$R_{\text{Rac1}_T\text{-GAP}} = k_2 C_{\text{Rac1}_T} C_{\text{GAP}} - k_3 C_{\text{Rac1}_T\text{-GAP}}. \quad (4.1d)$$

Here  $k_1$  is the basal rate at which cytosolic Rac1<sub>D</sub> binds and activates on the membrane.  $k_{11}$  and  $k_{12}$  quantify co-operative autocatalysis mediated, respectively, by membrane Rac1<sub>T</sub> and by the transient Rac1<sub>T</sub>-GAP complex. The positive feedback provided by  $k_{11}$  supplies the classical activator-self-activation mechanism of a Turing-type systems (Turing, 1952; Goryachev & Leda, 2019). The additional, delayed feedback through  $k_{12}$  (Rac1 that is momentarily inactive within the Rac1<sub>T</sub>-GAP complex still promotes further Rac1 recruitment) has been shown to broaden the parameter range that supports pattern formation in mass-conserved GTPase models (Otsuji et al., 2007; Mori et al., 2008). Complex formation and dissociation are governed by  $k_2$  and  $k_3$ , respectively. Finally, the factor  $(1 - C_{\text{Rac1}_T}/C_{\text{Rac1}_T}^{\text{MAX}})$  prevents Rac1<sub>T</sub> from exceeding a steric saturation limit on the membrane (Douglass & Vale, 2005; Mori et al., 2008).

The full evolution equation presented in Section 2.1.3 (see Eq. (2.13)) remains unchanged. Thus, we have adapted our RDA system to incorporate known signalling mechanisms that orchestrate cell motility in *Dictyostelium discoideum*. With this adaptation in place, we proceed with discussing relations between phenotype behaviour observed experimentally and in simulations.

## 4.2 Comparison of live and simulated cells

Our model reproduces all four motile classes observed experimentally. Furthermore, we have showed how varying coupling strengths can facilitate different motility phenotypes, with lone

exception being the run-and-stop class. As noted earlier, reproducing this class requires initialising the system with a total protein level that supports neither rotation nor oscillation. Such cells would move transiently due to the initial concentration profile and then stop once RD dynamics shut down.

We can nevertheless compare run-and-stop *shapes* to the persistent-runner class, as the run parts of both phenotypes should not differ. From figure 3.9, these cells span fan-like to stadium-like geometries: they start fan-shaped and elongate just before stopping, resembling a stadium. Both shapes occur within the simulated persistent-runner class (figure 2.14). By contrast, the dumbbell shape, which appears in simulations at large  $k_C$  without surface-tension variation, is rare in experiments. This supports the view that live cells exhibit a front-rear tension asymmetry, with lower frontal tension favouring fan-like shapes in *Dictyostelium*.

In both experiments and simulations, alternating runners emerge naturally from oscillatory dynamics in stationary cells. The time traces of elongation (figures 3.8 and 2.15) show repeated cycles: when the Rac1<sub>T</sub> patch shifts, cells transiently round up, then elongate during the run segments. In our simulations, alternating runners are comparatively rare on the rotation-seeded phase diagram (figure 2.18A) and appear mainly for  $k_\sigma > 0$ . We propose that, in the simulations, the initial patch asymmetry must be symmetrised by constrictive, surface tension-driven flow. On the oscillation-initiated diagram (figure 2.18B), alternating runners are more common, again mostly at  $k_\sigma > 0$ , which stabilises oscillatory patterns in stationary cells (figure 2.11F). For  $k_\sigma < 0$ , the induced flow suppresses alternating patch dynamics and favours persistent runs.

As with the higher incidence of alternating runners under oscillation initial conditions, circular runners appear only in simulations initiated from rotation profile. This again points to the importance of initial patch asymmetry, which could arise stochastically in live cells. In simulations (figure 2.16), we observe two circular-running modes: (i) a fan-shaped cell turning with a large radius and (ii) an oval/elliptical or stadium-like cell turning with a small radius comparable to the short semi-axis. Both modes reproduce the experimental velocity autocorrelation (figures 2.16B and 3.10B). Although figure 3.10C shows a wide distribution of shape-polarity angles, the mean is about  $50^\circ$  (figure 3.12), indicating that experimental circular runners more closely match the first, fan-shaped mode. The simulated shape differences again point to lower frontal surface tension in live cells.

The last class to compare is the run-and-turn cells. We have argued that this class reflects a geometry-mediated effect on the RDA system. In both experiment and simulation, the cell starts a run with high polarity aligned to the long axis. As speed increases, the Péclet number rises and the cell elongates perpendicular to motion. This spreads the patch, reducing polarity magnitude, speed, and thus the Péclet number. Despite noisier experimental metrics, this sequence is evident

in figures 3.11 and 2.17, supporting the conclusion that geometry-mediated modulation of RDA dynamics occurs in live cells, with our model providing a mechanistic explanation.

After the comparison of experimentally observed phenotypes with the simulated ones, we conclude that our model captures the main dynamics of the vegetative *Dictyostelium* cells. However, we have presented the comparison in terms of coupling strengths, which is instructive but not necessarily biologically grounded. To acknowledge this we present much more biologically feasible way cells can switch between different motile classes.

## 4.3 How cells shift between behavioural phenotypes

In Chapter 2, we have delineated the mathematical formulation of the model, present the properties of RD system in terms of the effects of geometry and transport and introduced the flows originating from two coupling forces within our model. We showed how the variation of these two forces, coupled to the concentration of the activator, can explain different motile behaviours within our model, which we related to the experimentally observed ones. However, we have neglected, until now, how total number of protein molecules inside the system affects the solutions of the fully coupled model. In the rest of this section we present how the system responds to different number of protein molecules inside the system and relate this to the biological implications.

### 4.3.1 Protein variation on stationary cell

Within the mass-conserved reaction–diffusion (MCRD) theory, one of the main parameters that determine the possible solutions the system can exhibit is the total number of protein molecules within such system (Brauns et al., 2020). To illustrate this we have initiated simulations with initial rotation concentration profile scaled in a way such that the total number of proteins in the bulk changes. This way we initiate system with same  $\text{Rac1}_T$  and  $\text{Rac1}_T\text{-GAP}$  profiles on the cortex while setting desired total protein number by tuning the way more uniform bulk profile. The results of these simulations are presented on phase diagram in Figure 4.2.

With the coupling forces disabled, and all the other parameters held fixed the geometry of the cell stays circular. On such domains three different canonical RD solutions can occur (see Section 2.3.1). With the cortex diffusion set to values in Table 5.14 only two nonuniform solutions are possible: rotation and oscillation pattern. First thing to note here is that oscillation pattern can emerge from initial rotation concentration profile, given the right protein number combination.

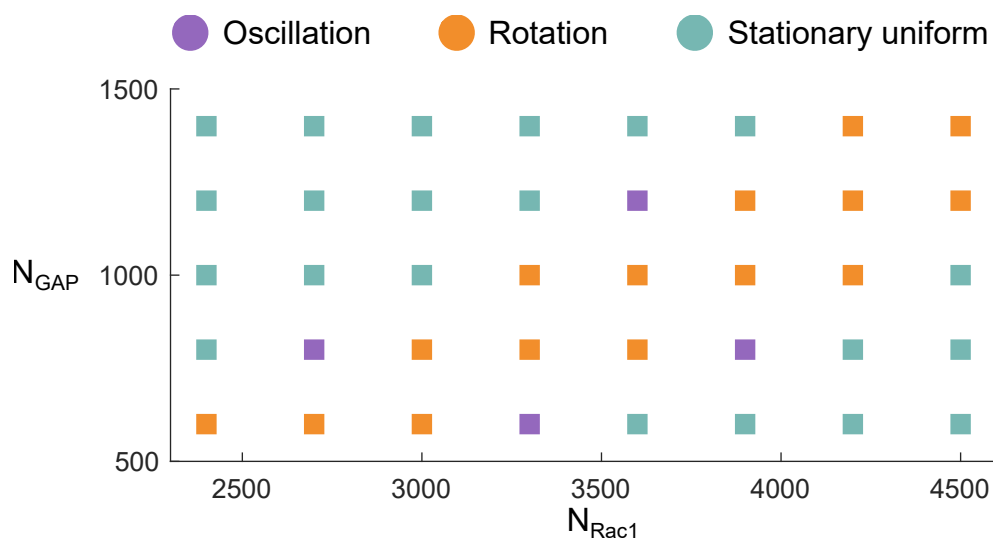


Figure 4.2: Phase diagram as a function of total number of protein molecules in the system. Simulations have been initiated without coupling forces ( $k_C = 0$  and  $k_\sigma = 0$ ), with rotation initial condition on a circular cell. Horizontal axis represent number of Rac1 molecules and the vertical represents number of GAP molecules in the system. Each point presents a pattern at 1500 s of simulation time. For full information about the parameters of the simulation see Table 5.14.

Phase diagram in Figure 4.2 shows how nonuniform solutions emerge only if the ratio of molecule numbers between Rac1 and GAP is constant (the diagonal patch in the diagram). Furthermore, oscillation pattern is constrained to the boundaries of the diagonal nonuniform solutions patch. It should be noted here that the oscillation patterns on the opposite sides of the patch differ a bit in shape of the  $\text{Rac1}_T$  profile on the cortex and its dynamics. Across all simulation presented in the diagram, the main difference between solutions labelled as the specific pattern, is the height of the cortex concentration profiles. Apart from the height the period of oscillations and rotations can change as well.

In simulations labelled as stationary uniform in the Figure 4.2, the dynamics died down through the first 1500 s of simulation time and the resulting concentration profiles were uniform and time independent for the rest of the simulation. When the coupling forces are disabled there are no advective flows influencing the dynamics of the system. From the effects of the flow on the dynamics of the system presented in Section 2.4.1 we expect that the inclusion of these flows will stabilize the system.

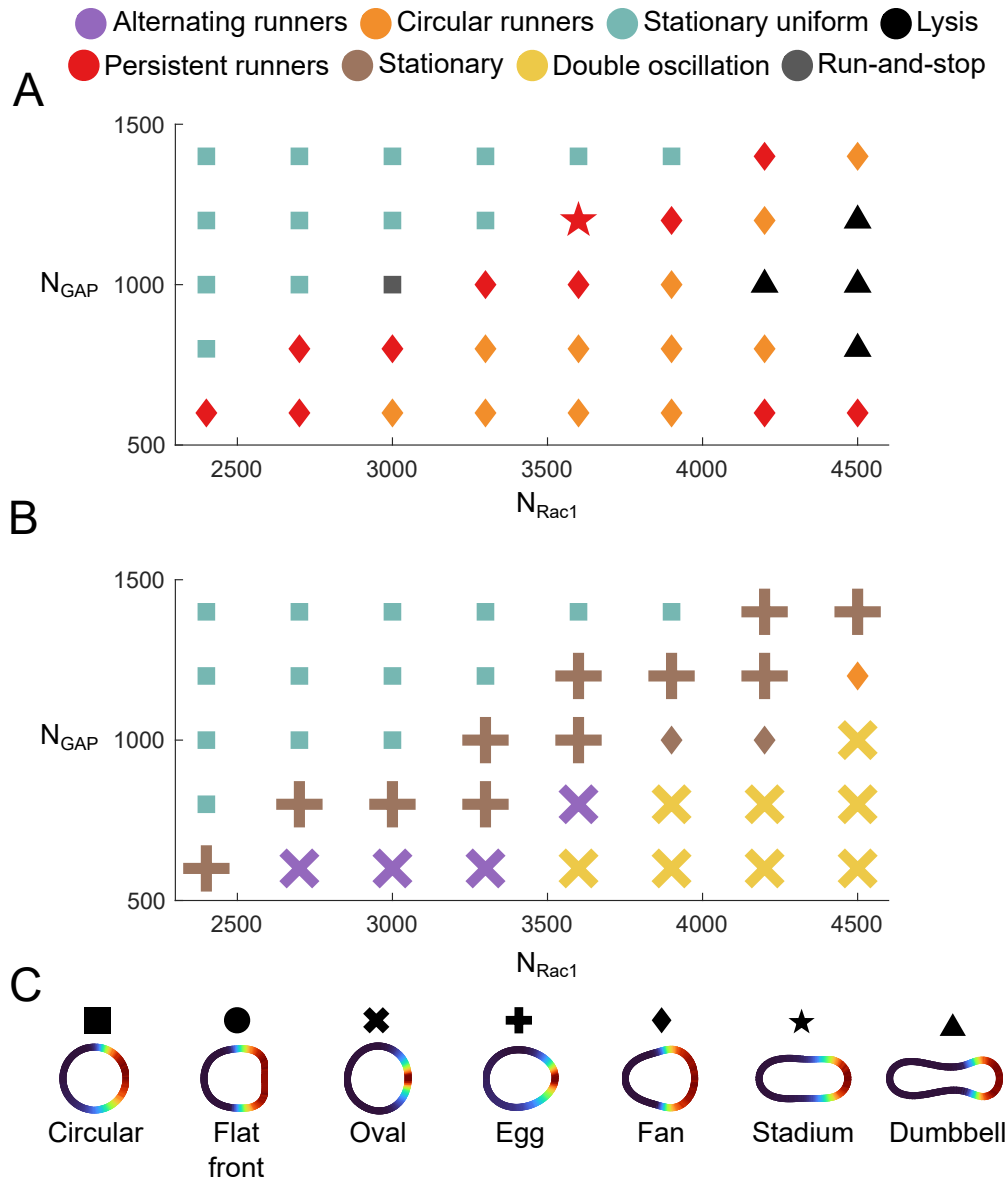


Figure 4.3: Phase diagrams as a function of total number of protein molecules in the system. Simulations have been initiated with rotation initial condition on a circular cell. **Panel A:** Phase diagram for simulations initiated with negative surface tension coupling  $k_{\sigma} = -0.03$  and protrusive coupling  $k_C = 0.03$ . Horizontal axis represent number of Rac1 molecules and the vertical represents number of GAP molecules in the system. Each point presents a pattern at 1000 s of simulation time. Each marker denotes a simulated parameter pair; marker *colour* encodes the resulting limit-cycle class and marker *shape* encodes the characteristic cell shape. **Panel B:** As in Panel A, but for simulations initiated with  $k_{\sigma} = 0.03$  and  $k_C = 0.03$ . **Panel C:** Legend linking marker shapes to representative cell contours. Contours are coloured by activator concentration along the cortex to indicate patch position. The contour shown for each class is a representative shape. For full information about the parameters of the simulation see Table 5.15.

### 4.3.2 Protein variation with coupling forces

To assess the effects of coupling-induced flows on the protein distribution, we ran two batches of simulations with nonzero coupling strengths: one with negative coupling (Figure 4.3A) and one with positive coupling (Figure 4.3B). Apart from the coupling terms, the initial conditions and all other parameters in Figure 4.3 match those in Figure 4.2, enabling a direct comparison of the emergent effects of the coupling forces.

The first observation when comparing Figures 4.2 and 4.3 is the expansion of non-uniform solutions into the bottom-right corner, reflecting the stabilizing influence of the coupling-induced flows. Regions of molecule-number phase space that were inaccessible under static geometry now transform into distinct motile classes. A second, previously unreported outcome is the emergence of a solution type we term **Lysis**.

The **Lysis** state denotes a limit-cycle outcome in which the patch splits to opposite sides of the cell, dragging the cortex in opposing directions. The cell adopts a dumbbell shape with two active cortex regions. As the cell stretches, the height of the patches increases, strengthening both protrusive and surface tension coupled forces. Once the concentration exceeds a threshold, the effective surface tension becomes negative, ruffling the surface. At that point the cortex fails numerically because the level-set function cannot adapt to the prescribed shape. This could likely be remedied by higher spatial resolution, which is not available in our current implementation. We therefore note this result here and do not discuss it further.

Turning to the motile classes introduced in Section 2.4.2 and shown in the diagrams in Figure 4.2, panel A indicates that with negative surface-tension coupling ( $k_{\sigma} < 0$ ) most emergent solutions are circular-runner or persistent-runner phenotypes. As noted earlier, an initial asymmetry in the patch profile is required to initiate circular runs, which justifies our choice of a rotational initial concentration pattern.

These two phenotypes are consistent with their known properties. However, in the top-left corner of the diagram, a simulation labeled stationary uniform in Figure 4.2 becomes a run-and-stop cell. Most cells in that corner initiate motion, but the dynamics decay before substantial displacement occurs. Under our classification procedure, the only case not labelled stationary is precisely this cell: it begins to move in a straight line, its trajectory briefly extending beyond the cell contour, before the dynamics die out and the cell returns to a circular, uniform, stationary state.

Similarly, in Figure 4.3B we observe the extension of non-uniform solutions to cover the entire bottom-right corner. Notably, all cells that showed no dynamics in the stationary simulations (Figure 4.2) now adopt the double-oscillation phenotype. This is consistent with the effect of positive surface-tension coupling on the emergence and stability of oscillatory patterns. As noted

earlier, the underlying dynamics of single- and two-patch oscillations are inherently similar and differ primarily in the number of patches.

The remaining cells in Figure 4.3B either remain stationary with cortical oscillations or display alternating-runner behaviour. Only a single case with positive surface-tension coupling ( $k_\sigma > 0$ ) retains a circular-runner trajectory with the characteristic fan shape. In contrast to the negative-coupling case, the top-left cells here do not change class relative to the stationary simulations.

Regarding biological implications, the couplings expand the non-stationary solution space, indicating stabilizing effects of the fully coupled system. This suggests why cells may employ reaction–diffusion–advection dynamics for motility signalling: it provides a robust framework that supports a wide range of locomotion modes. With all other properties held fixed, our model suggests that cells can shift between phenotypes simply by adjusting the expression levels of the relevant proteins.

This also helps explain why cells from the same sample can exhibit diverse behaviours despite minimal genetic or environmental differences. For example, the run-and-stop behaviour observed experimentally (see Section 3.2.1) may represent a transient phase between phenotypes as total protein numbers change. Once the molecular ratios again support the dynamics, stochastic noise or thermal fluctuations in a biological context could restart the system.

To conclude, viewing the system through the lens of total protein number provides a direct biological explanation for the variety of experimentally observed motile phenotypes. It also highlights emergent properties of the fully coupled system that are inaccessible without including the flows. This justifies our modelling approach and reveals novel insights into the vegetative, non-stimulated behaviour of living cells.

# Chapter 5

## Conclusion and outlook

### 5.1 Conclusion

We close this thesis by returning to the task set out at the start of the Introduction. The model developed here reproduces the principal experimentally observed motility and signalling patterns and offers a compact mechanistic account of how they arise. In doing so, it clarifies how flow and shape can both moderate and amplify reaction–diffusion dynamics, and it delineates a minimal set of reaction–shape–flow couplings sufficient to simulate motile cells efficiently and realistically.

This work advances our understanding of cell motility by identifying the minimal interactions required to reproduce experimentally observed behaviour. Because the model is grounded in current knowledge of cytoskeletal mechanics and signalling dynamics, it is readily adaptable to non-amoeboid modes of motility by tuning parameter values or modifying coupling mechanisms. We hope that this thesis provides a stepping stone toward more complete, predictive models of cellular locomotion.

### 5.2 Summary

In this thesis, we presented a minimal mechanochemical framework for modelling cell motility. Migration is a fundamental cellular process that integrates signalling-protein dynamics, evolving morphology, and cytosolic and membrane flows. As introduced in Chapter 1, small GTPases organise front–rear polarity and stimulate cytoskeletal components that drive directed motion. Although crawling phenotypes vary across eukaryotes, most of the underlying principles are shared.

This provided the groundwork for our model. We coupled signalling dynamics to cell shape and intracellular flows to capture the essence of motility mechanics. A key insight is that a retracting rear and protrusive front can be modelled by introducing spatially variable surface tension along the cortex, in addition to the normal protrusive force commonly used in prior models.

These two couplings (protrusive and surface tension) induce flows in the cytoplasm and along the cortex, which in turn modulate reaction–diffusion (RD) dynamics. We first characterised the canonical RD behaviours admitted by our model in a stationary domain, then analysed how the induced flows reshape these patterns. Our results indicate that RD dynamics in this setting are strongly influenced by advective coupling.

To validate the model, we imaged *in vitro* amoebae (*Dictyostelium discoideum*), known for their high motility. These cells possess simplified cytoskeletal and signalling machinery: motility is governed predominantly by the actomyosin cortex, microtubules play primarily a scaffolding role, canonical intermediate filaments are absent and majority of the motility signalling dynamics relies on only one GTPase called Rac1. This made *Dictyostelium* an ideal testbed for our minimal model of cellular locomotion.

From experimentally observed behaviours, we proposed a taxonomy of vegetative-cell motility classes: stationary, run-and-stop, alternating runners, circular runners, and run-and-turn. Each class was further characterised using quantitative metrics of shape, Rac1 GTPase dynamics, and trajectory features. We found that a compact set of four class-averaged metrics suffices to distinguish among these behaviours.

All four motile classes observed experimentally were reproduced by our simulations (alternating runners, circular runners and run-and-turn cells). Furthermore, persistent runners also appeared as the solution of the model, however this class resembles chemotactic locomotion of *Dictyostelium* and wasn't observed in our vegetative cells. We mapped how these classes depend on the ratios of protrusive and surface-tension couplings and showed how these couplings select characteristic cell geometries. The simulation results align well with experiments, supporting the conclusion that both couplings must act alongside RD and flow dynamics to recover the observed behaviours.

The main conclusion aligns with recent work by Chen *et al.* Chen et al., 2024, which argues that motility regimes can be understood through intracellular energy partitioning. In our framework, simulated classes differ in how energy is distributed among RD dynamics, advection/flows, and geometry-dependent mechanics. When RD dominates, cells remain largely stationary. As coupling strengths increase, motile classes emerge, initially driven by flow-modified RD patterns and, at higher couplings, increasingly shaped by geometric constraints.

This perspective is consistent with the idea that the balance of energy among RD, shape, and advection determines motile behaviour.

In summary, this thesis advances state-of-the-art modelling by introducing variable cortex tension coupled to signalling dynamics. This approach enabled us to simulate and interpret experimentally observed behaviours of *Dictyostelium discoideum*, thereby validating the model. We present these findings with the hope that subsequent studies of cell motility will adopt and extend this framework.

## 5.3 Outlook

With the results assembled and the conclusions drawn, both the model, and especially its implementation, leave ample room for improvement. Throughout this work we assumed a spatially uniform viscosity, an approximation unlikely to hold in live cells and one that could substantially alter the induced flows. A full treatment of dynamics arising from spatially variable surface tension likewise proved too time consuming for the time frame of this thesis. In addition, the current code cannot yet access the temporal and spatial scales required to unambiguously identify asymptotic limit cycles or to explore a substantially broader region of parameter space.

In its current form, the model is best suited to amoeboid motility. Many higher eukaryotes possess more complex cytoskeletal machinery that must be addressed to simulate motility more broadly. For example, myosin-induced contraction mediated by stress fibres should be modelled as an active contractile vector field, which is not yet included. The application to *Dictyostelium discoideum* presented here is simpler, as these cells lack canonical stress fibres and reorganise regions of higher and lower tension more rapidly than in more complex cells.

Even though the level-set formalism allows highly complex membrane geometries, the spatial resolution required to capture them lies beyond the scope of the current implementation, as the resulting simulation times would be too long. With higher resolution, one could simulate the ruffling effects associated with lower cortical tension observed experimentally in *Dictyostelium*. Furthermore, extending the simulation domain would mitigate periodic-boundary effects and could reveal new dynamics; at present, however, such runs are computationally prohibitive.

Recognising these limitations, we nonetheless view the central result positively: variable surface tension, together with cytoplasmic recirculation, can reproduce experimentally observed motility characteristics within a minimal framework. Our intention is to address the outstanding issues—introducing heterogeneous (and potentially anisotropic) viscosity, completing the implementation of surface tension–driven dynamics, and extending the numerics to longer simulations and wider parameter sweeps, to further clarify the underlying mechanisms. We conclude

with the hope that these ideas will seed next-generation models and tools, and that continued methodological advances will make the most ambitious explorations feasible.

# Appendix

Here we list the parameters used to obtain simulation results presented in chapters 2 and 4. In table 5.1 we present the parameter values which were held fixed for all of the simulations. Next

Table 5.1: Fixed parameters used in all of the simulations

Parameter	Symbol	Value
Grid spacing	$\Delta x, \Delta y$	0.12
Time step	$\Delta t$	$5 \times 10^{-5}$
Gradient threshold	gCO	$1 \times 10^{-3}$
Level-set tolerance	lsTOL	$1 \times 10^{-3}$
Pressure tolerance	pTOL	$1 \times 10^{-5}$
Maximum Jacobi iterations	maxIter	$6 \times 10^4$
Interface thickness	$\epsilon$	1.2
Viscosity (kinematic)	$\nu$	1
Density	$\rho$	1
Dissipation coefficient	$\beta$	1
Area-constraint coefficient	$\alpha$	0.1
Initial cell area	$A_0$	120
Initial cell radius	$r_0 (= \sqrt{A_0/\pi})$	6.21
<b>Reaction rates</b>		
Activator attachment	$k_1$	0.19
Activator autocatalytic attachment	$k_{11}$	0.027
Catalytic complex attachment	$k_{12}$	0.0045
Complex assoc.	$k_2$	4.5
Complex dissoc.	$k_3$	0.15
Activator saturation conc.	$C_a^{\max}$	200

we present parameters specific for each simulation presented in table 5.2-5.13. We display all of the remaining parameters used for each of the figures.

Table 5.2: Parameters used in the simulations presented in figure 2.7

Parameter	Symbol	Value
<b>Figure 2.7 oscillation</b>		
Domain size	$L_x, L_y$	18
Resting surface tension	$\sigma_0$	5
Surface tension coupling	$k_\sigma$	0
Protrusive-force coupling	$k_C$	0
Diffusion substrate 1	$D_{s_1}$	34
Diffusion activator	$D_a$	0.3
Diffusion substrate 2	$D_{s_2}$	8
Diffusion complex	$D_c$	0.1
Number of molecules $s_1 + a + c$	$N_1$	2400
Number molecules $s_2 + c$	$N_2$	700
<b>Figure 2.7 rotation</b>		
Domain size	$L_x, L_y$	18
Resting surface tension	$\sigma_0$	5
Surface tension coupling	$k_\sigma$	0
Protrusive-force coupling	$k_C$	0
Diffusion substrate 1	$D_{s_1}$	34
Diffusion activator	$D_a$	0.3
Diffusion substrate 2	$D_{s_2}$	8
Diffusion complex	$D_c$	0.1
Number of molecules $s_1 + a + c$	$N_1$	4000
Number molecules $s_2 + c$	$N_2$	1200
<b>Figure 2.7 static polarization</b>		
Domain size	$L_x, L_y$	18
Resting surface tension	$\sigma_0$	5
Surface tension coupling	$k_\sigma$	0
Protrusive-force coupling	$k_C$	0
Diffusion substrate 1	$D_{s_1}$	34
Diffusion activator	$D_a$	0.3
Diffusion substrate 2	$D_{s_2}$	8
Diffusion complex	$D_c$	0.6
Number of molecules $s_1 + a + c$	$N_1$	2400
Number molecules $s_2 + c$	$N_2$	700

Table 5.3: Parameters used in the simulations presented in figure 2.8

Parameter	Symbol	Value
<b>Figure 2.8 oscillation</b>		
Domain size	$L_x, L_y$	18
Resting surface tension	$\sigma_0$	5
Surface tension coupling	$k_\sigma$	0
Protrusive-force coupling	$k_C$	0
Diffusion substrate 1	$D_{s_1}$	34
Diffusion activator	$D_a$	0.3
Diffusion substrate 2	$D_{s_2}$	8
Diffusion complex	$D_c$	0.1
Number of molecules $s_1 + a + c$	$N_1$	2300
Number molecules $s_2 + c$	$N_2$	700
<b>Figure 2.8 rotation</b>		
Domain size	$L_x, L_y$	18
Resting surface tension	$\sigma_0$	5
Surface tension coupling	$k_\sigma$	0
Protrusive-force coupling	$k_C$	0
Diffusion substrate 1	$D_{s_1}$	34
Diffusion activator	$D_a$	0.3
Diffusion substrate 2	$D_{s_2}$	8
Diffusion complex	$D_c$	0.1
Number of molecules $s_1 + a + c$	$N_1$	4000
Number molecules $s_2 + c$	$N_2$	1200
<b>Figure 2.8 static polarization</b>		
Domain size	$L_x, L_y$	18
Resting surface tension	$\sigma_0$	5
Surface tension coupling	$k_\sigma$	0
Protrusive-force coupling	$k_C$	0
Diffusion substrate 1	$D_{s_1}$	34
Diffusion activator	$D_a$	0.3
Diffusion substrate 2	$D_{s_2}$	8
Diffusion complex	$D_c$	0.6
Number of molecules $s_1 + a + c$	$N_1$	2300
Number molecules $s_2 + c$	$N_2$	700

Table 5.4: Parameters used in the simulations presented in figure 2.9

Parameter	Symbol	Value
<b>Figure 2.9 A</b>		
Domain size	$L_x, L_y$	18
Resting surface tension	$\sigma_0$	5
Surface tension coupling	$k_\sigma$	0
Protrusive-force coupling	$k_C$	0
Diffusion substrate 1	$D_{s_1}$	34
Diffusion activator	$D_a$	0.01-1
Diffusion substrate 2	$D_{s_2}$	8
Diffusion complex	$D_c$	0.01-1
Number of molecules $s_1 + a + c$	$N_1$	4000
Number molecules $s_2 + c$	$N_2$	1200
<b>Figure 2.9 B</b>		
Domain size	$L_x, L_y$	18
Resting surface tension	$\sigma_0$	5
Surface tension coupling	$k_\sigma$	0
Protrusive-force coupling	$k_C$	0
Diffusion substrate 1	$D_{s_1}$	34
Diffusion activator	$D_a$	0.01-1
Diffusion substrate 2	$D_{s_2}$	8
Diffusion complex	$D_c$	0.01-1
Number of molecules $s_1 + a + c$	$N_1$	2300
Number molecules $s_2 + c$	$N_2$	700

Table 5.5: Parameters used in the simulations presented in figure 2.10

Parameter	Symbol	Value
<b>Figure 2.10</b>		
Domain size	$L_x, L_y$	18
Resting surface tension	$\sigma_0$	5
Surface tension coupling	$k_\sigma$	0
Protrusive-force coupling	$k_C$	0.04
Diffusion substrate 1	$D_{s_1}$	34
Diffusion activator	$D_a$	0.03
Diffusion substrate 2	$D_{s_2}$	8
Diffusion complex	$D_c$	0.01
Number of molecules $s_1 + a + c$	$N_1$	2400
Number molecules $s_2 + c$	$N_2$	700

Table 5.6: Parameters used in the simulations presented in figure 2.11

Parameter	Symbol	Value
<b>Figure 2.11 constant parameters</b>		
Domain size	$L_x, L_y$	28
Resting surface tension	$\sigma_0$	5
Protrusive-force coupling	$k_C$	0
Diffusion substrate 1	$D_{s_1}$	34
Diffusion activator	$D_a$	0.03
Diffusion substrate 2	$D_{s_2}$	8
Diffusion complex	$D_c$	0.01
<b>Figure 2.11 A and B</b>		
Surface tension coupling	$k_\sigma$	0.02
Number of molecules $s_1 + a + c$	$N_1$	2400
Number molecules $s_2 + c$	$N_2$	700
<b>Figure 2.11 C and D</b>		
Surface tension coupling	$k_\sigma$	-0.02
Number of molecules $s_1 + a + c$	$N_1$	2400
Number molecules $s_2 + c$	$N_2$	700
<b>Figure 2.11 E</b>		
Surface tension coupling	$k_\sigma$	-0.02 or 0.02
Number of molecules $s_1 + a + c$	$N_1$	2400
Number molecules $s_2 + c$	$N_2$	700
<b>Figure 2.11 F</b>		
Surface tension coupling	$k_\sigma$	-0.02 - 0.05
Protrusive-force coupling	$k_C$	0
Number of molecules $s_1 + a + c$	$N_1$	2400 or 4000
Number molecules $s_2 + c$	$N_2$	700 or 1200

Table 5.7: Parameters used in the simulations presented in figure 2.12

Parameter	Symbol	Value
<b>Figure 2.12 rotation</b>		
Domain size	$L_x, L_y$	28
Resting surface tension	$\sigma_0$	5
Surface tension coupling	$k_\sigma$	0.02
Protrusive-force coupling	$k_C$	0.02
Diffusion substrate 1	$D_{s_1}$	34
Diffusion activator	$D_a$	0.3
Diffusion substrate 2	$D_{s_2}$	8
Diffusion complex	$D_c$	0.1
Number of molecules $s_1 + a + c$	$N_1$	4000
Number molecules $s_2 + c$	$N_2$	1200
<b>Figure 2.12 oscillation</b>		
Domain size	$L_x, L_y$	28
Resting surface tension	$\sigma_0$	5
Surface tension coupling	$k_\sigma$	0.04
Protrusive-force coupling	$k_C$	0.02
Diffusion substrate 1	$D_{s_1}$	34
Diffusion activator	$D_a$	0.3
Diffusion substrate 2	$D_{s_2}$	8
Diffusion complex	$D_c$	0.1
Number of molecules $s_1 + a + c$	$N_1$	4000
Number molecules $s_2 + c$	$N_2$	1200
<b>Figure 2.12 double oscillation</b>		
Domain size	$L_x, L_y$	28
Resting surface tension	$\sigma_0$	5
Surface tension coupling	$k_\sigma$	0.04
Protrusive-force coupling	$k_C$	0.04
Diffusion substrate 1	$D_{s_1}$	34
Diffusion activator	$D_a$	0.3
Diffusion substrate 2	$D_{s_2}$	8
Diffusion complex	$D_c$	0.1
Number of molecules $s_1 + a + c$	$N_1$	3600
Number molecules $s_2 + c$	$N_2$	600

Table 5.8: Parameters used in the simulations presented in figure 2.13

Parameter	Symbol	Value
<b>Figure 2.13 Run-and-stop cell</b>		
Domain size	$L_x, L_y$	28
Resting surface tension	$\sigma_0$	5
Surface tension coupling	$k_\sigma$	-0.04
Protrusive-force coupling	$k_C$	0.04
Diffusion substrate 1	$D_{s_1}$	34
Diffusion activator	$D_a$	0.3
Diffusion substrate 2	$D_{s_2}$	8
Diffusion complex	$D_c$	0.1
Number of molecules $s_1 + a + c$	$N_1$	4000
Number molecules $s_2 + c$	$N_2$	1400

Table 5.9: Parameters used in the simulations presented in figure 2.14

Parameter	Symbol	Value
<b>Figure 2.14 constant parameters</b>		
Domain size	$L_x, L_y$	28
Resting surface tension	$\sigma_0$	5
Diffusion substrate 1	$D_{s_1}$	34
Diffusion activator	$D_a$	0.3
Diffusion substrate 2	$D_{s_2}$	8
Diffusion complex	$D_c$	0.1
<b>Cell 1</b>		
Surface tension coupling	$k_\sigma$	-0.03
Protrusive-force coupling	$k_C$	0.02
Number of molecules $s_1 + a + c$	$N_1$	4000
Number molecules $s_2 + c$	$N_2$	1200
<b>Cell 2</b>		
Surface tension coupling	$k_\sigma$	0
Protrusive-force coupling	$k_C$	0.03
Number of molecules $s_1 + a + c$	$N_1$	4000
Number molecules $s_2 + c$	$N_2$	1200
<b>Cell 3</b>		
Surface tension coupling	$k_\sigma$	0
Protrusive-force coupling	$k_C$	0.04
Number of molecules $s_1 + a + c$	$N_1$	4000
Number molecules $s_2 + c$	$N_2$	1200
<b>Cell 3</b>		
Surface tension coupling	$k_\sigma$	-0.04
Protrusive-force coupling	$k_C$	0.04
Number of molecules $s_1 + a + c$	$N_1$	2400
Number molecules $s_2 + c$	$N_2$	200

Table 5.10: Parameters used in the simulations presented in figure 2.15

Parameter	Symbol	Value
<b>Figure 2.15</b>		
Domain size	$L_x, L_y$	28
Resting surface tension	$\sigma_0$	5
Surface tension coupling	$k_\sigma$	0.01
Protrusive-force coupling	$k_C$	0.05
Diffusion substrate 1	$D_{s_1}$	34
Diffusion activator	$D_a$	0.3
Diffusion substrate 2	$D_{s_2}$	8
Diffusion complex	$D_c$	0.1
Number of molecules $s_1 + a + c$	$N_1$	2400
Number molecules $s_2 + c$	$N_2$	700

Table 5.11: Parameters used in the simulations presented in figure 2.16

Parameter	Symbol	Value
<b>Figure 2.16</b>		
Domain size	$L_x, L_y$	28
Resting surface tension	$\sigma_0$	5
Protrusive-force coupling	$k_C$	0.03
Diffusion substrate 1	$D_{s_1}$	34
Diffusion activator	$D_a$	0.3
Diffusion substrate 2	$D_{s_2}$	8
Diffusion complex	$D_c$	0.1
Number of molecules $s_1 + a + c$	$N_1$	4000
Number molecules $s_2 + c$	$N_2$	1200
<b>Cell 1</b>		
Surface tension coupling	$k_\sigma$	-0.04
<b>Cell 2</b>		
Surface tension coupling	$k_\sigma$	0.02

Table 5.12: Parameters used in the simulations presented in figure 2.17

Parameter	Symbol	Value
<b>Figure 2.17</b>		
Domain size	$L_x, L_y$	28
Resting surface tension	$\sigma_0$	5
Surface tension coupling	$k_\sigma$	-0.02
Protrusive-force coupling	$k_C$	0.04
Diffusion substrate 1	$D_{s_1}$	34
Diffusion activator	$D_a$	0.3
Diffusion substrate 2	$D_{s_2}$	8
Diffusion complex	$D_c$	0.1
Number of molecules $s_1 + a + c$	$N_1$	4000
Number molecules $s_2 + c$	$N_2$	1200

Table 5.13: Parameters used in the simulations presented in figure 2.18

Parameter	Symbol	Value
<b>Figure 2.18 constant parameters</b>		
Domain size	$L_x, L_y$	28
Resting surface tension	$\sigma_0$	5
Surface tension coupling	$k_\sigma$	-0.06 - 0.06
Protrusive-force coupling	$k_C$	0 - 0.05
Diffusion substrate 1	$D_{s_1}$	34
Diffusion activator	$D_a$	0.3
Diffusion substrate 2	$D_{s_2}$	8
Diffusion complex	$D_c$	0.1
<b>Figure 2.18 A</b>		
Number of molecules $s_1 + a + c$	$N_1$	4000
Number molecules $s_2 + c$	$N_2$	1200
<b>Figure 2.18 B</b>		
Number of molecules $s_1 + a + c$	$N_1$	2400
Number molecules $s_2 + c$	$N_2$	700

Table 5.14: Parameters used in the simulations presented in figure 4.2

Parameter	Symbol	Value
<b>Figure 2.18 constant parameters</b>		
Domain size	$L_x, L_y$	28
Resting surface tension	$\sigma_0$	5
Surface tension coupling	$k_\sigma$	0
Protrusive-force coupling	$k_C$	0
Diffusion substrate 1	$D_{s_1}$	34
Diffusion activator	$D_a$	0.3
Diffusion substrate 2	$D_{s_2}$	8
Diffusion complex	$D_c$	0.1
Number of molecules Rac1	$N_1$	2400 – 4500
Number molecules GAP	$N_2$	600 – 1400

Table 5.15: Parameters used in the simulations presented in figure 4.3

Parameter	Symbol	Value
<b>Figure 2.18 constant parameters</b>		
Domain size	$L_x, L_y$	28
Resting surface tension	$\sigma_0$	5
Diffusion substrate 1	$D_{s_1}$	34
Diffusion activator	$D_a$	0.3
Diffusion substrate 2	$D_{s_2}$	8
Diffusion complex	$D_c$	0.1
Number of molecules Rac1	$N_1$	2400 – 4500
Number molecules GAP	$N_2$	600 – 1400
<b>Figure 4.3 A</b>		
Surface tension coupling	$k_\sigma$	-0.03
Protrusive-force coupling	$k_C$	0.03
<b>Figure 4.3 B</b>		
Surface tension coupling	$k_\sigma$	0.03
Protrusive-force coupling	$k_C$	0.03

# References

- Alisafaei F., et al., 2024, *Communications Biology*, 7, 658, *Vimentin is a key regulator of cell mechanosensing through opposite actions on actomyosin and microtubule networks*
- Alonso S., Stange M., Beta C., 2018, *PLOS ONE*, 13, e0201977, *Modeling random crawling, membrane deformation and intracellular polarity of motile amoeboid cells*
- Amin E., et al., 2016, *Journal of Biological Chemistry*, 291, 20353, *Deciphering the molecular and functional basis of rhogap family proteins: A systematic approach toward selective inactivation of rho family proteins*
- Anderson D. M., McFadden G. B., Wheeler A. A., 1998, *Annual Review of Fluid Mechanics*, 30, 139, *Diffuse-interface methods in fluid mechanics*
- Annesley S. J., Fisher P. R., 2009, *Molecular and Cellular Biochemistry*, 329, 73, *Dictyostelium discoideum—a model for many reasons*
- Aranson I. S., ed. 2016, *Physical models of cell motility*. Biological and Medical Physics, Biomedical Engineering, Springer, Cham, Switzerland, doi:10.1007/978-3-319-24448-8, <https://doi.org/10.1007/978-3-319-24448-8>
- Asano Y., Mizuno T., Kon T., Nagasaki A., Sutoh K., Uyeda T. Q. P., 2004, *Cell Motility and the Cytoskeleton*, 59, 17, *Keratocyte-like locomotion in amiB-null Dictyostelium cells*
- Baniukiewicz P., Collier S., Bretschneider T., 2018, *Bioinformatics*, 34, 2695, *Quimp: Analyzing transmembrane signalling in highly deformable cells*
- Barnhart E. L., Lee K. C., Keren K., Mogilner A., Theriot J. A., 2011, *PLOS Biology*, 9, e1001059, *An adhesion-dependent switch between mechanisms that determine motile cell shape*
- Bement W. M., et al., 2015, *Nature Cell Biology*, 17, 1471, *Activator–inhibitor coupling between rho signalling and actin assembly makes the cell cortex an excitable medium*
- Bement W. M., Goryachev A. B., Miller A. L., von Dassow G., 2024, *Nature Reviews Molecular Cell Biology*, 25, 290, *Patterning of the cell cortex by Rho GTPases*
- Beta C., Kruse K., 2017, *Annual Review of Condensed Matter Physics*, 8, 239, *Intracellular oscillations and waves*
- Bokoch G. M., 2003, *Annual Review of Biochemistry*, 72, 743, *Biology of the p21-activated kinases*
- Boulter E., Garcia-Mata R., Guilluy C., Dubash A., Rossi G., Brennwald P. J., Burridge K., 2010, *Nature Cell Biology*, 12, 477, *Regulation of Rho GTPase crosstalk, degradation and activity by RhoGDI*
- Bozzaro S., 2019, *International Journal of Developmental Biology*, 63, 321, *The past, present and future of dictyostelium as a model system*
- Brackbill J. U., Kothe D. B., Zemach C., 1992, *Journal of Computational Physics*, 100, 335, *A continuum method for modeling surface tension*
- Brandt D. T., Grosse R., 2007, *EMBO Reports*, 8, 1019, *Get to grips: steering local actin dynamics with IQGAPs*
- Brauns F., Halatek J., Frey E., 2020, *Phys. Rev. X*, 10, 041036, *Phase-space geometry of mass-conserving reaction-diffusion dynamics*
- Brückner D. B., Broedersz C. P., 2024, *Reports on Progress in Physics*, 87, 056601, *Learning dynamical models of single and collective cell migration: a review*
- Butcher J. C., 2016, *Numerical methods for ordinary differential equations*, 3 edn. John Wiley & Sons, Chichester, doi:10.1002/9781119121534, <https://doi.org/10.1002/9781119121534>

- Buttenschön A., Edelstein-Keshet L., 2020, PLOS Computational Biology, 16, e1008411, *Bridging from single to collective cell migration: A review of models and links to experiments*
- Chen S., Seara D. S., Michaud A., Kim S., Bement W. M., Murrell M. P., 2024, Nature Physics, 20, 1824, *Energy partitioning in the cell cortex*
- Chiou J.-G., Ramirez S. A., Elston T. C., Witelski T. P., Schaeffer D. G., Lew D. J., 2018, PLOS Computational Biology, 14, e1006095, *Principles that govern competition or co-existence in rho-gtpase driven polarization*
- Chorin A., 1968, Mathematics of Computation, 22, 745, *Numerical solution of the navier–stokes equations*
- Chugh P., Paluch E. K., 2018, Journal of Cell Science, 131, jcs186254, *The actin cortex at a glance*
- Coelho-Rato L. S., Parvanian S., Salajkova S. A., Medalia O., Eriksson J. E., 2024, Journal of Cell Science, 137, jcs261386, *Intermediate filaments at a glance*
- Colin A., Singaravelu P., Théry M., Blanchoin L., Gueroui Z., 2018, Current Biology, 28, 2647, *Actin-network architecture regulates microtubule dynamics*
- Cook D. R., Rossman K. L., Der C. J., 2014, Oncogene, 33, 4021, *Rho guanine nucleotide exchange factors: Regulators of rho gtpase activity in development and disease*
- Cooper G. M., Hausman R. E., 2000, *The cell: a molecular approach*. ASM press Washington, DC
- Cowan A. E., Nakhimovsky L., Myles D. G., Koppel D. E., 1997, Biophysical Journal, 73, 507, *Barriers to diffusion of plasma membrane proteins form early during guinea pig spermiogenesis*
- Dai J., Ting-Beall H. P., Hochmuth R. M., Sheetz M. P., Titus M. A., 1999, Biophysical Journal, 77, 1168, *Myosin i contributes to the generation of resting cortical tension*
- Das M., Drake T., Wiley D. J., Buchwald P., Vavylonis D., Verde F., 2012, Science, 337, 239, *Oscillatory dynamics of Cdc42 GTPase in the control of polarized growth*
- De Pascalis C., et al., 2018, Journal of Cell Biology, 217, 3031, *Intermediate filaments control collective migration by restricting traction forces and sustaining cell–cell contacts*
- Devreotes P. N., Sivaramakrishnan S., Iglesias R. J., Lampert P. A., Miao M., Bhattacharya Y., 2017, Annual Review of Cell and Developmental Biology, 33, 103, *Excitable signal transduction networks in directed cell migration*
- Douglass A. D., Vale R. D., 2005, Cell, 121, 937, *Single-molecule microscopy reveals plasma membrane microdomains created by protein-protein networks that exclude or trap signaling molecules in t cells*
- Dumontier M., Höcht P., Mintert U., Faix J., 2000, Journal of Cell Science, 113, 2253, *Rac1 gtpases control filopodia formation, cell motility, endocytosis, cytokinesis and development in dictyostelium*
- Dunn G. A., Brown A. F., 1990, in Alt W., Hoffmann G., eds, Lecture Notes in Biomathematics, Vol. 89, Biological Motion. Springer, Berlin, Heidelberg, pp 10–34, doi:10.1007/978-3-642-51664-1\_2, [https://doi.org/10.1007/978-3-642-51664-1\\_2](https://doi.org/10.1007/978-3-642-51664-1_2)
- Eden S., Rohatgi R., Podtelejnikov A. V., Mann M., Kirschner M. W., 2002, Nature, 418, 790, *Mechanism of regulation of WAVE1-induced actin nucleation by rac1 and nck*
- Eichinger L., et al., 2005, Nature, 435, 43, *The genome of the social amoeba dictyostelium discoideum*
- Eroumé K. S., Vasilevich A., Vermeulen S., de Boer J., Carlier A., 2021, PLOS ONE, 16, e0248293, *On the influence of cell shape on dynamic reaction–diffusion polarization patterns*
- Faix J., Weber I., 2013, Small GTPases, 4, 110, *A dual role model for active rac1 in cell migration*
- Faix J., Weber I., Mintert U., Köhler J., Lottspeich F., Marriott G., 2001, EMBO J., 20, 3705, *Recruitment of cortexillin into the cleavage furrow is controlled by rac1 and iggap-related proteins*
- Filić V., Marinović M., Faix J., Weber I., 2012, Journal of Cell Science, 125, 387, *A dual role for rac1 gtpases in the regulation of cell motility*
- Filić V., Marinović M., Faix J., Weber I., 2014, Cellular and Molecular Life Sciences, 71, 2775, *The iggap-related protein dgap1 mediates signaling to the actin cytoskeleton as an effector and a sequestrator of rac1 gtpases*
- Filić V., Mijanović L., Putar D., Talajić A., Četković H., Weber I., 2021, Cells, 10, 1592, *Regulation of the actin cytoskeleton via rho gtpase signalling in Dictyostelium and mammalian cells: A parallel slalom*
- Fisher P. R., Williams K. L., 1982, Microbiology, 128, 965, *Thermotactic behaviour of Dictyostelium discoideum slug phototaxis mutants*

- Fogelson A. L., Keener J. P., 2015, *SIAM Journal on Applied Mathematics*, 75, 1346, *A framework for exploring the post-gelation behavior of ziff and stell's polymerization models*
- Fornberg B., 1988, *Mathematics of Computation*, 51, 699, *Generation of finite difference formulas on arbitrarily spaced grids*
- Frey Y., Lungu C., Olayioye M. A., 2025, *Cellular Signalling*, 125, 111505, *Regulation and functions of the dlc family of rhogap proteins: Implications for development and cancer*
- Fritz-Laylin L. K., Titus M. A., 2023, *Molecular Biology of the Cell*, 34, *The evolution and diversity of actin-dependent cell migration*
- Fukata M., et al., 2002, *Cell*, 109, 873, *Rac1 and Cdc42 capture microtubules through IQGAP1 and CLIP-170*
- Garcia-Mata R., Boulter E., Burridge K., 2011, *Nature Reviews Molecular Cell Biology*, 12, 493, *The 'invisible hand': regulation of rho gtpases by rhogdis*
- Gebele R., Halatek J., Würthner L., Frey E., 2020, *Nature Communications*, 11, 539, *Geometric cues stabilise long-axis polarisation of PAR protein patterns in C. elegans*
- Gierer A., Meinhardt H., 1972, *Kybernetik*, 12, 30, *A theory of biological pattern formation*
- Girard K. D., Kuo S. C., Robinson D. N., 2006, *Proceedings of the National Academy of Sciences*, 103, 2103, *Dictyostelium myosin ii mechanochemistry promotes active behavior of the cortex on long time scales*
- Gittes F., Mickey B., Nettleton J., Howard J., 1993, *Journal of Cell Biology*, 120, 923, *Flexural rigidity of microtubules and actin filaments measured from thermal fluctuations in shape*
- Golding A. E., Visco I., Bieling P., Bement W. M., 2019, *eLife*, 8, e50471, *Extraction of active rhogtpases by rhogdi regulates spatiotemporal patterning of rhogtpases*
- Goryachev A. B., Leda M., 2019, *F1000Research*, 8, 1676, *Autoactivation of small gtpases by the gef-effector positive feedback modules*
- Graessl M., et al., 2017, *Journal of Cell Biology*, 216, 4271, *An excitable rho gtpase signaling network generates dynamic subcellular contraction patterns*
- Gräf R., Grafe M., Meyer I., Mitic K., Pitzen V., 2021, *Cells*, 10, 2657, *The dictyostelium centrosome*
- Gräf R., Batsios P., Grafe M., Meyer I., Mitic K., 2025, *Cells*, 14, 186, *Nuclear envelope dynamics in dictyostelium amoebae*
- Halatek J., Brauns F., Frey E., 2018, *Philosophical Transactions of the Royal Society B: Biological Sciences*, 373, 20170107, *Self-organization principles of intracellular pattern formation*
- Harlow F., Welch J., 1965, *Physics of Fluids*, 8, 2182, *Numerical calculation of time-dependent viscous incompressible flow of fluid with free surface*
- Hart M. J., Eva A., Evans T., Aaronson S. A., Cerione R. A., 1991, *Nature*, 354, 311, *Catalysis of guanine nucleotide exchange on the CDC42Hs protein by the dbl oncogene product*
- Havel L. S., Kline E. R., Salgueiro A. M., Marcus A. I., 2015, *Oncogene*, 34, 1979, *Vimentin regulates lung cancer cell adhesion through a vav2-rac1 pathway to control focal adhesion kinase activity*
- Heasman S. J., Ridley A. J., 2008, *Nature Reviews Molecular Cell Biology*, 9, 690, *Mammalian rho gtpases: New insights into their functions from in vivo studies*
- Hecht I., Levine H., Rappel W.-J., Ben-Jacob E., 2011, *PLOS ONE*, 6, e21955, *"self-assisted" amoeboid navigation in complex environments*
- Helfand B. T., Mikami A., Vallee R. B., Goldman R. D., 2002, *Journal of Cell Biology*, 157, 795, *A requirement for cytoplasmic dynein and dynactin in intermediate filament network assembly and organization*
- Helfand B. T., et al., 2011, *Molecular Biology of the Cell*, 22, 1274, *Vimentin organization modulates the formation of lamellipodia*
- Henty-Ridilla J. L., Rankova A., Eskin J. A., Kenny K., Goode B. L., 2016, *Science*, 352, 1004, *Accelerated actin filament polymerization from microtubule plus ends*
- Holmes W. R., Edelstein-Keshet L., 2012, *PLOS Computational Biology*, 8, e1002793, *A comparison of computational models for eukaryotic cell shape and motility*

- Hookway C., Ding L., Davidson M. W., Rappoport J. Z., Danuser G., Gelfand V. I., 2015, *Molecular Biology of the Cell*, 26, 1675, *Microtubule-dependent transport and dynamics of vimentin intermediate filaments*
- Houk A. R., et al., 2012, *Cell*, 148, 175, *Membrane tension maintains cell polarity by confining signals to the leading edge during neutrophil migration*
- Htet P. H., Lauga E., 2025, *PNAS Nexus*, 4, pgaf057, *Analytical methods for cytoplasmic streaming in elongated cells*
- Huang W., Russell R. D., 2011, *Adaptive moving mesh methods*. Applied Mathematical Sciences Vol. 174, Springer New York, doi:10.1007/978-1-4419-7916-2, <https://doi.org/10.1007/978-1-4419-7916-2>
- Hynes R. O., 2002, *Cell*, 110, 673, *Integrins: Bidirectional, allosteric signaling machines*
- Infante E., Etienne-Manneville S., 2022, *Frontiers in Cell and Developmental Biology*, 10, 951816, *Intermediate filaments: Integration of cell mechanical properties during migration*
- Innocenti M., et al., 2004, *Nature Cell Biology*, 6, 319, *Abi1 is essential for the formation and activation of a wave2 signalling complex*
- International Organization for Standardization (ISO) International Electrotechnical Commission (IEC) 2024, *Information technology — programming languages — c*, International Standard ISO/IEC 9899:2024, 5th ed., <https://www.iso.org/standard/82075.html>
- Ishikawa-Ankerhold H., Kroll J., van den Heuvel D., Renkawitz J., Müller-Taubenberger A., 2022, *Cells*, 11, 1776, *Centrosome positioning in migrating Dictyostelium cells*
- Ishizaki T., Morishima Y., Okamoto M., Furuyashiki T., Kato T., Narumiya S., 2001, *Nature Cell Biology*, 3, 8, *Coordination of microtubules and the actin cytoskeleton by the rho effector mdial*
- Ivšić B., 2019, Master's thesis, Faculty of Science (PMF), University of Zagreb, Department of Physics, Zagreb, Croatia, <https://repositorij.pmf.unizg.hr/object/pmf:7638>
- Jaffe A. B., Hall A., 2005, *Annual Review of Cell and Developmental Biology*, 21, 247, *Rho gtpases: biochemistry and biology*
- Jilkine A., Marée A. F. M., Edelstein-Keshet L., 2007, *Bulletin of Mathematical Biology*, 69, 1943, *Mathematical model for spatial segregation of the rho-family gtpases based on inhibitory crosstalk*
- Jimenez A. J., et al., 2021, *Current Biology*, 31, 1206, *Acto-myosin network geometry defines centrosome position*
- Jiu Y., Peränen J., Schaible N., Cheng F., Eriksson J. E., Krishnan R., Lappalainen P., 2017, *Journal of Cell Science*, 130, 892, *Vimentin intermediate filaments control actin stress fiber assembly through GEF- H1 and RhoA*
- Johnson J. L., Erickson J. W., Cerione R. A., 2009, *Journal of Biological Chemistry*, 284, 23860, *New insights into how the rho guanine nucleotide dissociation inhibitor regulates the interaction of cdc42 with membranes*
- Kabaso D., Shlomovitz R., Schloen K., Stradal T., Gov N. S., 2011, *PLOS Computational Biology*, 7, e1001127, *Theoretical model for cellular shapes driven by protrusive and adhesive forces*
- Katsuta H., et al., 2023, *iScience*, 26, 106090, *Actin crosslinking by  $\alpha$ -actinin averts viscous dissipation of myosin force transmission in stress fibers*
- Keep N. H., Barnes M., Barsukov I. L., Badii R., Lian L., Segal A. W., Moody P. C. E., Roberts G. C. K., 1997, *Structure*, 5, 623, *A modulator of rho family g proteins, rhoGDI, binds these g proteins via an immunoglobulin-like domain and a flexible n-terminal arm*
- Kimmel A. R., Faix J., 2006, in Eichinger L., Rivero F., eds, *Methods in Molecular Biology*, Vol. 346, Dictyostelium Protocols. Humana Press, Totowa, NJ, pp 187–199, doi:10.1385/1-59745-144-4:187
- Kuusela E., Alt W., 2009, *Journal of Mathematical Biology*, 58, 135, *Continuum model of cell adhesion and migration*
- Landau L. D., Lifshitz E. M., 1987, *Fluid mechanics*, 2 edn. No. 6 in Course of Theoretical Physics, Pergamon Press, Oxford, doi:10.1016/C2013-0-03799-1, <https://doi.org/10.1016/C2013-0-03799-1>
- Lanier M. H., Kim T., Cooper J. A., 2015, *Molecular Biology of the Cell*, 26, 4577, *Carmil2 is a novel molecular connection between vimentin and actin essential for cell migration and invadopodia formation*
- Lauffenburger D. A., Horwitz A. F., 1996, *Cell*, 84, 359, *Cell migration: a physically integrated molecular process*

- LeVeque R. J., 2007, *Finite difference methods for ordinary and partial differential equations: Steady-state and time-dependent problems*. Society for Industrial and Applied Mathematics, Philadelphia, PA, doi:10.1137/1.9780898717839, <https://doi.org/10.1137/1.9780898717839>
- Leduc C., Etienne-Manneville S., 2017, *Journal of Cell Biology*, 216, 1689, *Regulation of microtubule-associated motors drives intermediate filament network polarization*
- Lee S. H., Dominguez R., 2010, *Molecules and Cells*, 29, 311, *Regulation of actin cytoskeleton dynamics in cells*
- Lee G., Leech G., Rust M. J., Das M., McGorty R. J., Ross J. L., Robertson-Anderson R. M., 2021, *Science Advances*, 7, eabe4334, *Myosin-driven actin-microtubule networks exhibit self-organized contractile dynamics*
- Li L., Cox E. C., Flyvbjerg H., 2011, *Physical Biology*, 8, 046006, *'dicty dynamics': Dictyostelium motility as persistent random motion*
- Liu Y., Rens E. G., Edelstein-Keshet L., 2021, *Journal of Mathematical Biology*, 82, 28, *Spots, stripes, and spiral waves in models for static and motile cells*
- Lombardi M. L., Knecht D. A., Dembo M., Lee J., 2007, *Journal of Cell Science*, 120, 1624, *Traction force microscopy in Dictyostelium reveals distinct roles for myosin ii motor and actin-crosslinking activity in polarized cell movement*
- MacDonald G., Mackenzie J. A., Nolan M., Insall R. H., 2016, *Journal of Computational Physics*, 309, 207, *A computational method for the coupled solution of reaction-diffusion equations on evolving domains and manifolds: Application to a model of cell migration and chemotaxis*
- Machacek M., et al., 2009, *Nature*, 461, 99, *Coordination of rho gtpase activities during cell protrusion*
- Mackenzie J. A., Rowlatt C. F., Insall R. H., 2019, arXiv preprint arXiv:1910.02282, *A conservative finite element scheme for mass-conserving reaction-diffusion equations on evolving two-dimensional domains*
- Maeda Y. T., Inose J., Matsuo M. Y., Iwaya S., Sano M., 2008, *PLOS ONE*, 3, e3734, *Ordered patterns of cell shape and orientational correlation during spontaneous cell migration*
- Maekawa M., et al., 1999, *Science*, 285, 895, *Signaling from Rho to the actin cytoskeleton through protein kinases ROCK and LIM-kinase*
- Maniotis A. J., Chen C. S., Ingber D. E., 1997, *Proceedings of the National Academy of Sciences of the United States of America*, 94, 849, *Demonstration of mechanical connections between integrins, cytoskeletal filaments, and nucleoplasm that stabilize nuclear structure*
- Marinović M., Šoštar M., Filić V., Antolović V., Weber I., 2016, *Histochemistry and Cell Biology*, 146, 267, *Quantitative imaging of rac1 activity in Dictyostelium cells with a fluorescently labelled gtpase-binding domain from dpka kinase*
- Marée A. F. M., Grieneisen V. A., Edelstein-Keshet L., 2012, *PLOS Computational Biology*, 8, e1002402, *How cells integrate complex stimuli: The effect of feedback from phosphoinositides and cell shape on cell polarization and motility*
- Mattila P. K., Lappalainen P., 2008, *Nature Reviews Molecular Cell Biology*, 9, 446, *Filopodia: molecular architecture and cellular functions*
- Meinhardt H., Gierer A., 1980, *Journal of Theoretical Biology*, 85, 429, *Generation and regeneration of sequence of structures during morphogenesis*
- Merino-Casallo F., Gomez-Benito M. J., Hervas-Raluy S., Garcia-Aznar J. M., 2022, *Cell Adhesion & Migration*, 16, 25, *Unravelling cell migration: defining movement from the cell surface*
- Merkel R., Simson R., Simson D. A., Hohenadl M., Boulbitch A., Wallraff E., Sackmann E., 2000, *Biophysical Journal*, 79, 707, *A micromechanic study of cell polarity and plasma membrane-cell body coupling in Dictyostelium*
- Miao Y., Bhattacharya S., Edwards M., Cai H., Inoue T., Iglesias P. A., Devreotes P. N., 2017, *Nature Cell Biology*, 19, 329, *Altering the threshold of an excitable signal transduction network changes cell migratory modes*
- Michaux J. B., Robin F. B., McFadden W. M., Munro E. M., 2018, *Journal of Cell Biology*, 217, 4230, *Excitable rhoa dynamics drive pulsed contractions in the early C. elegans embryo*
- Mijanović L., Weber I., 2022, *Frontiers in Cell and Developmental Biology*, 10, 910736, *Adhesion of dictyostelium amoebae to surfaces: A brief history of attachments*

- Mitchison T. J., Kirschner M. W., 1984, *Nature*, 312, 237, *Dynamic instability of microtubule growth*
- Mogilner A., Oster G., 1996, *Biophysical Journal*, 71, 3030, *Cell motility driven by actin polymerization*
- Mogilner A., Oster G., 2003, *Biophysical Journal*, 84, 1591, *Force generation by actin polymerization II: The elastic ratchet and tethered filaments*
- Moreno E., Alonso S., 2022, *Frontiers in Physics*, 10, 881885, *Mass-conservation increases robustness in stochastic reaction-diffusion models of cell crawling*
- Moreno E., Flemming S., Font F., 2020, *Physica D: Nonlinear Phenomena*, 412, 132591, *Modeling cell crawling strategies with a bistable model: From amoeboid to fan-shaped cell motion*
- Moreno E., Großmann R., Beta C., Alonso S., 2022, *Frontiers in Physics*, 9, 750187, *From single to collective motion of social amoebae: A computational study of interacting cells*
- Mori Y., Jilkine A., Edelstein-Keshet L., 2008, *Biophysical Journal*, 94, 3684, *Wave-pinning and cell polarity from a bistable reaction-diffusion system*
- Morton K. W., Mayers D. F., 2005, *Numerical solution of partial differential equations: An introduction*, 2 edn. Cambridge University Press, Cambridge, doi:10.1017/CBO9780511812248, <https://doi.org/10.1017/CBO9780511812248>
- Mosaddeghzadeh N., Ahmadian M. R., 2021, *Cells*, 10, 1831, *The rho family gtpases: Mechanisms of regulation and signaling*
- Moure A., Gomez H., 2016, *Physical Review E*, 94, 042423, *Computational model for amoeboid motion: Coupling membrane and cytosol dynamics*
- Narumiya S., Tanji M., Ishizaki T., 2009, *Cancer Metastasis Reviews*, 28, 65, *Rho signaling, rock and mdia1, in transformation, metastasis and invasion*
- Neilson M. P., Mackenzie J. A., Webb S. D., Insall R. H., 2010, *Integrative Biology*, 2, 687, *Use of the parameterised finite element method to robustly and efficiently evolve the edge of a moving cell*
- Ning W., et al., 2016, *Developmental Cell*, 39, 61, *The camsap3-acf7 complex couples noncentrosomal microtubules with actin filaments to coordinate their dynamics*
- Ning Y., Zheng M., Zhang Y., Jiao Y., Wang J., Zhang S., 2024, *Cancer Cell International*, 24, 339, *Rhoa-rock2 signaling possesses complex pathophysiological functions in cancer progression and shows promising therapeutic potential*
- Niwayama R., Nagao H., Kitajima T. S., Hufnagel L., Shinohara K., Higuchi T., Ishikawa T., Kimura A., 2016, *PLOS ONE*, 11, e0159917, *Bayesian inference of forces causing cytoplasmic streaming in *Caenorhabditis elegans* embryos and mouse oocytes*
- Nobes C. D., Hall A., 1995, *Cell*, 81, 53, *Rho, rac, and cdc42 gtpases regulate the assembly of multimolecular focal complexes associated with actin stress fibers, lamellipodia, and filopodia*
- Noritake J., et al., 2004, *Molecular Biology of the Cell*, 15, 1065, *Positive role of IQGAP1, an effector of Rac1, in actin-meshwork formation at sites of cell-cell contact*
- Ohashi K., Kunitomi A., Chiba S., Mizuno K., 2024, *Frontiers in Cell and Developmental Biology*, 12, 1485725, *Roles of the dbl family of rhoGefs in mechanotransduction – a review*
- Oono Y., Puri S., 1987, *Physical Review Letters*, 58, 836, *Computationally efficient modeling of ordering of quenched phases*
- Oono Y., Puri S., 1988, *Physical Review A*, 38, 434, *Study of phase-separation dynamics by use of cell dynamical systems. i. modeling*
- Osher S., Fedkiw R. P., 2003, *Level set methods and dynamic implicit surfaces*, 1 edn. No. 153 in *Applied Mathematical Sciences*, Springer-Verlag, New York, NY, doi:10.1007/b98879, <https://doi.org/10.1007/b98879>
- Osher S., Sethian J. A., 1988, *Journal of Computational Physics*, 79, 12, *Fronts propagating with curvature-dependent speed: Algorithms based on hamilton-jacobi formulations*
- Otsuji M., Ishihara S., Co C., Kaibuchi K., Mochizuki A., Kuroda S., 2007, *PLOS Computational Biology*, 3, e108, *A mass conserved reaction-diffusion system captures properties of cell polarity*

- Palazzo A. F., Cook T. A., Alberts A. S., Gundersen G. G., 2001, *Nature Cell Biology*, 3, 723, *mdia mediates rho-regulated formation and orientation of stable microtubules*
- Parameswaran S., Mandal J. C., 2023, *European Journal of Mechanics – B/Fluids*, 98, 40, *A stable interface-preserving reinitialization equation for conservative level set method*
- Patra M., Karttunen M., 2006, *Numerical Methods for Partial Differential Equations*, 22, 936, *Stencils with isotropic discretization error for differential operators*
- Pears C. J., Gross J. D., 2021, *Microbiology*, 167, 001040, *Microbe profile: Dictyostelium discoideum: model system for development, chemotaxis and biomedical research*
- Pertz O., Hodgson L., Klemke R. L., Hahn K. M., 2006, *Nature*, 440, 1069, *Spatiotemporal dynamics of RhoA activity in migrating cells*
- Peskin C. S., 2002, *Acta Numerica*, 11, 479, *The immersed boundary method*
- Peskin C. S., Odell G. M., Oster G. F., 1993, *Biophysical Journal*, 65, 316, *Cellular motions and thermal fluctuations: the brownian ratchet*
- Pollard T. D., 2019, *Annual Review of Cell and Developmental Biology*, 35, 1, *Cell motility and cytokinesis: From mysteries to molecular mechanisms in five decades*
- Press W. H., Teukolsky S. A., Vetterling W. T., Flannery B. P., 2007, *Numerical recipes: The art of scientific computing*, 3 edn. Cambridge University Press, Cambridge
- Rathje L.-S. Z., Nordgren N., Pettersson T., Rönnlund D., Widengren J., Aspenström P., Gad A. K. B., 2014, *Proceedings of the National Academy of Sciences*, 111, 1515, *Oncogenes induce a vimentin filament collapse mediated by hdac6 that is linked to cell stiffness*
- Ridley A. J., 2001, *Journal of Cell Science*, 114, 2713, *Rho gtpases and cell migration*
- Rittinger K., Walker P. A., Eccleston J. F., Smerdon S. J., Gamblin S. J., 1997, *Nature*, 389, 758, *Structure at 1.65 Å of RhoA and its GTPase-activating protein in complex with a transition-state analogue*
- Rivero F., Xiong H., 2016, *International Review of Cell and Molecular Biology*, 322, 61, *Rho signaling in Dictyostelium discoideum*
- Rohatgi R., Ma L., Miki H., Lopez M., Kirchhausen T., Takenawa T., Kirschner M. W., 1999, *Cell*, 97, 221, *The interaction between n-wasp and the arp2/3 complex links cdc42-dependent signals to actin assembly*
- Russo G., Smereka P., 2000, *Journal of Computational Physics*, 163, 51, *A remark on computing distance functions*
- Saad Y., 2003, *Iterative methods for sparse linear systems*, 2 edn. No. 82 in *Other Titles in Applied Mathematics*, Society for Industrial and Applied Mathematics, Philadelphia, PA, doi:10.1137/1.9780898718003, <https://doi.org/10.1137/1.9780898718003>
- Sackmann E., Keber F., Heinrich D., 2010, *Annual Review of Condensed Matter Physics*, 1, 257, *Physics of cellular movements*
- Schaap P., 2011, *Development*, 138, 387, *Evolutionary crossroads in developmental biology: Dictyostelium discoideum*
- Schaedel L., Lorenz C., Schepers A. V., Klumpp S., Köster S., 2021, *Nature Communications*, 12, 3799, *Vimentin intermediate filaments stabilize dynamic microtubules by direct interactions*
- Schindelin J., et al., 2012, *Nature Methods*, 9, 676, *Fiji: An open-source platform for biological-image analysis*
- Schindler D., Moldenhawer T., Beta C., Huisinga W., Holschneider M., 2024, *PLOS ONE*, 19, e0297511, *Three-component contour dynamics model to simulate and analyze amoeboid cell motility in two dimensions*
- Scriven L., Sternling C., 1960, *Nature*, 187, 186, *The marangoni effects*
- Seetharaman S., Etienne-Manneville S., 2019, *Journal of Cell Science*, 132, jcs232843, *Microtubules at focal adhesions – a double-edged sword*
- Seetharaman S., Etienne-Manneville S., 2020, *Trends in Cell Biology*, 30, 720, *Cytoskeletal crosstalk in cell migration*
- Sells M. A., Boyd J. T., Chernoff J., 1999, *Journal of Cell Biology*, 145, 837, *p21-activated kinase 1 (pak1) regulates cell motility in mammalian fibroblasts*

- Sens P., Plastino J., 2015, *Journal of Physics: Condensed Matter*, 27, 273103, *Membrane tension and cytoskeleton organization in cell motility*
- Shao D., Levine H., Rappel W.-J., 2012, *Proceedings of the National Academy of Sciences*, 109, 6851, *Coupling actin flow, adhesion, and morphology in a computational cell motility model*
- Shi C., Huang C.-H., Devreotes P. N., Iglesias P. A., 2013, *PLOS Computational Biology*, 9, e1003122, *Interaction of motility, directional sensing, and polarity modules recreates the behaviors of chemotaxing cells*
- Singh A. R., Leadbetter T., Camley B. A., 2022, *Proceedings of the National Academy of Sciences*, 119, e2121302119, *Sensing the shape of a cell with reaction diffusion and energy minimization*
- Sussman M., Smereka P., Osher S., 1994, *Journal of Computational Physics*, 114, 146, *A level set approach for computing solutions to incompressible two-phase flow*
- Teague M. R., 1980, *Journal of the Optical Society of America*, 70, 920, *Image analysis via the general theory of moments*
- Terriac E., Coceano G., Mavajian Z., Hageman T. A. G., Christ A. F., Testa I., Lautenschläger F., Gad A. K. B., 2017, *Cells*, 6, 2, *Vimentin levels and serine 71 phosphorylation in the control of cell-matrix adhesions, migration speed, and shape of transformed human fibroblasts*
- The MathWorks, Inc. 2023, *MATLAB (r2023b)*. The MathWorks, Inc., Natick, Massachusetts, <https://www.mathworks.com/products/matlab.html>
- Tryggvason G., Scardovelli R., Zaleski S., 2011, *Direct numerical simulations of gas-liquid multiphase flows*. Cambridge Monographs on Applied and Computational Mathematics, Cambridge University Press, Cambridge, doi:10.1017/CBO9780511975264, <https://doi.org/10.1017/CBO9780511975264>
- Turing A. M., 1952, *Philosophical Transactions of the Royal Society of London. Series B, Biological Sciences*, 237, 37, *The chemical basis of morphogenesis*
- Tyson R. A., Epstein D. B. A., Anderson K. I., Bretschneider T., 2010, *Mathematical Modelling of Natural Phenomena*, 5, 34, *High resolution tracking of cell membrane dynamics in moving cells: an electrifying approach*
- Van Haastert P. J. M., Bosgraaf L., 2009, *PLOS ONE*, 4, e6814, *Food searching strategy of amoeboid cells by starvation induced run length extension*
- Watanabe N., Kato T., Fujita A., Ishizaki T., Narumiya S., 1999, *Nature Cell Biology*, 1, 136, *Cooperation between mDia1 and ROCK in Rho-induced actin reorganization*
- Weißbruch K., Mayor R., 2024, *BioEssays*, 46, e2400055, *Actomyosin forces in cell migration: Moving beyond cell body retraction*
- Wen Q., Janmey P. A., 2011, *Current Opinion in Solid State and Materials Science*, 15, 177, *Polymer physics of the cytoskeleton*
- Whitfield C. A., Hawkins R. J., 2016, *New Journal of Physics*, 18, 123016, *Instabilities, motion and deformation of active fluid droplets*
- Wittmann T., Bokoch G. M., Waterman-Storer C. M., 2003, *Journal of Cell Biology*, 161, 845, *Regulation of leading edge microtubule and actin dynamics downstream of rac1*
- Wu X., Kodama A., Fuchs E., 2008, *Cell*, 135, 137, *Acf7 regulates cytoskeletal-focal adhesion dynamics and migration and has atpase activity*
- Yoshioka K., Kagami O., Nagasaki A., Sekiguchi Y., Mizuno T., 2011, *bioimages*, 19, 7, *Microtubule disruption and Dictyostelium cell motility: Effects on random migration and chemotaxis*
- Young D. M., 1954, *Transactions of the American Mathematical Society*, 76, 92, *Iterative methods for solving partial difference equations of elliptic type*
- Ziebert F., Aranson I. S., 2016, *npj Computational Materials*, 2, 16019, *Computational approaches to substrate-based cell motility*
- Šoštar M., 2022, PhD thesis, Sveučilište u Zagrebu, Prirodoslovno-matematički fakultet, Zagreb, Hrvatska, <https://urn.nsk.hr/urn:nbn:hr:217:457625>
- Šoštar M., Marinović M., Filić V., Pavin N., Weber I., 2024, *PLOS Computational Biology*, 20, e1012025, *Oscillatory dynamics of rac1 activity in Dictyostelium discoideum amoebae*

# Supervisor information

## **Sr. Res. Assoc. Tomislav Vuletić, PhD**

Has been a scientist at the Institute of Physics since 2008 and has held the rank of Senior Research Associate since 2011. From 2017 to 2019 he served as Deputy Director. He earned a PhD in condensed-matter physics at the Department of Physics, Faculty of Science (PMF), University of Zagreb, and completed postdoctoral training at Université Paris-Sud XI.

Between 2010 and 2021 he was Secretary of the Croatian Biophysical Society and Head of the International School of Biophysics, and he has organized numerous scientific meetings. He has supervised around a dozen doctoral and master's theses. He has led and contributed to multiple national scientific and technological projects (UKF, BICRO, Croatian Science Foundation-HrZZ), and has collaborated on the Institute of Physics infrastructure project CALT (Centre for Advanced Laser Techniques) as well as on activities within the Centre of Excellence CEMS (Centre for Advanced Materials and Sensors). He also serves as a reviewer for EU and national funding agencies and for international journals.

His research focuses on the interface of biology and nanotechnology, with particular interest in macromolecules, molecular machines, and cellular components; nano-bio hybrids and nanopores; and biopolymers and biopolyelectrolytes. He led the design, planning, set-up, and equipping of the Institute's laboratories for experimental soft-matter physics research, and has overseen their ongoing redesign, upgrading, and procurement of new equipment. The group's experimental capabilities include dielectric/impedance spectroscopy; quartz crystal microbalance with dissipation monitoring (QCM-D) for deposition and binding studies of biomacromolecules and cells; polarization microscopy; fluorescence correlation spectroscopy (FCS); atomic force microscopy (AFM); and a dedicated biochemical wet lab.

He has delivered approximately 20 invited talks and seminars, authored more than 30 scientific publications,<sup>1</sup> and is a co-inventor on one international patent application.

---

<sup>1</sup>A complete publication list is available via the Croatian Scientific Bibliography (CROSBI): <https://www.bib.irb.hr:8443/pretraga?operators=and%7C29793%7Ctext%7Cprofile&page=3>.

## Prof. Matko Glunčić, PhD

Matko Glunčić was born on 11 August 1972 in Dubrovnik, Croatia. He completed his elementary and secondary education in Dubrovnik, where he graduated from a mathematics and computer science high school in 1991. He enrolled in the undergraduate Physics program at the Faculty of Science, University of Zagreb, and obtained the degree of Dipl. Ing. Phys. He continued his academic training at the same institution, where he defended his doctoral thesis in physics in 2009.

From 2001 to 2013, he held positions as assistant and senior assistant at the Department of Physics, Faculty of Science, University of Zagreb. In the period 2012-2013, he conducted postdoctoral research at the Max Planck Institute for the Physics of Complex Systems in Dresden, Germany, where his research interests further expanded toward theoretical biophysics and bioinformatics. He was appointed Assistant Professor (Docent) in 2013, Associate Professor in 2020, and Full Professor in 2025 at the Department of Physics, Faculty of Science, University of Zagreb. From 2016 to 2018, he served as State Secretary at the Ministry of Science and Education of the Republic of Croatia.

His scientific research lies at the intersection of theoretical physics, bioinformatics, and biophysics, with a particular focus on the structure and evolution of repetitive DNA sequences in human and primate genomes, centromeric organization, and the dynamics of microtubules and molecular motors. He has authored or co-authored over 45 scientific publications<sup>2</sup>, including papers in leading international journals such as *Physical Review Letters*, *Nature Communications*, *Nucleic Acids Research*, *Bioinformatics*, *Molecular Biology and Evolution*, *Scientific Reports*, *Life Science Alliance*, and *Bioinformatics Advances*. His work has been cited around 500 times in the Web of Science Core Collection. Dr. Glunčić has been the principal investigator or collaborator on several nationally and internationally funded research projects, including projects supported by the Croatian Science Foundation, the University of Zagreb, the Max Planck Society, and the Scientific Centre of Excellence for Quantum and Complex Systems. He is the developer of the Global Repeat Map (GRM) methodology and its extensions, which are widely used for the identification and analysis of higher-order repetitive structures in genomes.

He has supervised ten graduate theses, one bachelor's thesis at the Technische Universität Wien, and currently supervises one doctoral student. He has extensive teaching experience at undergraduate, graduate, and doctoral levels, having delivered more than 5,000 teaching hours across physics, bioinformatics, and data analysis courses. He has also actively contributed to

---

<sup>2</sup>A complete publication list is available via the Croatian Scientific Bibliography (CROSBI): <https://www.bib.irb.hr:8443/pretraga?operators=and|Glun%C4%8Di%C4%87,%20Matko%20%2821091%29|text|profile>.

curriculum development and interdisciplinary study programs.

In addition to his academic activities, Dr. Glunčić has held numerous institutional and national leadership roles, including President of the Governing Board of the Institute of Physics, State Secretary at the Ministry of Science and Education of the Republic of Croatia, membership in national advisory councils for science, education, and research infrastructures, and expert roles in EU-funded projects related to education policy, labour market analysis, and skills classification.

# Curriculum vitae

Blaž Ivšić was born on 3 June 1995 in Brežice, Slovenia. He completed primary school in Brežice before moving to Zagreb, Croatia, where he graduated from the Lucijan Vranjanin Gymnasium (academic high school). In 2014, he enrolled in physics at the Department of Physics, Faculty of Science, University of Zagreb, and graduated in 2019. His Master's thesis was completed under the supervision of Prof. Dr. Igor Weber at the Laboratory of Cell Dynamics, Ruđer Bošković Institute (Zagreb), and was entitled *Rac1 dynamics and its dependence on cell shape*. In this work, he investigated the effect of static domain geometry on mass-conserved reaction–diffusion systems. In 2020, he began working as a research assistant at the Institute of Physics, Zagreb, and enrolled in a postgraduate programme in Biophysics at the Department of Physics, Faculty of Science, University of Zagreb. During 2020–2025, he worked as a teaching assistant at the Faculty of Science, the Faculty of Food Technology and Biotechnology, and the Faculty of Graphic Arts (University of Zagreb). He is a member of the Croatian Biophysical Society. At the time of writing this thesis, he has published two scientific papers as an author or co-author.<sup>3</sup>

---

<sup>3</sup>A complete publication list is available via the Croatian Scientific Bibliography (CROSBİ): <https://www.crois.hr/osobe/profil/36146>.

## Refereed publications

### Published

- 1 **Ivšić, B.**, Vulić, D., Weber, I., Nowakowski, P., & Smith, A.-S., 2026, *PLOS Computational Biology*, 22(4), e1014216, *Diversity in emergent cell locomotion from the coupling cytosolic and cortical Marangoni flows with reaction–diffusion dynamics*
- 2 Biba, R., Košpić, K., **Ivšić, B.**, Vujević, L., Hozić, A., Erk, M., Đapić, I., & Cindrić, M., 2025, *Journal of Chromatography Open*, 8, 100262, *Orthogonality of separation and sorbent evaluation in offline multidimensional peptide fractionation using automated positive pressure micro solid phase extraction*

### Non-refereed publications

- 1 **Ivšić, B.**, Nowakowski, P., Weber, I., & Smith, A.-S., 2025, DPG-Frühjahrstagung (DPG Spring Meeting) of the Condensed Matter Section (SKM), Regensburg, Germany, 16–21 March 2025, *Coupling reaction-diffusion and locomotion in vegetative cells* (abstract)
- 2 **Ivšić, B.**, Vuletić, T., Šoštar, M., & Weber, I., 2022, 4th Croatian Microscopy Congress (CMC 2022), Poreč, Croatia, 18–20 May 2022, *Dependence of cell shape on spatial confinement*
- 3 **Ivšić, B.**, Šoštar, M., Vuletić, T., & Weber, I., 2022, 15th Easter Biophysics Workshop, Tainach, Austria, 19–20 April 2022, *Influence of cell shape on dynamics of Rac1*
- 4 Milisav, A.-M., Šegota, S., Vuletić, T., **Ivšić, B.**, Brkić, A. L., & Dutour Sikirić, M., 2022, *Arhiv za higijenu rada i toksikologiju*, A16–A16, *Multilayers of Polyaminoacids and Silver Nanoparticles as Antimicrobial Coatings for Orthopaedic Implants*